Behavior of diaphragm walls in clays and reliablity analysis

Xuan, Feng

2009

Xuan, F. (2009). Behavior of diaphragm walls in clays and reliablity analysis. Master’s thesis, Nanyang Technological University, Singapore.

https://hdl.handle.net/10356/19261

https://doi.org/10.32657/10356/19261

NANYANG TECHNOLOGICAL UNIVERSITY

BEHAVIOR OF DIAPHRAGM WALLS IN CLAYS AND RELIABLITY ANALYSIS

XUAN FENG

SCHOOL OF CIVIL AND ENVIRONMENT ENGNIEERING

2009

Behavior of Diaphragm Walls in Clays and Reliability Analysis

Xuan Feng

School of Civil and Environment Engineering

A thesis submitted to the Nanyang Technological University
in fulfillment of the requirement for the degree of
Master of Engineering

2009

ACKNOWLEDGEMENTS

First and foremost, the author would like to express his deepest gratitude to his supervisor, Associate Professor Anthony Goh Teck Chee, for his constant encouragement, guidance and suggestion, since the author was in Shanghai Jiao Tong University. Without his consistent and illuminating instruction, the report could not have reached its present form.

At the same time, the author would like to express his gratitude to Professor Wang Jian Hua from Shanghai Jiao Tong University, for his guidance and suggestions in the concept of the project and giving the author the opportunity to take part in the Exchange-Program between NTU and SJTU.

Next, the author would like to express his gratitude to Dr. Wong Kai Sin for his invaluable advice, and the help from the staff of CEE.

Finally, the author would also like to express his gratitude to Nanyang Technological University for providing this program. It provides a good opportunity and environment to expand author's views and knowledge not only on the research field but also outlook on life.

ABSTRACT

With rapid economic development, the number of braced excavation projects has grown in Singapore and other coastal cities. The technology of diaphragm wall is widely used in these areas where soil deposits comprise of thick soft clay layers overlying stiff clay. However, the traditional empirical methods for predicting wall deflection, ground movement, and strut forces for these excavations are mostly based on excavations with flexible walls. This project studies the excavation behavior using the Finite element method. Uncertainties in the process of design and construction of excavations have been considered through reliability analysis. This project aims to study the behavior of excavations with diaphragm wall in soft clay and to develop a procedure to estimate the reliability index associated with wall and ground movement for excavation system. The following are the major aspects of this project.

1. The small strain effect on excavation problems has been assessed using the HSS (Hardening small-strain) model implemented in PLAXIS 8.5 (commercial software). The characteristic of small strain behavior is reflected by analysis of several case histories with the HSS model and comparisons of the behavior with other soil models. A coefficient is introduced to evaluate the small strain effect on wall deflections.
2. Parametric studies have been carried out to study the excavation behavior with respect to wall deflection, soil settlement and apparent pressure. The response surfaces equations for predicting the maximum wall deflection and soil settlement have been proposed. A chart is proposed to estimate the maximum apparent pressure for calculating the strut forces.
3. Reliability analyses on wall deflection and surface settlement have been illustrated by two examples. Simplified charts have been proposed to assess the failure probability of wall deflection and surface settlement.

TABLE OF CONTENTS

LIST OF TABLES

LIST OF FIGURES

LIST OF SYMBOLS

Symbol	Description
B	Excavation width
H	Excavation depth
H_e	Final excavation depth
c_u	Undrained shear strength
N_c	Bearing capacity coefficient
q	Surcharge pressure
μ_t	Clay thickness factor
μ_d	Wall penetration factor
μ_w	Wall stiffness factor
δ_{hm}	Maximum lateral wall deflection
E	Young's modulus of building component
I	Moment of inertia
δ_{vm}	Maximum ground settlement
R	Deformation ratio; Correlation matrix
K_o	Coefficient of earth pressure at rest
γ	Unit weight
β	Reliability index
c	Cohesion of soil
x	Random variable
σ	Standard deviation
φ	Friction angle of soil
ψ	Dilatancy angle
m	Power for stress-level dependency of stiffness; Mean of random variable; Coefficient in Terzaghi & Peck method for apparent pressure diagram
p^{ref}	Reference stress for stiffness

E_{50}^{ref}	Reference secant stiffness in standard drained triaxial test
E_{50}	Secant stiffness in standard drained triaxial test
E_{oed}^{ref}	Reference tangent stiffness for primary oedometer loading
E_{oed}	Tangent stiffness for primary oedometer loading
E_{ur}^{ref}	Reference unloading/reloading stiffness
E_{ur}	Unloading/reloading stiffness
υ	Poisson ratio
G_0^{ref}	Reference shear modulus at very small strains ($\varepsilon < 10^{-6}$)
G_0	Shear modulus at very small strains
G_{secant}	Secant shear modulus
$\gamma_{0.7}$	Shear strain at which $G_{secant} = G_0$
E_u	Undrained stiffness of soil
E'	Drained stiffness of soil
σ_1'	Maximum principal stress
σ_v'	Vertical effective stress
σ_3'	Minor principal stress
R_f	Failure ratio
N_{SPT}	Blow count of SPT
A	Area of spring
k	Permeability; ratio of soil initial shear modulus to unloading/reloading stiffness
η	Slope of wall deflection path
I_R	Ratio of soil initial shear modulus to soil undrained shear strength
t	Ratio of soil initial stiffness to unloading/reloading stiffness
δ_{HSS}	Wall deflection modeled by HSS
δ_{HS}	Wall deflection modeled by HS

μ_{ss}	Ratio of wall deflection modeled by HSS to wall deflection modeled by HS
d	Wall thickness
T'	Depth to hard stratum measured from the current excavation level
σ_{max}	Maximum earth pressure
σ_{TP}	Terzaghi & Peck earth pressure
μ_R	Deflection ratio
D	Penetration depth
λ_h	Percentage of excavation depth for wall deflection
λ_v	Percentage of excavation depth for surface settlement
P_f	Probability of failure
$P_{f,m}$	Modified failure probability

Chapter 1

INTRODUCTION

1.1 Overview

With rapid growth in urban development, more and more excavations projects for high-rise buildings and subway lines are being executed and scheduled. Most of the current empirical and semiempirical methods for assessing the excavation behavior are mostly based on excavations with flexible walls. There is therefore a need for simplified methods to evaluate the behavior of excavations with diaphragm walls in soft clay. The first aim of the project is to obtain reasonable predictions on excavation behavior by conducting a series of parametric studies.

The second aim of the project is to look at the viability of applying reliability analysis in this field for assessing the performance of excavation system with the objective of ensuring economy and safety. To minimize the damage to adjacent buildings and avoid failure of the excavation itself, wall deflection and soil settlement are the most critical factors in the excavation process. So this project will focus on these two factors when conducting reliability analysis.

1.2 Objective and Scope of the Research

This research has three main objectives which are

1. To reflect the characteristic of wall deflection and soil settlement more accurately by considering the small strain behavior of soil.
2. To set up a simplified model for estimating wall deflection and soil settlement after performing a series of practical case studies and hypothetical analyses. And
3. To assess the reliability of braced excavation systems with focus on the deformation assessment.

1.3 Outline of the Thesis

In chapter 2, the relevant literature on the subject of excavations is summarized, focusing on the excavation behavior and the basic concepts of reliability. The commercial finite element program—PLAXIS mainly used in this paper is introduced and the soil models are described.

In chapter 3, cases studies are presented to demonstrate the use of the HSS (Hardening small-strain) model in PLAXIS to estimate wall deflection and soil settlement. The difference between HSS and HS (Hardening soil) predictions is illustrated by a set of parametric studies. A coefficient is provided to assess the small strain effect on wall deflection.

In chapter 4 the results of a comprehensive parametric study are presented. The factors affecting the excavation behavior are studied. The response surfaces for predicting wall deflection and surface settlement are generated by the response surface method. A method for predicting the maximum apparent pressure is proposed.

In chapter 5 the reliability analyses is illustrated by two examples. The factors affecting the failure probability are studied to find the critical factors. Simplified charts are provided to assess the failure probability for wall deflections and surface settlements.

Chapter 2

LITERATURE REVIEW

2.1 Overview

The main aspects in the design of excavation system are the estimation of basal heave, the wall deflection, soil settlement, strut forces and wall bending moment. These are reviewed in chapter 2, followed by an overview of small strain soil behavior, reliability concepts and PLAXIS small strain model.

2.2 Basal Heave Stability

Terzaghi (1943) developed Eq. (2.1) and Eq. (2.2) to compute the factor of safety (FS) for basal heave stability. It is a method applicable for wide excavations $(\mathrm{B/H} > 1)$ with the limitation that the FS is independent of wall penetration, wall stiffness and adhesion.

For $r > 0.7B$:

$$FS = \frac{5.7c_{u2}}{H\left(\gamma - \frac{c_{u1}\sqrt{2}}{B}\right)} \tag{2.1}$$

And for $r < 0.7B$:

$$FS = \frac{5.7c_{u2}}{H\left(\gamma - \frac{c_{u1}}{B}\right)} \tag{2.2}$$

where c_{u1}, c_{u2} is the undrained soil shear strength of the soil above and below the excavation level respectively, and H, B, r are the depth of the excavation, the width of the excavation and the depth to firm layer respectively as shown in Figure 2.1.

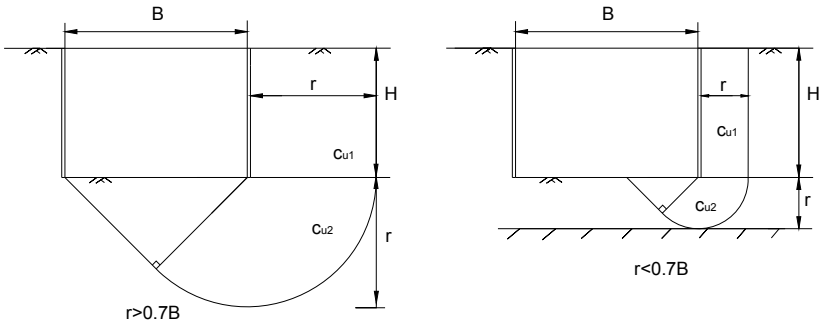

Figure2.1 Bottom Heave Analysis for Wide Excavation $(B/H > 1)$ (Terzaghi,1943)

Bjerrum and Eide (1956) proposed a method as shown in Figure 2.2 and Eq. (2.3) for estimating factor of safety against basal heave for narrow excavations $(B/H \leq 1)$. It has been validated by many case records with different shapes. The effect of clay thickness is ignored and the effect of wall penetration and stiffness are also not included.

$$FS = N_c \frac{c_u}{\gamma H + q} \tag{2.3}$$

where N_c is the bearing capacity coefficient and q is the surcharge load.

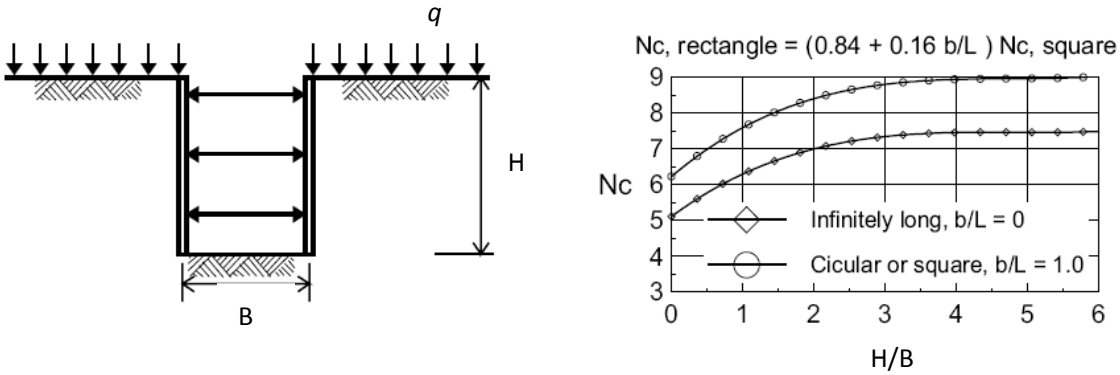

Figure2.2 Bottom Heave for Deep Excavation $(B/H \leq 1)$

(Bjerrum and Eide, 1956)

Goh (1994) suggested an approach considering the effect of wall penetration, wall stiffness and clay thickness for wide excavation ($B/H > 1$). However, the excavation shape effect is not included and c_u should be constant. The FS is given by

$$FS = \frac{c_u N_h}{\gamma H + q} \mu_t \mu_d \mu_w \tag{2.4}$$

where N_h is bearing capacity factor, and μ_t, μ_d, μ_w are the clay thickness factor, wall penetration factor and wall stiffness factor, respectively as shown in Figure 2.3.

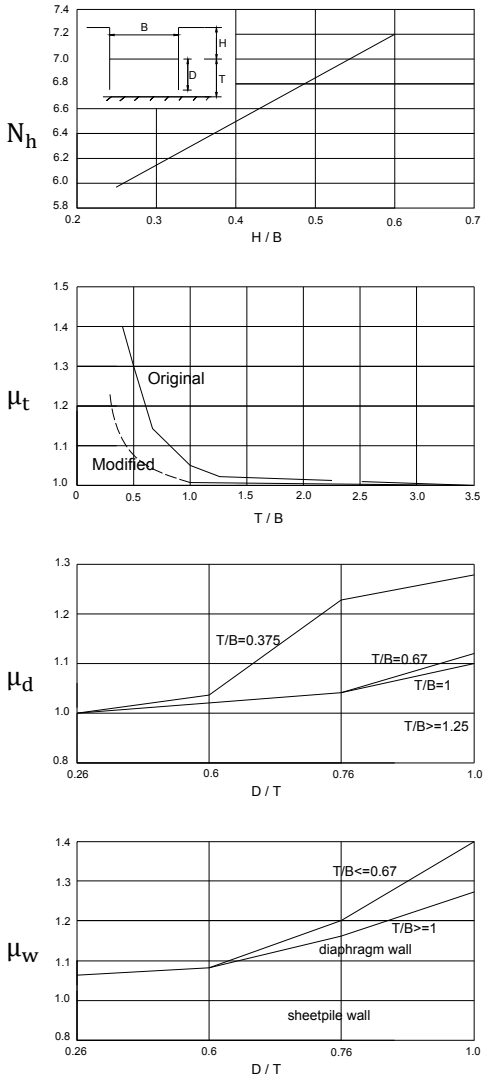

Figure 2.3 N_h, μ_t, μ_d, and μ_w (Goh, 1994)

2.2 Lateral Wall Deflection, δ_{hm}

Mana and Clough (1981) introduced the relationship between the maximum wall deflection (δ_{hm}) and factor of safety against basal heave defined by Terzaghi (1943) after studying a number of excavation case histories in soft to medium clays. As the chart in Figure 2.4 shows, when the factor of safety was less than 1.5, the maximum wall deflection increased rapidly.

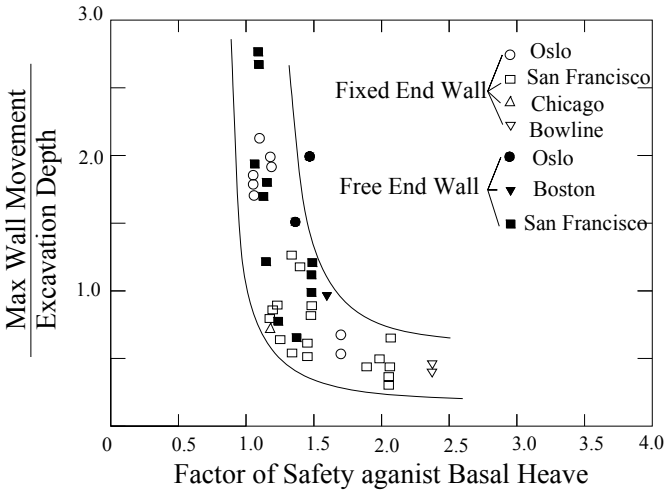

Figure 2.4 Relationship between Factor of Safety Against Basal Heave and Non-dimensionalized maximum Lateral Wall Movement from Case History Data (Mana and Clough,1981)

Wong and Broms (1989) studied the effects of factor of safety against basal heave, excavation width, depth to hard stratum and wall stiffness on lateral wall deflection based on several series of finite element analyses. They concluded that the factor of safety against basal heave which was related to the soil undrained shear strength mainly controlled the lateral displacement as shown in Figure 2.5. They also pointed out the structural system including wall stiffness, preloading and strut spacing heavily affected the wall deflection. They proposed a simple procedure to

estimate the maximum wall deflection for a braced excavation in soft clay. The method was based on the important assumptions of no net volume change and the yielding of zone c governed the lateral wall movement as shown in Figure 2.6.

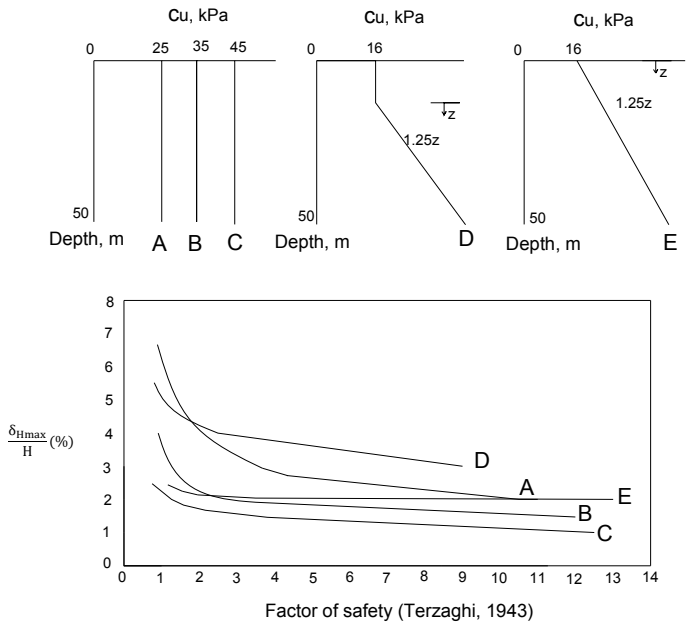

Figure 2.5 Effect of Factor of Safety on Wall Deflection (Wong and Broms, 1989)

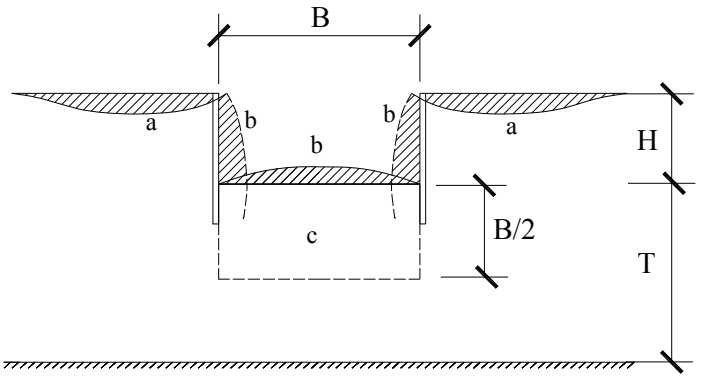

Figure 2.6 Movements around Braced Excavation (Wong and Broms, 1989)

Clough and O'Rourke (1990) proposed a semi-empirical chart (Figure 2.7) for estimating δ_{hm} for soft to medium clays, which can simultaneously consider the factor of safety against basal heave and system stiffness ($EI/\gamma_w h_{avg}^4$, where EI is wall stiffness, h_{avg} is average vertical strut spacing and γ_w is unit weight of water).

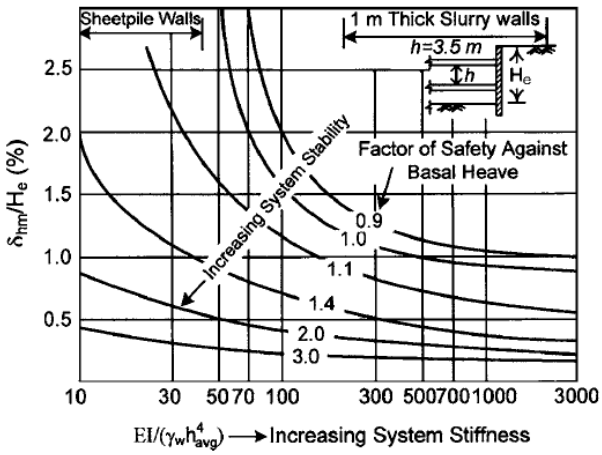

Figure 2.7 Design Curves to Obtain Maximum Lateral Wall Movement for Soft to Medium clays (Clough and O'Rourke, 1990)

Wong et al. (1997) presented and discussed the data collected from construction of the tunnels in the Central Expressway (CET) Phase Ⅱ of Singapore. The results in Figure 2.8 showed the wall movements were less than 0.5%H and 0.35%H, when the thickness of soft-soil layers was less than 0.9H and 0.6H overlying stiff soils, respectively. The wall types that affected wall deflection were illustrated in the Figure 2.8. It indicated that stiffer wall stiffness would reduce the movement significantly with thick soft layer at sites if it excluded the two cases supported by contiguous bored pile walls where the maximum lateral wall movement was slightly less than 0.5%H. They also illustrated and explained the effect of prop type on the maximum wall deflection in Figure 2.9, which showed anchored excavations result in smaller wall deflection.

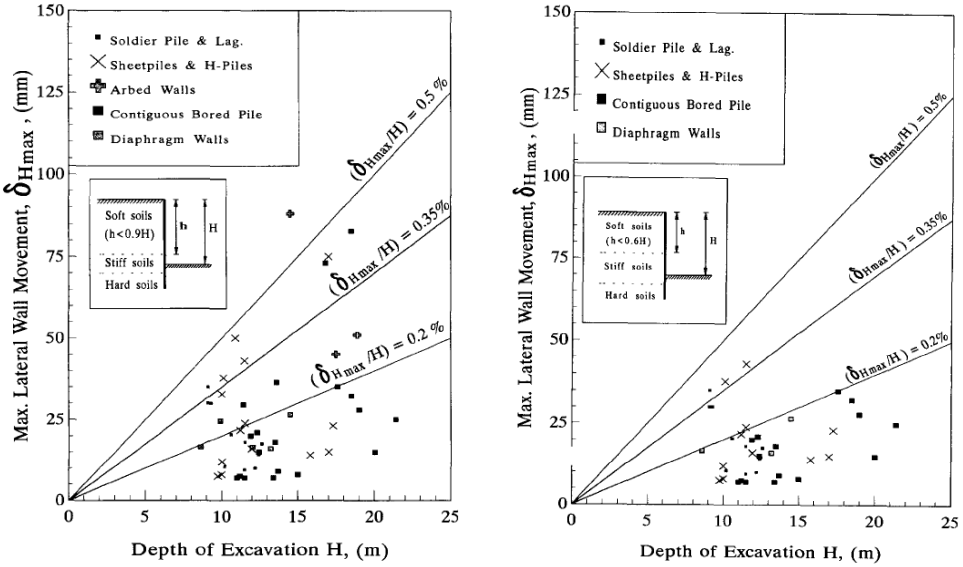

Figure 2.8 Observed Maximum Lateral Wall Deflection for Excavation by Five Types of Walls (left, h<0.9H and right, h<0.6H) in the Construction of CTE Phase Ⅱ (Wong et al., 1997)

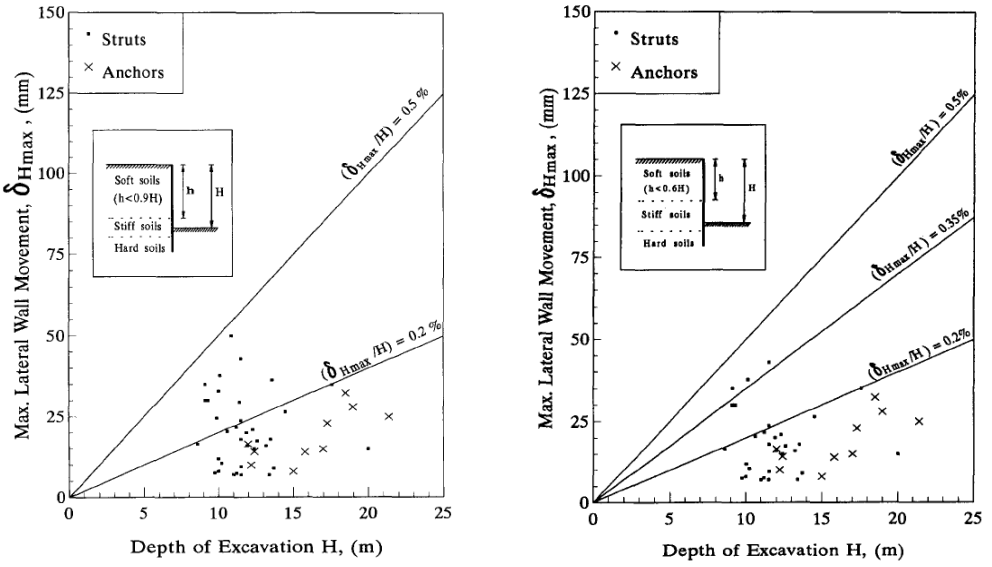

Figure 2.9 Effect of Prop Type on Maximum Lateral Wall Movements for Excavations Supported by Five Types of Wall (left, h<0.9H and right, h<0.6H) in the Construction of CTE Phase Ⅱ (Wong et al., 1997)

Yoo (2001) showed the same effect of wall type, strut type on the wall deflection as Wong et al. (1997), which was based on the data collected from sites as well as from hypothetical cases performed with FEM in multilayered ground condition of residual soils overlying rock stratum. The average value $\delta_{hm} = 0.12\%\text{H}$ they concluded is smaller than the $0.2\%\text{H}$ reported by Clough and O'Rourke (1990) due to the underlying rock constrains the wall movement at toe. The analysis showed the effect of system stiffness ($EI/\gamma_w h_{avg}^4$) played a significant role on wall deflection in Figure 2.10. Figure 2.11 indicated the stiffer system stiffness had more pronounced effect on wall movements in a less stiff soil environment. Figure 2.12 demonstrated the interaction between wall stiffness and strut spacing for wall movements. It indicated the efficient way to decrease the wall movement is by reducing the support spacing for less stiff wall stiffness.

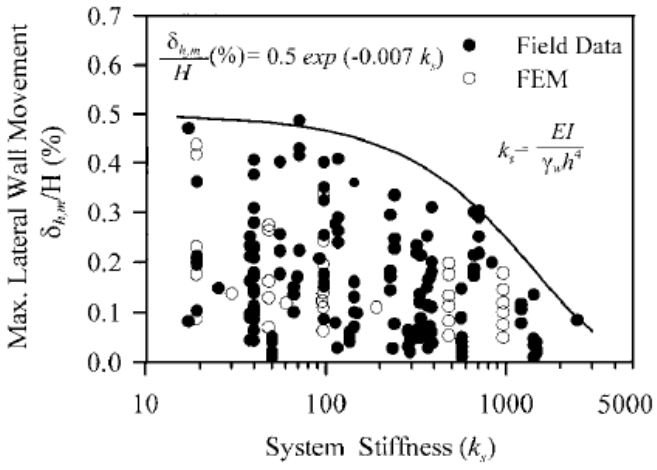

Figure 2.10 Variation of $\delta_{h,m}/H$ with System Stiffness (Yoo, 2001)

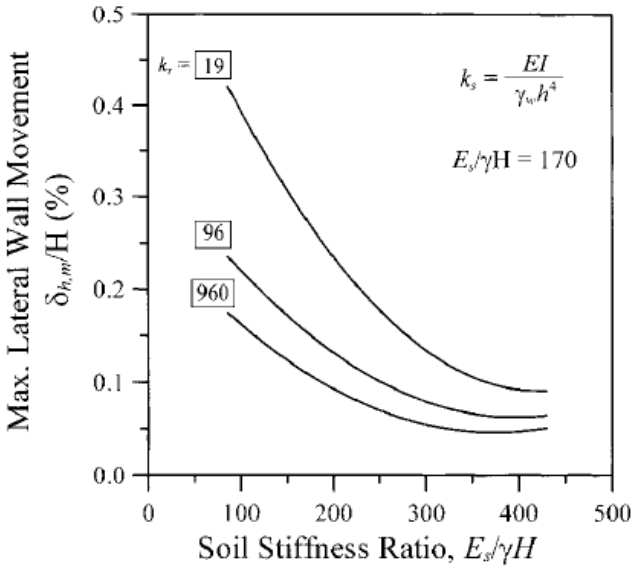

Figure 2.11 Variation of $\delta_{h,m}/H$ with Retained Soil Stiffness (Yoo, 2001)

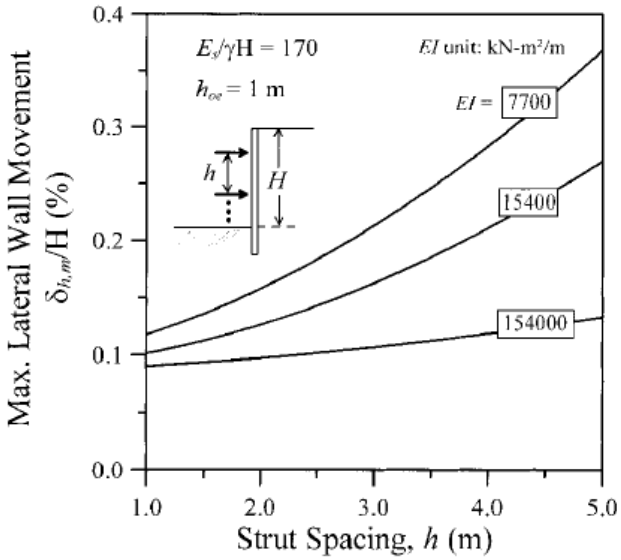

Figure 2.12 Variation of $\delta_{h,m}/H$ with Strut Spacing (Yoo, 2001)

2.3 Ground Surface Settlement

The ground settlement behind the wall is very important as it is directly related to the safety of adjacent buildings and facilities. The settlement may be caused by

excavation behavior, structure installation and dewatering. Because of this complex behavior most approaches predicting for the ground settlement are based on empirical and semi-empirical method.

Peck (1969) summarized the field observations of ground surface settlement around several excavations in a graphical form, this first empirical method to estimate the soil settlement, assumes a spandrel-type settlement profile. The settlement curve is classified into three zones, Ⅰ, Ⅱ, Ⅲ as it shown in Figure 2.13, depending on the type of soil and workmanship. The data shows the settlement is $\delta_{vm} = 1-3\%$H, for excavations supported by sheet piles or soldier piles.

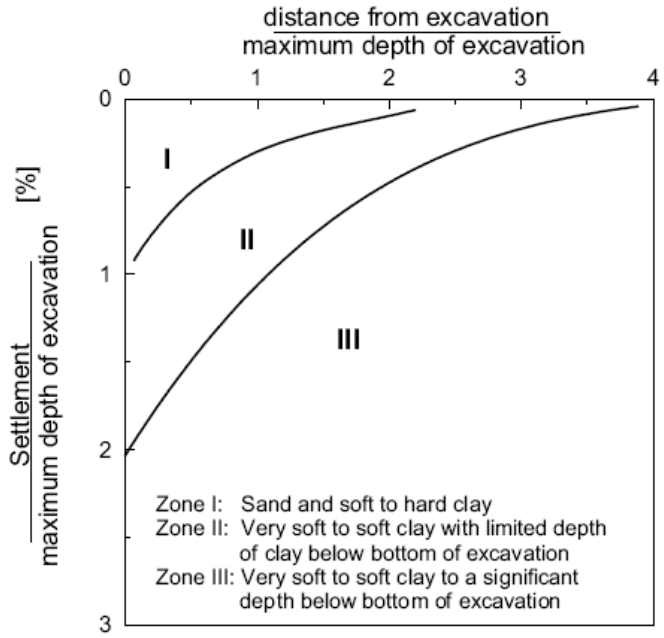

Figure 2.13 Summary of Soil Settlement behind Insitu Walls (Peck, 1969)

The Clough and O'Rourke (1990) charts in Figure 2.14 showed that the surface settlement profile for excavations in sandy soil or stiff clay and soft to medium clay are triangular and trapezoidal shape, respectively. The corresponding settlement

influence zones are defined as a ratio of excavation depth. The envelope for estimating soil settlement in a practical case can be derived when the maximum settlement δ_{vm} is known. The authors reported that the average δ_{vm} is about 0.15%H.

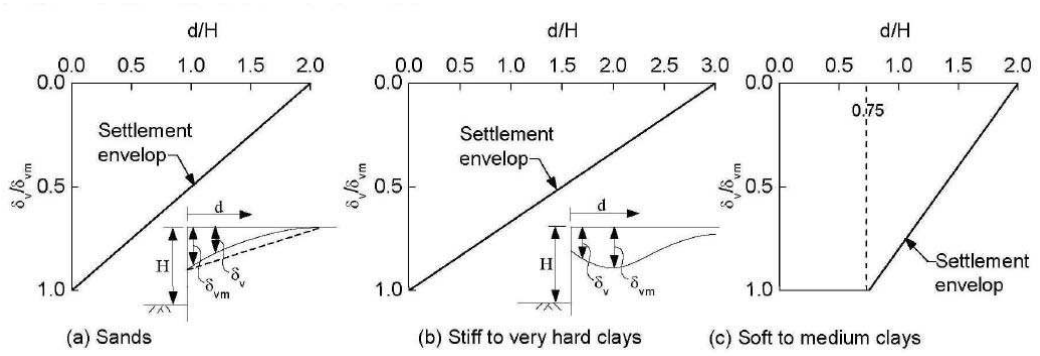

Figure 2.14 Dimensionless Settlement Profiles Recommended for Estimating the Distribution of Settlement adjacent to Excavations in Different Soil Types (Clough and O'Rourke, 1990)

Ou et.al (1993) observed that the vertical movements of the soil behind the wall may extend to a considerable distance. The settlement at a limited distance behind the wall is not uniform and increases with the excavation depth. It proposed a trilinear line for predicting the spandrel-type settlement profile. It also concluded the deformation ratio falls in the range of $0.5 - 1.0\delta_{hm}$ in Taipei.

Hsieh and Ou (1998) proposed a method for estimating the ground surface settlement for both concave and spandrel settlement profiles in Figure 2.15, which are divided into two parts, the primary influence zone and the secondary influence zone. The proposed method much depends on the accuracy of the estimated value of maximum lateral wall movement which can be obtained using numerical methods.

The types of settlement profiles are related to the magnitude of the cantilever component (A_c) and deep inward component (A_s) as shown in Figure 2.16. They suggested $A_s = 1.6A_c$ was the boundary for the two types from case studies, and $A_s < 1.6A_c$ is for spandrel type and $A_s > 1.6A_c$ is for concave type.

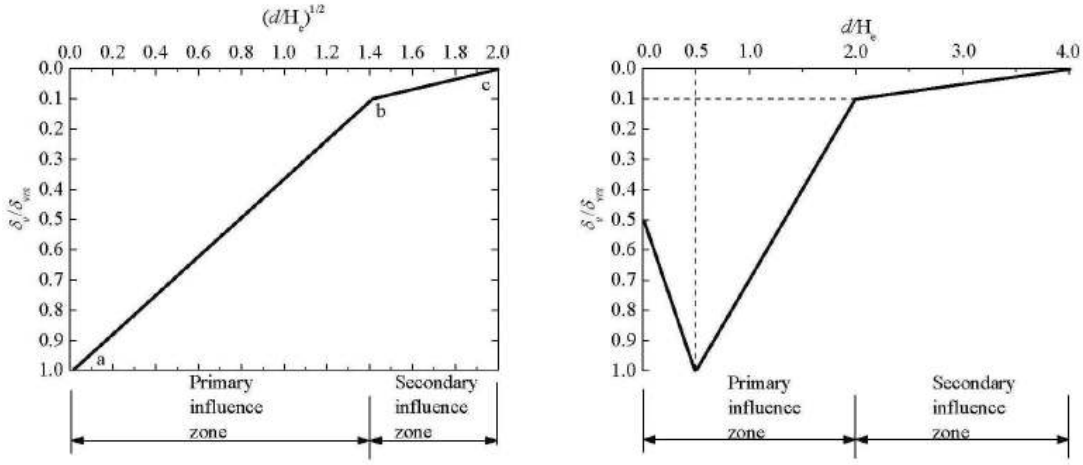

Figure 2.15 Proposed Method for Predicting Spandrel and Concave Settlement (Hsieh and Ou, 1998)

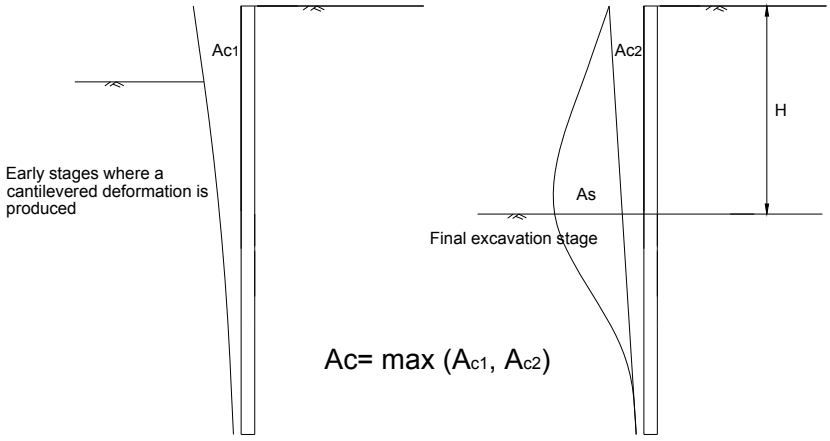

Figure 2.16 Definitions of the Area of the Deep Inward Part and the Cantilevered Part of the Wall Deflection (Hsieh and Ou, 1998)

Kung et.al (2007a) developed a modified profile of Hsieh and Ou (1998) through a number of practical cases records and numerical case studies of braced excavations in soft to medium clays. They also proposed that the maximum surface settlement can be estimated from the relationship between δ_{vm} and δ_{hm}, which be expressed as: $\delta_{vm} = \mu_R \delta_{hm}$ where μ_R = deformation ratio. The factors affecting the deformation ratio R were soil shear strength, Young's modulus, and the clay-layer thickness relative to wall length. Figure 2.17 shows the modified settlement profile, which only modifies the magnitude of settlement adjacent the wall compared with Hsieh and Ou (1998).

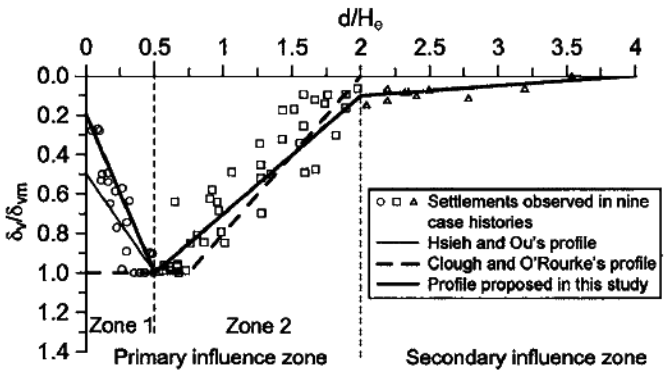

Figure 2.17 The Proposed Surface Settlement Profile (trough) and other Data (Kung et.al, 2007a)

2.4 Apparent Earth Pressure

The support system is composed of wall and struts or anchors which are installed prior to the process of excavation. Ensuring the safety of the structural system is important.

Terzaghi and Peck (1967) and Peck (1969) recommended the widely used apparent earth pressure diagram, to estimate the magnitude and distribution of prop loads.

They proposed different earth pressure diagrams for braced excavation in sands, stiff fissured clays and soft to medium clays as shown in Figure 2.18, where φ is effective friction angle for sand and $N_S = \gamma H/c_u$ is the stability number for clay. This method was developed based on data from flexible wall. The pressure diagrams are difficult to use in multi-layered ground conditions. Its applicability to long-term conditions also needs to be verified.

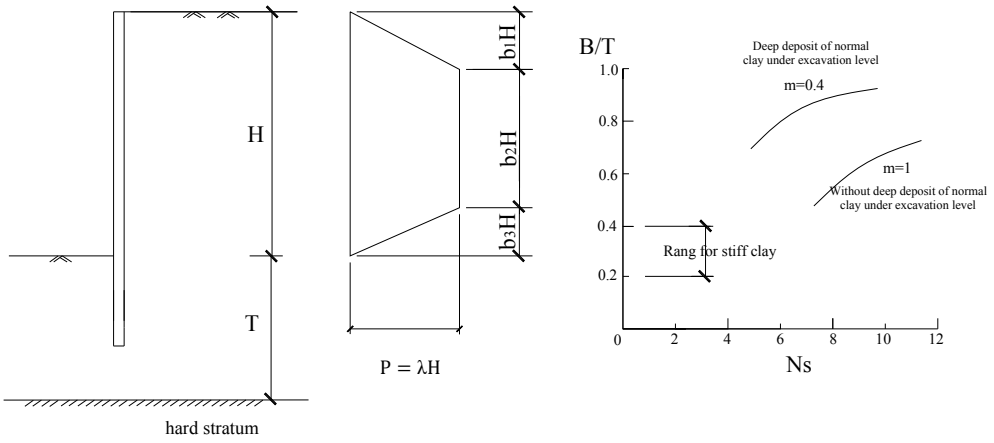

Soil Type	b_1	b_2	b_3	λ	K_A	Normal range of λ
Sand	0	1.0	0	$\beta = 0.65K_A\gamma$	$\tan(45-\varphi/2)^2$	0.2γ
Soft to medium clay ($N_S > 5\ or\ 6$)	0.25	0.75	0	$\beta = K_A\gamma$	$1 - m(4c_u/\gamma H)$	0.4γ~0.8γ
Stiff fissured clay ($N_S < 4$)	0.25	0.50	0.25	$\beta = 0.2\gamma$~0.4γ	–	0.3γ

Figure 2.18 Apparent Pressure Diagram for Calculating Strut Loads (Terzaghi and Peck, 1967)

Chang and Wong (1996) pointed out the Terzaghi and Peck method underestimate the apparent pressure for diaphragm walls in soft clay. They suggested the Terzaghi-Peck APD should be increased by a factor of 2 for deep clay deposit ($T/B \geq 1$) for diaphragm walls in soft clay, and for shallow clay deposit ($T/B < 1$) this factor can be reduced.

Twine and Roscoe (1997) presented the CIRIA report for prop loads. They recommended the term 'distributed prop load' (DPL) rather than apparent pressure to estimate the prop load. The DPL includes the maximum loads at each propping level, which frequently occur at different stages of excavations. Different DPL diagrams were proposed for different scenarios with different wall stiffness and soil stiffness.

For the Singapore CTE project, Wong et al. (1997) observed that the maximum apparent earth pressure was about $0.6\gamma H$, $0.4\gamma H$, and $0.25\gamma H$ for excavation with thickness of soft-soil layers of less than $0.9H$, $0.8H$, and $0.6H$ overlying stiff soils, respectively as shown in Figure 2.19. It suggested that most data were within the vertical boundary of the apparent earth pressure diagram proposed by Terzaghi and Peck (1967). However, the diagram should extend to the ground surface instead of decreasing to zero to fit all data. This trend may be caused by the high position of the first prop level (close to ground surface) and the application of preload.

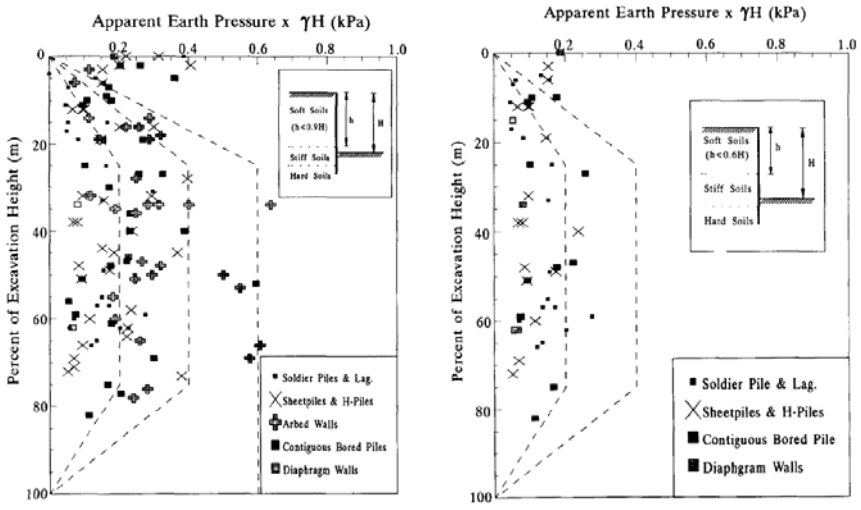

Figure 2.19 Apparent Earth Pressure Diagram for Excavation Supported by Five Types of Wall (left, h<0.9H and right, h<0.6H) in the Construction of CTE Phase Ⅱ (Wong et al., 1997)

2.5 Bending Moment

The bending moments are related with the wall stiffness and curvature of the wall. The curvature of the wall is dependent on the wall deflection induced by the soil excavation.

Hashash and Whittle (1996) analyzed excavation behavior based on nonlinear finite-element analyses considering small strain with MIT-E3 model. It presented a variety of the wall bending moment as functions of factors affecting excavation performance in Figure 2.20 to Figure 2.21, as wall deflections were also involved. One point had been noted that the maximum bending moment could control the failure mechanism if it exceeded the ultimate bending moment of the applied wall with larger excavation depth and less strut spacing.

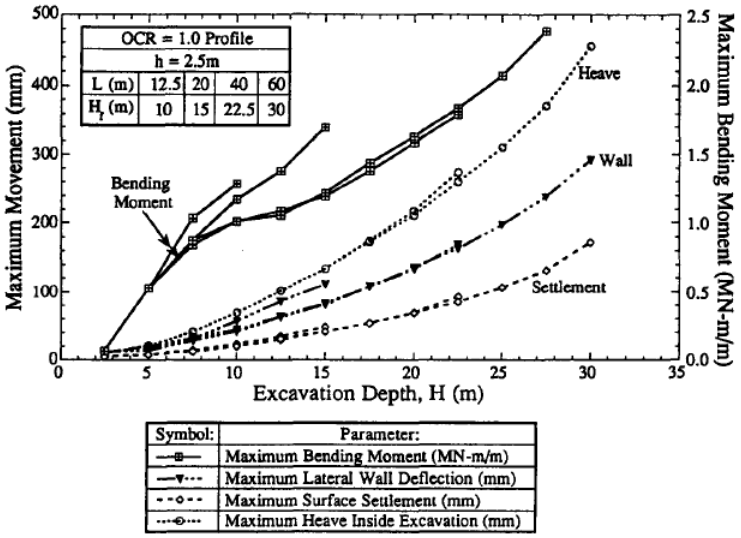

Figure 2.20 Effect of Wall Length on Maximum Wall Bending Moments, Deflections, and Ground Movements (Hashash and Whittle, 1996)

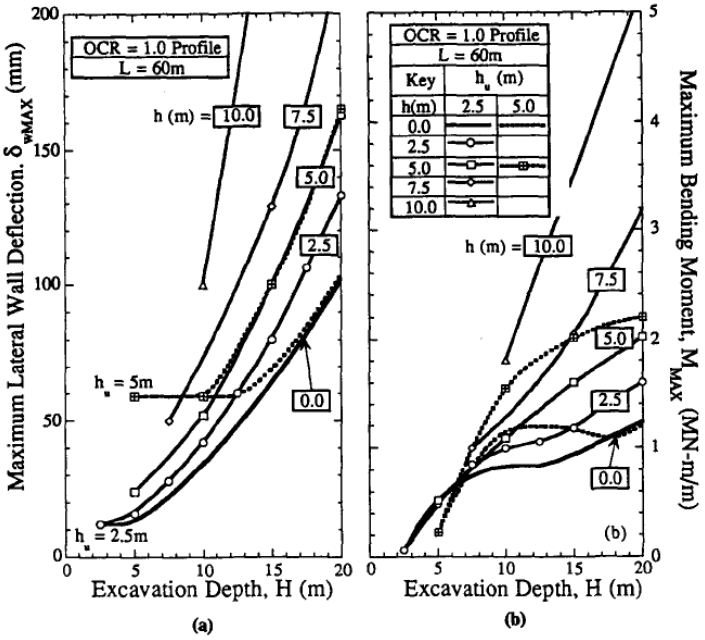

Figure 2.21 Effect of Strut Spacing on Maximum Wall Bending Moment and Maximum Lateral Deflection (Hashash and Whittle, 1996)

2.6 Earth Pressure

Lambe and Whitman (1969) and Hashash and Whittle (2002) illustrated the arching mechanism and its effect on earth pressure distribution which resulted in larger pressure in the upper retained soil through numerical analysis as shown in Figure 2.22 and Figure 2.23, respectively. The hypothetical cases modeled by Hashash and Whittle (2002) were in the condition of pure soft clay and with free toe of the wall. They also showed the arching mechanism was independent on stress history profile and soil model.

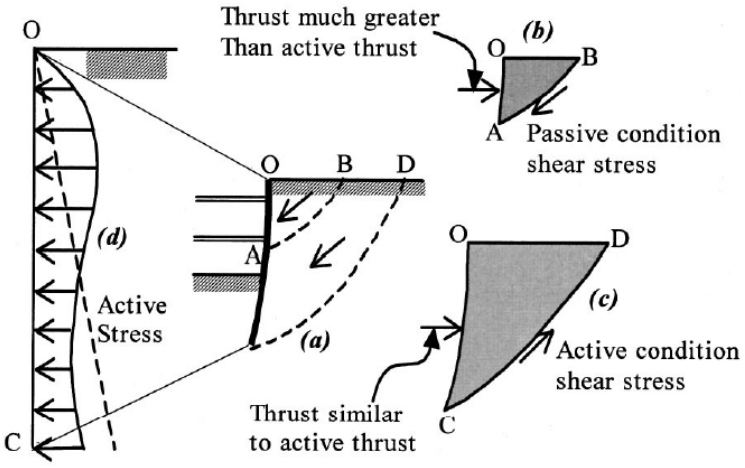

Figure 2.22 Active Arching Mechanism for Braced Excavation

(Lambe and Whitman, 1969)

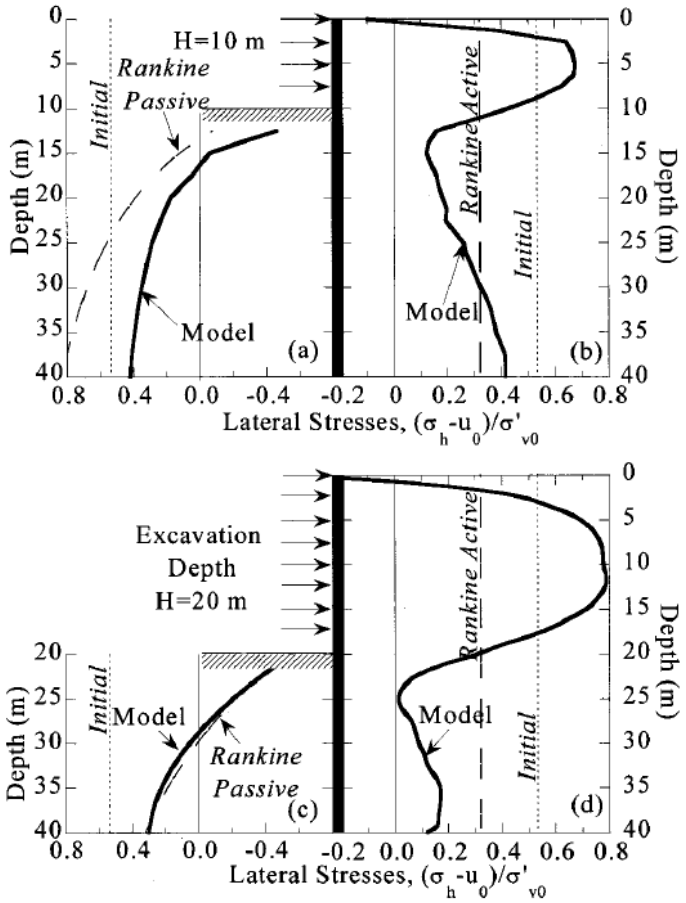

Figure 2.23 Predictions of Total Lateral Stresses Acting on Diaphragm Wall

(Hashash and Whittle, 2002)

2.7 Effect of Small Strain on Excavation Behavior

Jardine et.al (1986) was the first to apply small strain concepts to excavation problems. Using a simple empirical expression for soil stiffness (Figure 2.24) from the laboratory measured stress-strain relationships, which considered the high stiffness at small strain stage, for a simple excavation problem, the finite element analysis showed distinct differences between the mentioned model and linearly elastic soil model (Figure 2.25).

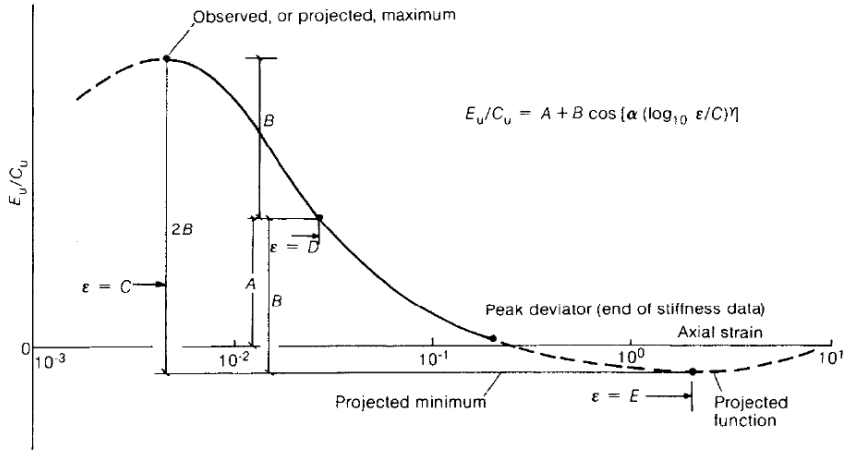

Figure 2.24 Curve and Equation Fitting to Stiffness-Strain Data (Jardine et.al, 1986)

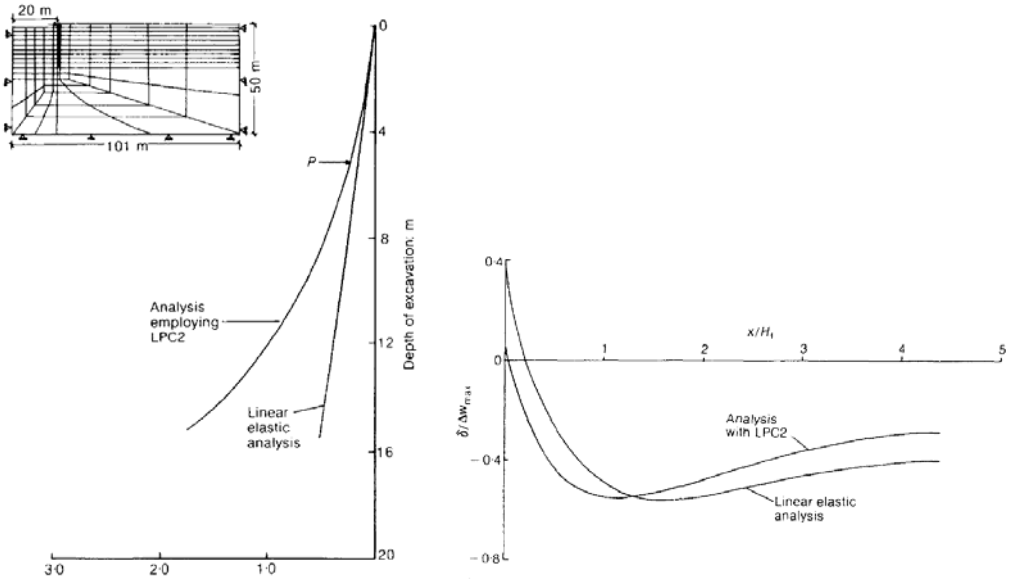

Figure 2.25 Wall Deflection and Surface Settlement (Jardine et.al, 1986)

Whittle and Hashash (1994) simulated the ground settlement and movement more accurately and realistically with the soil model—MIT-E3 (Whittle & Kavvadas, 1994) compared with the Modified Cam-Clay model (MCC), which illustrated the role of small strain and anisotropic stress-strain behavior in soil. Figure 2.26 showed the difference between MIT-E3 and MCC in predicting wall deflection and

bending moment. The results for the MCC model show that the rate of maximum wall deflection actually decreases as excavation proceeds. In contrast, MIT-E3 predicts rapidly increasing wall deflections and bending moments which reflect the development of a failure mechanism. Figure 2.27 presented significant settlements and lateral displacements at locations very far from the excavation by MCC while MIT-E3 predicts much more realistic settlements occur within 20-30m of the excavation.

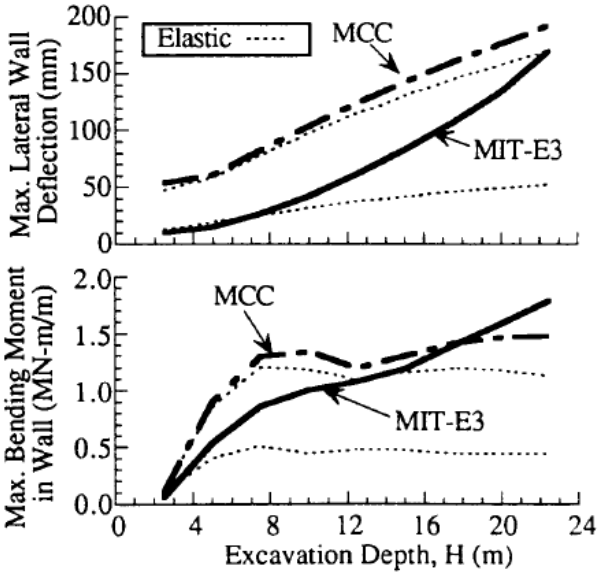

Figure 2.26 Maximum Wall Bending Moment and Lateral Deflection

(Whittle and Hashash, 1994)

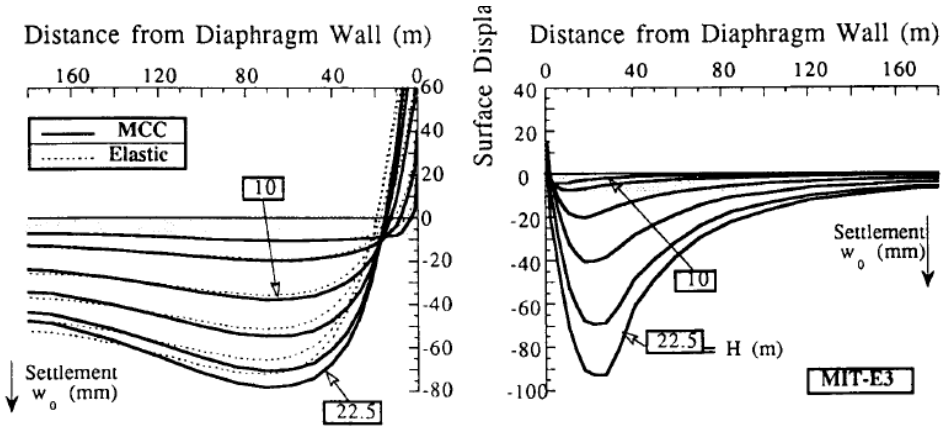

Figure 2.27 Summary of Predicted Ground Surface Movements

(Whittle and Hashash, 1994)

Kung et.al (2007a) and Kung et.al (2008) showed the importance of stress-strain characteristic of soils at small strains with the modified pseudo plasticity (MPP) model and the three-Surface Kinematic Hardening model (3-SKH) both through back-analysis of the TNEC project in Taipei. The wall deflection and surface settlement of TNEC project were both modeled by the two models. Figure 2.28 showed the predicted results of Type-A with 3-SKH which agreed well with the observation and compared with the other predictions which were modeled with MCC.

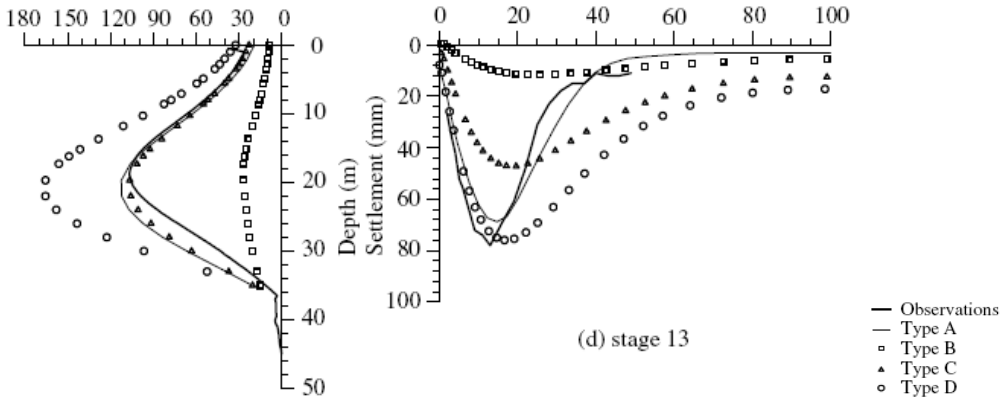

Figure 2.28 Predictions versus Observations of Wall Deflection and Surface Settlement in TNEC Excavation Case (Kung et.al, 2008)

2.8 Basic Reliability Concept

2.8.1 Introduction

The conventional design method used in many geotechnical designs projects relies on some forms of safety factor to provide a margin of safety against failure. This approach does not reflect the underlying uncertainties and cannot determine the performance of the excavation system precisely particularly in relation to wall and ground movements. In order to overcome this limitation, a more rational approach based on the reliability concepts is used in this project. The section provides an overview of the basic concepts underlying reliability analysis.

2.8.2 Reliability Index

Many researchers assess the safety of a system by establishing a relationship between the load S of the system and the resistance R. Typically this is expressed as

$$G(\mathrm{x}) = R - S = 0 \tag{2.5}$$

where x is the vector of the random variables. Mathematically, $R > S$ or $G(\mathrm{x}) > 0$ would denote a 'safe' domain, and $R < S$ or $G(\mathrm{x}) < 0$ would denote a 'failure' domain. Eq. (2.5) which is the boundary of two states is called the *limit state function* (LSF). If R and S are random in nature, they can be characterized by their probability density function (f_S, f_R), as depicted in Figure 2.29, where m_S and m_R are the mean value for the two variables S and R, respectively.

Due to the uncertainties in the variables of LSF, it is impossible to predict the state of system with absolute certainty. The feasible way is to assess the probability of

'failure'. The calculation of the probability of 'failure' involves the determination of the joint probability distribution of R and S and the integration of the probability density function (pdf) over the failure domain as indicated by the volume *abcd* in Figure 2.30 (Goh, et al., 2005). Mathematically, the probability of 'failure' P_f is assessed as

$$P_f = P(R < S) = \int_{G(X)\leq 0} f(X)dx \tag{2.6}$$

where X is the random variable and $f(X)$ is the joint density function of R and S.

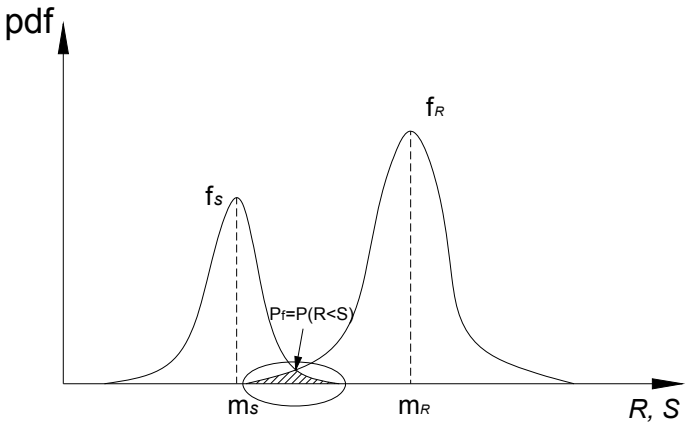

Figure 2.29 Probability Density Function of *R* and *S*

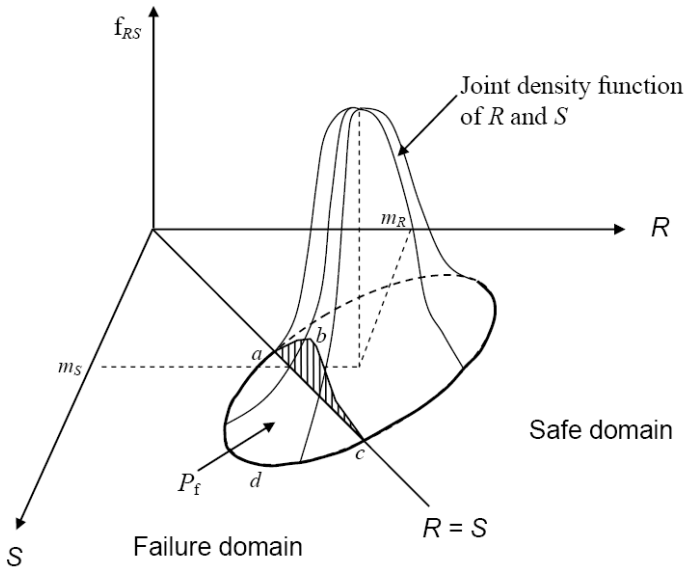

Figure 2.30 Joint Probability Distribution Function (pdf) for Two Variables (Goh, et al., 2005)

For a problem with multiple *n* random variables, the calculation of P_f involves the determination of a multi-dimensional joint probability density function of the random variables and the integration of the pdf over the failure domain $G(\mathrm{x}) < 0$.

For many geotechnical problems, the pdf of the variables are not known. An approximate method to assess P_f is using the *reliability index* β. Mathematically, the reliability index β of the system is often expressed as

$$\beta = -\Phi^{-1}(P_f) \tag{2.7}$$

where Φ^{-1} is the inverse of the standard normal cumulative distribution function.

Many methods have been developed to assess the reliability index, including the First Order Reliability Method (FORM), Second Order Reliability Method (SORM), Point Estimate Method (PEM), Monte Carlo Method, and so on. The FORM is

widely used in Civil Engineering due to its convenience and efficiency, and is adopted herein.

2.8.3 FORM

2.8.3.1 Basic Concepts

The term 'First Order' indicates that the limit function is linearized as shown in Figure 2.31, where x_1, x_2 are random variables . The linearization of the limit state is carried out at the so called 'Design Point', which is the point on the limit state ($G(x) = 0$) with the highest probability density (Schweckendiek, 2006).

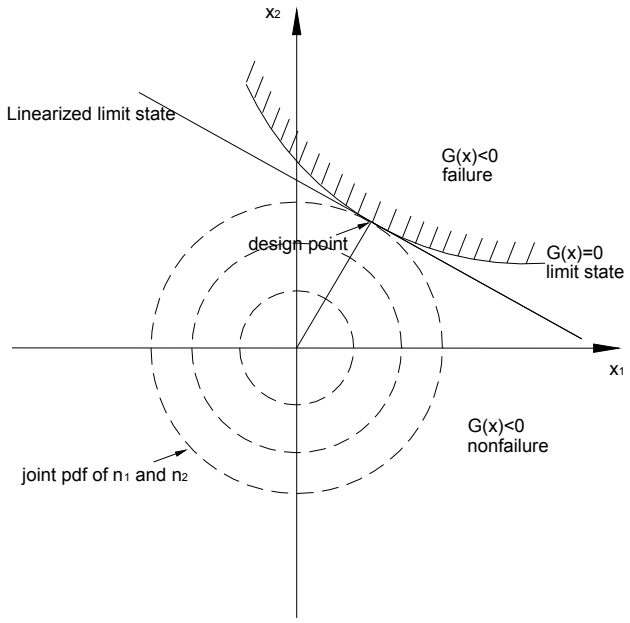

Figure 2.31 Design Point and Linearized Limit State for Two Dimensions (Schweckendiek, 2006).

The first to apply this concept is Cornell (1969), where β is expressed as

$$\beta = \frac{m_G}{\sigma_G} = \frac{m_R - m_S}{\sqrt{(\sigma_R^2 + \sigma_S^2)}} \tag{2.8}$$

where m_G, σ_G and m_R, σ_R and m_s, σ_s are the mean value, standard deviation for G and R and S, respectively. The method is limited to statistically independent normally or lognormally distributed variables. It is also not invariant to the formulation of the limit state. Hence different results are obtained for LSF-formulations in terms of safety factors ($R/S < 1$) and in terms of margins of safety ($R - S < 0$) when using this method.

Hasofer and Lind (1974) developed an alternative method known widely as FORM to assess the reliability index. The reliability index defined by Hasofer and Lind (1974) is illustrated in Figure 2.32 for uncorrelated variables, where m_1, σ_1, and m_2, σ_2 are the mean value and the standard deviation of variables of X_1 and X_2. The reliability index β can be regard as the distance from (m_1, m_2) to the boundary of the failure region directly in units of standard deviations. Further explanations can be found in Ditlevsen (1981), Ang and Tang (1984) and Rackwitz, 2001.

In this method, the random variables are transformed to equivalent standard normally distributed (Gaussian) variables. For normal distributed variables:

$$n_i = \frac{x_i - m_i}{\sigma_i} \tag{2.9}$$

where m_i and σ_i are the mean value and standard deviation for variable x_i.

The distance has to be minimized to find the design point and β (Figure 2.32). Using a Taylor Series Approach (Beacher and Christian, 2003), the reliability index is obtained as

$$\beta = \frac{m_G}{\sigma_G} = -\frac{\sum ni \cdot \left(\frac{\partial G}{\partial n_i}\right)}{\sqrt{\sum \left(\frac{\partial G}{\partial n_i}\right)^2}} \tag{2.10}$$

and

$$\alpha_i = -\frac{\left.\frac{\partial G}{\partial n_i}\right|_{n_i}}{\sqrt{\sum \left(\frac{\partial G}{\partial n_i}\right)^2}} \tag{2.11}$$

where α_i is the 'directional cosine' for n_i or 'influence factor' with the relationships $\beta = \sum n_i \cdot \alpha_i$ and $\sum {\alpha_i}^2 = 1$. The reliability index can be worked out by the Rackwitz-algorithm method (Rackwitz and Fiessler, 1978) or Newton-Raphson scheme.

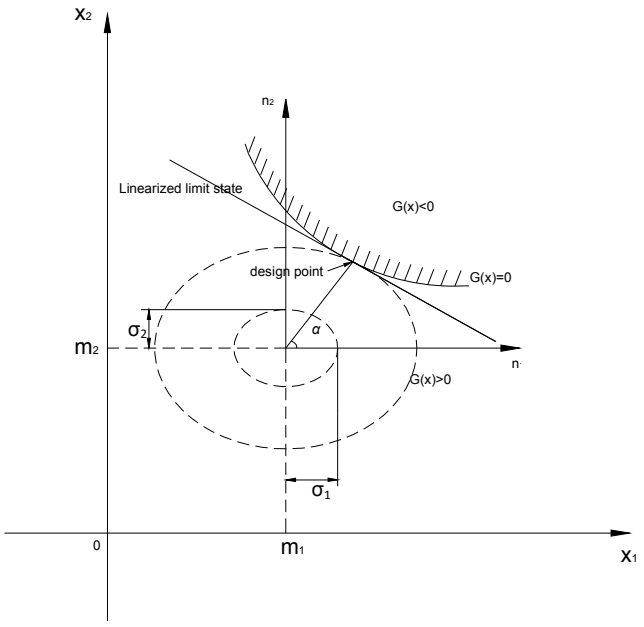

Figure 2.32 Reliability Index for Noncorrelated Variables in x-space

2.8.3.2 Spreadsheet Approach

A alternative expression for Hasofer and Lind (1974)'s index is Eq. (2.12a) (Veneziano, 1974; Ditlevsen, 1981) or equivalently the Eq. (2.12b) (Low and Tang, 1997)

.

$$\beta = \min_{X \in F} \sqrt{[\mathbf{x}-\mathbf{m}]^{\mathbf{T}}[\mathbf{C}]^{-1}[\mathbf{x}-\mathbf{m}]} \tag{2.12a}$$

$$\beta = \min_{X \in F} \sqrt{\left[\frac{\mathbf{x}-\mathbf{m}}{\boldsymbol{\sigma}}\right]^{\mathbf{T}} [\mathbf{R}]^{-1} \left[\frac{\mathbf{x}-\mathbf{m}}{\boldsymbol{\sigma}}\right]} \tag{2.12b}$$

where $\mathbf{x}$ = vector of random variables; $\mathbf{m}$ = vector of mean values; $\boldsymbol{\sigma}$ = vector of standard deviation; $\mathbf{C}$ = covariance matrix of the random variables; $\mathbf{R}$ = correlation matrix; and $\mathbf{F}$ = failure region.

Low (1996) provided a practical and efficient way of using a spreadsheet to calculate the reliability index β for FORM based on Eq. (2.12a). He presented a more intuitive interpretation of the meaning of β as shown in Figure 2.33, where $\beta = \min_{\theta}\left(\frac{R(\theta)}{r(\theta)}\right)$. It showed the Hasofer-Lind index can be calculated by minimizing the quadratic form subject to the constraint that the ellipsoid just touches the surface of the failure region **F**. Low and Tang (1997) used Eq. (2.12b) in preference to Eq. (2.12a) to set up the matrix $[\mathbf{R}]$ and convey the correlation of structure more explicitly when using spreadsheet method. Low and Tang (2007) proposed a new spreadsheet algorithm by changing the dimensionless equivalent standard normal vector (n_i) rather than the (x_i) in the process of invoking the spreadsheet 'Solver'. The method is more efficient and robust compared with the previous method.

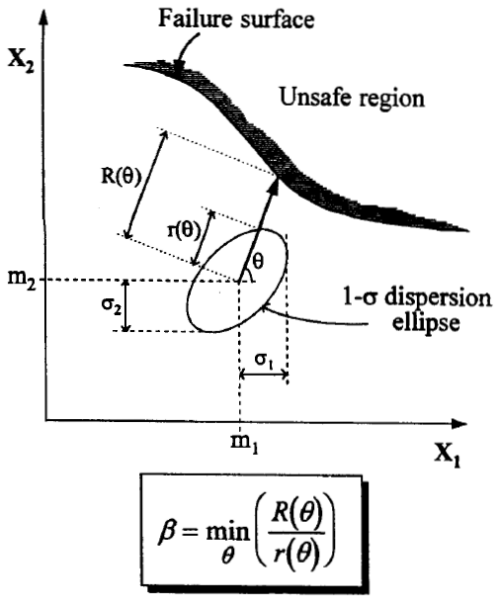

Figure 2.33 Illustrate of Reliability Index β in the Plane (Low, 1996)

Phoon (2004) presented a state-of-the-art review of FORM. He proposed methods to model dependent non-Gaussian random vectors for FORM by using the spreadsheet approach based on Hermite polynomials. He also recommended the concept of Cholesky factorization in calculating the reliability index, which ensures the variables are properly scaled and the correlation matrix is positive definite.

2.8.4 Reliability Applied in Excavations

Limited research work has been done on the subject of reliability applied in excavation performance in recently years. Schweiger (2002) used a point estimate method together with a finite element model to assess the probability of the horizontal displacement of the top of a cantilever sheet pile wall exceeding an arbitrarily predefined value.

Goh et al. (2005) introduced a method of assessing the serviceability performance of excavation system with the reliability index, which can be calculated by using the first-order reliability method and by incorporating a response surface model derived from parametric studies, using a numerical procedure.

Goh and Kulhawy (2005) provided an integrated neural network-reliability method to assess the serviceability performance of braced retaining walls. The reliability index was worked out through the non-linear limiting state surface for wall deflection with the aid of the spreadsheet approach. The limit state surface is obtained through a series of parametric studies by FEM and a neural network model. Two examples were illustrated to show the methodology.

Goh et al. (2008) applied reliability concept in evaluating the basal-heave stability for wide and deep excavations. The uncertainties of this potential failure mechanism were determined by reliability index β, which was defined by Hasofer and Lind (1974) and calculated in a spreadsheet environment. Mathematical expressions, tables, and charts were presented to estimate the probability of basal-heave failure for wide and deep excavations.

Hsiao et al. (2008) conducted reliability analysis on excavation-induced ground settlement based on the KJHH model which was developed by (Kung et al. 2007b) to evaluate the ground settlement. The KJHH model is the response surface with an explicit form for ground settlement and the reliability index is calculated by the spreadsheet approach. Effects of limiting tolerable settlement, variation in soil properties on settlement and sensitivity analysis were analyzed to show the critical factors. They also proposed methods to update the predicted settlements through observed settlement at the current excavation stage, as well as reliability assessment.

2.9 Overview of PLAXIS

2.9.1 PLAXIS

PLAXIS (Brinkgreve and Vermeer, 2002) is a finite element package specifically intended for the simulation and analysis of geotechnical problem. It contains several advanced constitutive models that takes the characteristic of soil with nonlinear, creep, and small strain into consideration. It is capable of performing excavation problem with simple procedures and accurate results. In the following, an overview is given of two advanced soil models used in this project.

2.9.2 Hardening Soil Model

The hardening-soil (HS) model is an advanced model for simulating the behavior of different types of soil, both soft soils and stiff soils (Schanz, 1999). The stress-strain relationship can be well approximated by a hyperbola, which is shown in Figure 2.34. Some basic characteristics of the model are:

c, φ, ψ: cohesion, friction angle and dilatancy angle according to the Mohr-Coulomb model

m : Power for stress-level dependency of stiffness

E_{50}^{ref} : Secant stiffness in standard drained triaxial test

E_{oed}^{ref} : Tangent stiffness for primary oedometer loading

E_{ur}^{ref} : Unloading/reloading stiffness at engineering strains ($\varepsilon \approx 10^{-3} \sim 10^{-2}$)

(default $E_{ur}^{ref} = 3E_{50}^{ref}$)

υ_{ur} : Poisson's ratio for unloading-reloading (default $\upsilon_{ur} = 0.2$)

p^{ref} : Reference stress for stiffness (default $p^{ref} = 100$ stress units)

K_o : Coefficient of earth pressure at rest (default $K_o = 1 - \sin\varphi$)

The relationships between the parameters are as follows:

$$E_{50} = E_{50}^{ref} \left(\frac{c \cos \varphi - \sigma_3' \sin \varphi}{c \cos \varphi + p^{ref} \sin \varphi} \right)^m \quad (2.13)$$

$$E_{ur} = E_{ur}^{ref} \left(\frac{c \cos \varphi - \sigma_3' \sin \varphi}{c \cos \varphi + p^{ref} \sin \varphi} \right)^m \quad (2.14)$$

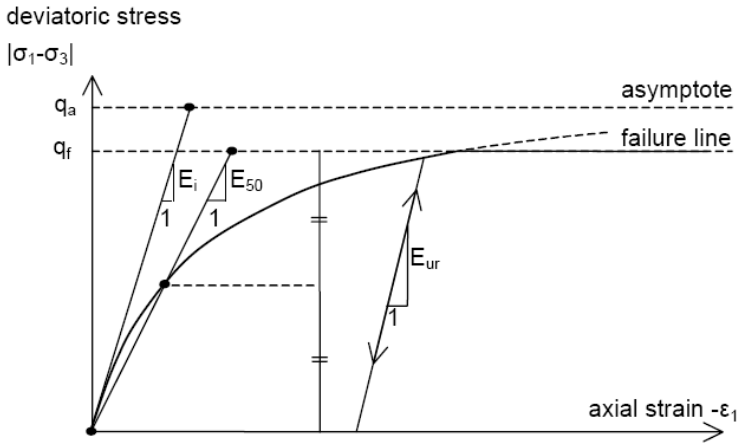

Figure 2.34 Hyperbolic Stress-Strain Relation in Primary Loading for a Standard Drained Triaxial Test (Brinkgreve and Vermeer, 2002)

2.9.3 HSS Model

The model is based on laboratory tests of characteristic stress-strain relationship with special instrumentation. As shown in Figure 2.35, the soil shear modulus is high at very small and small strains. The HSS model is an extension of the HS model.

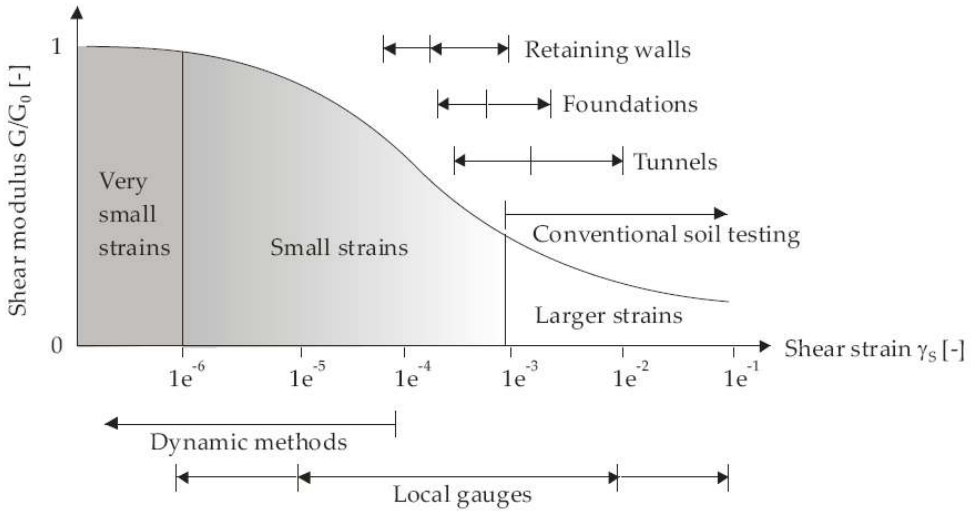

Figure 2.35 Characteristic Stiffness-Strain Behavior of Soil with Typical Strain Ranges for Laboratory Tests and Structures (Atkinson & Sallfors, 1991)

Two additional parameters are added to the HS model to describe small strain.

G_0^{ref} ： reference shear modulus at very small strains ($\varepsilon < 10^{-6}$)

$\gamma_{0.7}$ ： shear strain at which $G_{secant} = G_0$

Values and relationships of these two parameters recommended by PLAXIS manual are presented in Figure 2.36 and Figure 2.37:

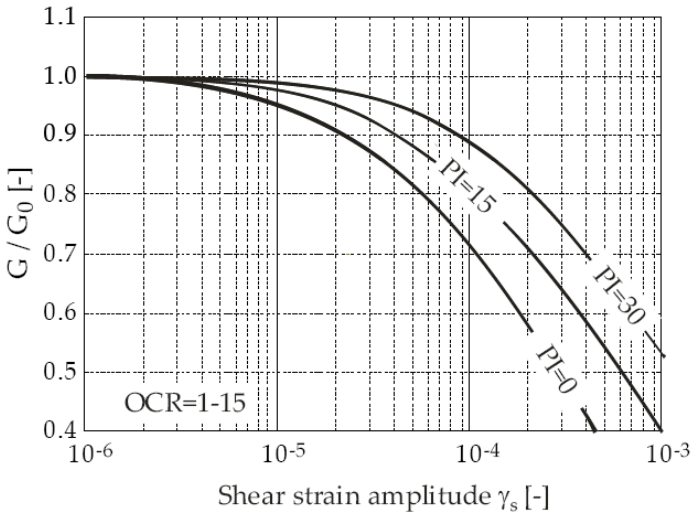

Figure 2.36 Influence of Plasticity Index (PI) on Stiffness Reduction

(Vucetic & Dobry, 1991)

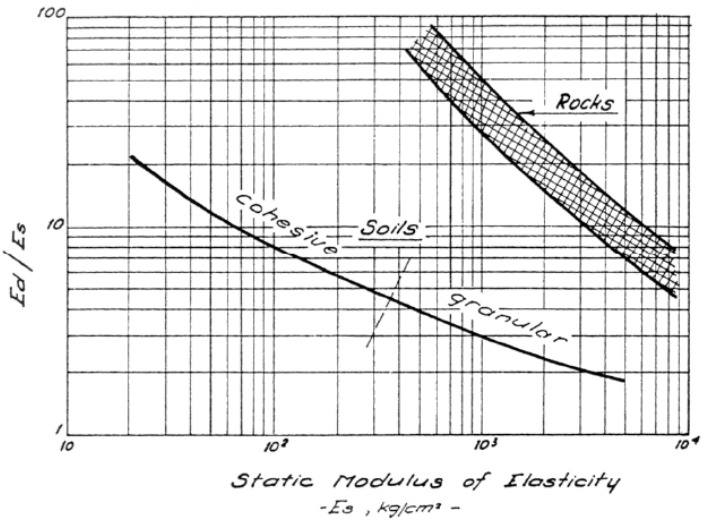

Figure 2.37 Relation between Dynamic ($E_d = E_0$) and Static Soil Stiffness

($E_s \approx E_{ur}$) (Alpan, 1970)

For the case studies in Chapter 3, the G_0^{ref} for soft clays is derived from the chart in Figure 2.37 and some relationships presented in the PLAXIS manual and shown below. The relationships are:

$$E_{50} = E_{50}^{ref}\left(\frac{c\cos\varphi - \sigma_3^{'}\sin\varphi}{c\cos\varphi + p^{ref}\sin\varphi}\right)^m \tag{2.15}$$

$$E_{ur} = E_{ur}^{ref}\left(\frac{c\cos\varphi - \sigma_3^{'}\sin\varphi}{c\cos\varphi + p^{ref}\sin\varphi}\right)^m \tag{2.16}$$

$$G_0 = G_0^{ref}\left(\frac{c\cos\varphi - \sigma_1^{'}\sin\varphi}{c\cos\varphi + p^{ref}\sin\varphi}\right)^m \tag{2.17}$$

$$E_{ur}^{ref} = 3E_{50}^{ref} \tag{2.18}$$

$$E_{ur} = 3E_{50} \tag{2.19}$$

$$G_0^{ref} = \frac{E_0^{ref}}{2(1+\upsilon_{ur})} \tag{2.20}$$

$$G_0 = \frac{E_0}{2(1+\upsilon_{ur})} \tag{2.21}$$

From the chart shown in Figure 2.37:

$$E_d = E_0 \tag{2.22}$$

$$E_s = E_{ur} \tag{2.23}$$

$$\frac{E_d}{E_s} = \frac{E_0}{E_{ur}} = t \tag{2.24}$$

If $c = 0,\ \sigma_3^{'} = K_0\sigma_1^{'},$ we obtain:

$$E_{50}^{ref} = E_{50}/\left(\frac{-\sigma_3^{'}}{p^{ref}}\right)^m \tag{2.25}$$

$$E_{ur} = E_{ur}^{ref}\left(\frac{-\sigma_3^{'}}{p^{ref}}\right)^m \tag{2.26}$$

$$G_0 = G_0^{ref}\left(\frac{-\sigma_1^{'}}{p^{ref}}\right)^m \tag{2.27}$$

$$G_0 = \frac{E_0}{2(1+\upsilon_{ur})} = \frac{tE_{ur}}{2(1+\upsilon_{ur})} = \frac{tE_{ur}^{ref}}{2(1+\upsilon_{ur})}\left(\frac{-\sigma_3^{'}}{p^{ref}}\right)^m \tag{2.28}$$

$$G_0^{ref} = \frac{G_0}{\left(\frac{-\sigma_1^{'}}{p^{ref}}\right)^m} = \frac{t}{2(1+\upsilon_{ur})}\left(\frac{\sigma_3^{'}}{\sigma_1^{'}}\right)^m E_{ur}^{ref} = \frac{t}{2(1+\upsilon_{ur})}(K_0)^m E_{ur}^{ref} \tag{2.29}$$

If $K_0 = 0.5,\ \upsilon_{ur} = 0.2$:

$$G_0^{ref} = 0.42t \times 0.5^m \times E_{ur}^{ref} \tag{2.30}$$

A flow chart illustrating the procedure to obtain G_0^{ref} when m, K_0, c_u and E_{50}/c_u are known, is shown in Figure 3.38.

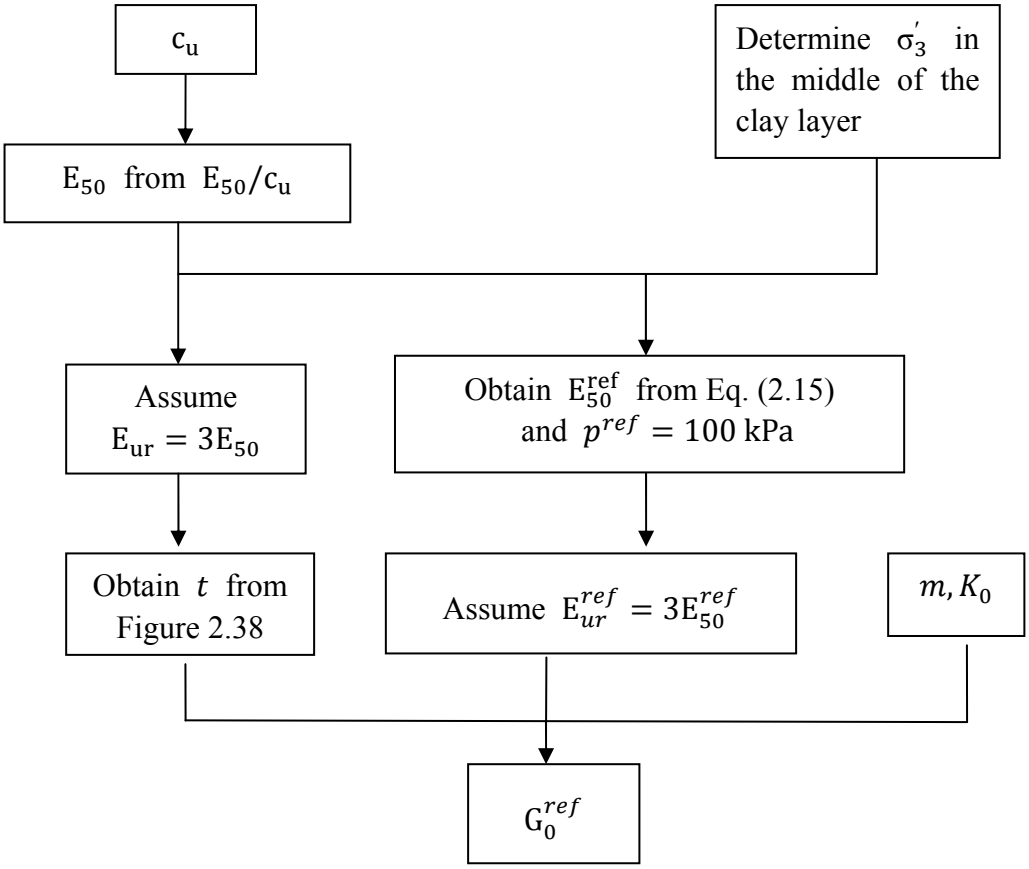

Figure 2.38 Procedure to Obtain G_0^{ref}

For example, for very soft clay, the PLAXIS recommendation is $m = 1,\ t = 9$. Substituting in Eq. (2.30) gives :

$$G_0^{ref} = 1.89E_{ur}^{ref} \tag{2.31}$$

For stiff clay and sand, $m = 0.8,\ t = 4$:

$$G_0^{ref} = 0.96E_{ur}^{ref} \tag{2.32}$$

Chapter 3

CASE STUDIES

3.1 Introduction

In this chapter, seven cases are presented to verify the HSS model in predicting excavation behavior. All the cases are for undrained behavior of clay. The HSS model in PLAXIS, which has been introduced in Chapter 2 is used for modeling the soft clay, stiff clay and sand layers. Some comparisons are also carried out with the HS model and the conventional Mohr-Coulomb model.

3.2 Parameters of HSS model

3.2.1 Undrained Traxial Test Stress-Strain

The Mohr-Coulomb (MC), HS, HSS stress-strain models can be compared in the following simple hypothetical triaxial case for undrained soil behavior, in which the initial stress $\sigma'_v = 100$ kPa. MC-A (method A) and MC-B (method B) are two different methods coined by Dr. Andrew Pickles as shown in Table 3.1 for modeling undrained soil behavior in PLAXIS. Wong (2003, 2004) further explained these two methods and pointed out that MC-A can overestimate the shear strength and produce wrong results. All the parameters for the models are shown in Table 3.2. The characteristics of small strain behavior are illustrated in the strain-stress curve of HSS in Figure 3.1. It demonstrates HSS model can model the nonlinear undrained behavior of clays. The HSS model predicts a lower failure deviator stress than the HS model because of the different failure criterion assumed.

Table 3.1 Parameters for MC-A and MC-B

Model	Material type	υ	φ (°)	c (kPa)	E_u (kPa)	E' (kPa)
Mohr-Coulomb-A (MC-A)	Undrained	0.35	input	0	–	input
Mohr-Coulomb-B (MC-B)	Undrained	0.35	0	c_u	input	–

Table 3.2 Parameters for Hypothetic Triaxial Case

model	φ (°)	$\frac{c_u}{\sigma_v'}$	c (kPa)	$K_0 = 1 - \sin\varphi'$	σ_3' (kPa)	E_{50} (kPa)	E_{50}^{ref} (kPa)	E_{oed}^{ref} (kPa)	E_{ur}^{ref} (kPa)	υ	m	R_f	G_0^{ref} (kPa)
MC-A	30	–	0	0.5	100	5000	–	–	–	0.35	–	–	–
MC-B-0.2	0	0.2	40	1	100	5500	–	–	–	0.35	–	–	–
MC-B-0.3	0	0.3	60	1	100	5500	–	–	–	0.35	–	–	–
HS	30	–	0	0.5	100	5000	5000	5000	15000	0.2	1	0.9	–
HS-Small	30	–	0	0.5	100	5000	5000	5000	15000	0.2	1	0.9	20000

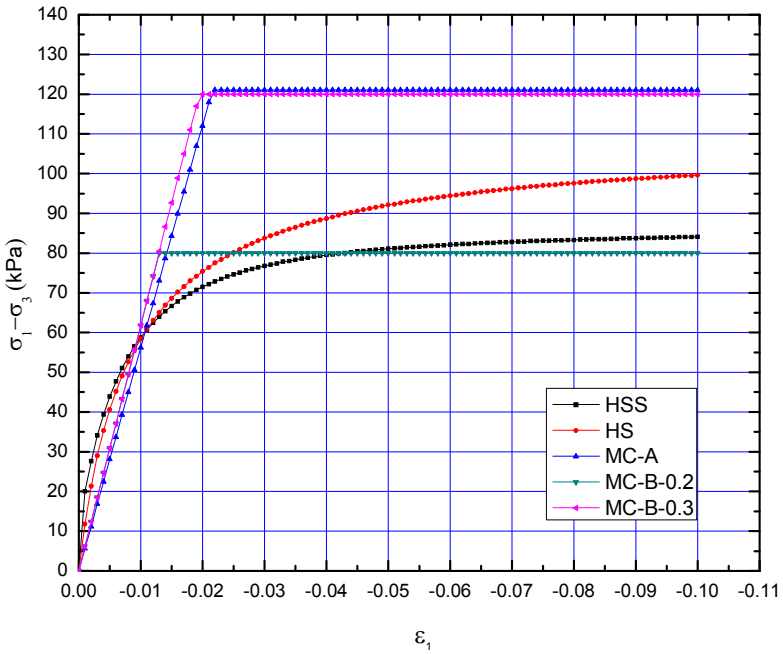

Figure 3.1 Comparison of Stress-Strain Curves for CU Triaxial Test

3.2.2 E_{50} for clay

For some of the case studies, stiff clay layers were present at the sites. Stroud (1974) suggested that c_u is about 4 to 6 N_{SPT} in kPa. In this study, c_u equals to $5N_{SPT}$ is adopted for the stiffer clays. For some cases which lack N_{SPT} values, the relationship between c_u and overburden stress σ_v' is used.

$$c_u = 5N_{SPT} \tag{3.1}$$

$$\frac{c_u}{\sigma_v'} = 0.2\sim0.35 \tag{3.2}$$

Duncan and Buchigani (1976) proposed relationships between c_u and E_u for predicting elastic stiffness of clay and silt at 50% of the failure stress (E_{50}), which is commonly used for MC model. For the HS-Small model used in this project, various correlations of E_{50}/c_u were used by taking $E_{50} = nc_u$, for $n = 100$, $n = 150$, $n = 200$ and so on, to examine the influence of the E_{50}/c_u ratio.

3.2.3 φ for Clay

For the effective friction angle used in HS and HSS models, Wroth and Houlsby (1985) suggested Eq. (3.3) for normally consolidated clay.

$$\left(\frac{s_{utc}}{\sigma'_{vo}}\right) = 0.5743\frac{3\sin\varphi}{3-\sin\varphi} \tag{3.3}$$

where σ'_{vo} is the vertical effective stress, s_{utc} is the undrained shear strength and φ is the effective friction angle in triaxial compression at the critical state.

3.2.4 E_{50} for Sand

Some of the sites contained sand deposits. Bowles (1988) listed a chart (Figure 3.2) for estimating E_S (in unit of kPa) for sand. The linear relationship between E_S and $(\mathrm{N_{SPT}} + 15)$ is adopted in the analysis herein.

For silt clay and loose sand,

$$\mathrm{E_{50}} = 320(\mathrm{N_{SPT}} + 15) \tag{3.4}$$

For dense and very dense sand

$$\mathrm{E_{50}} = 600(\mathrm{N_{SPT}} + 15) \tag{3.5}$$

E_s in kPa for SPT and units of q_c for CPT; divide kPa by 50 to obtain ksf. The N values should be estimated as N_{55} and not N_{70}. F

Soil	SPT	CPT
Sand (normally consolidated)	$E_s = 500(N + 15)$ $= 7000\sqrt{N}$ $= 6000N$ — — — ‡E_s = (15 000 to 22 000) · ln N	$E_s = (2 \text{ to } 4)q_u$ $= 8000\sqrt{q_c}$ — — — $E_s = 1.2(3D_r^2 + 2)q_c$ *$E_s = (1 + D_r^2)q_c$
Sand (saturated)	$E_s = 250(N + 15)$	$E_s = Fq_c$ $e = 1.0 \quad F = 3.5$ $e = 0.6 \quad F = 7.0$
Sands, all (norm. consol.)	¶E_s = (2600 to 2900)N	
Sand (overconsolidated)	†$E_s = 40\,000 + 1050N$ $E_{s(\mathrm{OCR})} \approx E_{s,\mathrm{nc}}\sqrt{\mathrm{OCR}}$	$E_s = (6 \text{ to } 30)q_c$
Gravelly sand	$E_s = 1200(N + 6)$ $= 600(N + 6) \quad N \le 15$ $= 600(N + 6) + 2000 \quad N > 15$	
Clayey sand	$E_s = 320(N + 15)$	$E_s = (3 \text{ to } 6)q_c$
Silts, sandy silt, or clayey silt	$E_s = 300(N + 6)$	$E_s = (1 \text{ to } 2)q_c$
	If $q_c < 2500$ kPa use $\quad$ §$E_s' = 2.5q_c$ $2500 < q_c < 5000$ use $\quad E_s' = 4q_c + 5000$ where E_s' = constrained modulus = $\dfrac{E_s(1-\mu)}{(1+\mu)(1-2\mu)} = \dfrac{1}{m_v}$	
Soft clay or clayey silt		$E_s = (3 \text{ to } 8)q_c$

Figure 3.2 Equations for stress-strain modulus E_S by several test methods (Bowles, 1988)

3.2.5 φ for Sand

Peck, Hanson and Thornburn (1974) recommended the relationship between SPT N value and φ for cohesionless soils as shown in Table 3.3.

Table 3.3 N versus φ Relationships

N Value (blows/ft or 305 mm)	Relative Density	Approximate φ (degrees)
0 ~ 4	Very loose	<28
4~10	Loose	28~30
10~30	Medium	30~36
30~50	Dense	36~41
>50	Very dense	>41

As shown in chapter 2, E_{50}^{ref} and G_0^{ref} can be derived from formula recommended in the PLAXIS manual and the default values are taken. In this chapter, coefficients of permeability adopted are $k = 1 \times 10^{-4}$ m/sec and $k = 1 \times 10^{-8}$ m/sec for drained and undrained material type, respectively. For simply, $\gamma_{0.7}$ is taken as 2×10^{-4} for all soils in the analyses as the range of $\gamma_{0.7}$ for clay and sand is about $1 \sim 5 \times 10^{-4}$ (Fig 2.36). Another reason is that the results are not significantly influenced by the $\gamma_{0.7}$ values.

3.3 Case Study

This section presents the results of the seven case studies. As mentioned in Section 3.2.2, various ratios of E_{50}/c_u were considered for the soft clays.

3.3.1 Project: Syed Alwi

A cross-section of the excavation support system and the soil profile are shown in Figure 3.3. A 20 m diaphragm wall braced at two levels formed the framework of the excavation support system. The original ground water level was about 1.0 m below ground surface. The strut spacing is 4.5 m. The HSS soil parameters adopted in the analysis and structural properties of the wall and struts are summarized in Table 3.4 and Table 3.5, respectively. The maximum predicted wall deflections using HSS($E_{50} = 150c_u$), HS($E_{50} = 150c_u$), and HSS($E_{50} = 100c_u$) for the soft clay are 45, 50 and 57 mm, respectively. The maximum measured wall deflection was 49 mm. For the same $E_{50}/c_u = 150$, the HSS model results in slightly smaller wall deflections than the HS model.

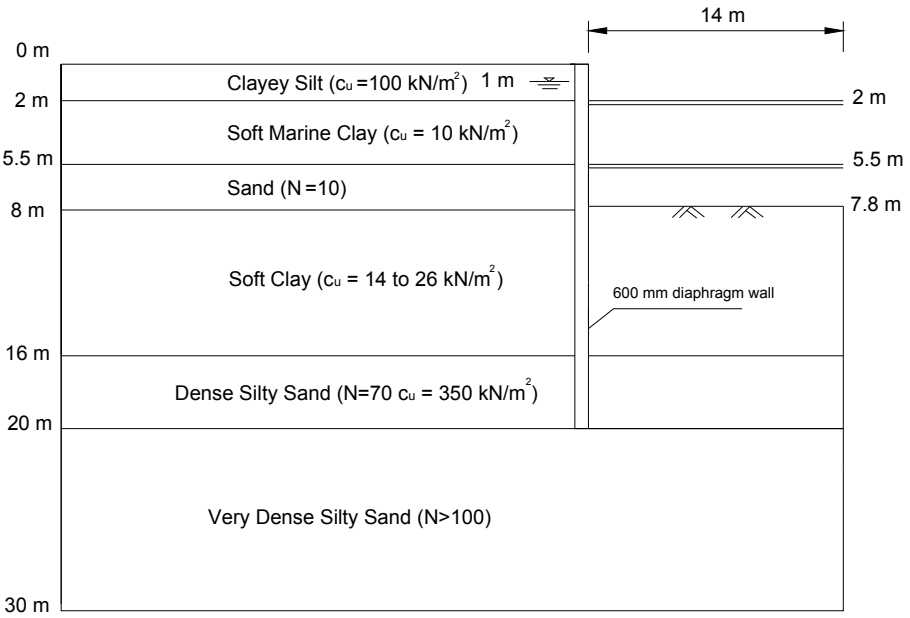

Figure 3.3 Cross-section of Excavation at Syed ALwi Project (Lim et al., 2003)

Table 3.4 Soil Properties at Syed Alwi Project (for clay, $E_{50} = 150c_u$)

Soil type	model	γ (kN /m³)	N	c_u (kPa)	E_{50} (kPa)	E_{50}^{ref} (kPa)	E_{oed}^{ref} (kPa)	E_{ur}^{ref} (kPa)	m	G_0^{ref} (kPa)	$\gamma_{0.7}$	φ (°)	k (m/ sec)
Silty clay (0-2 m)	HSS	20	–	100	15000	60000	60000	180000	1	220000	0.0002	25	1e-8
Soft marine clay (2-5.5 m)	HSS	15	–	10	1500	8000	8000	24000	1	30000	0.0002	25	1e-8
Sand (5.5-8 m)	HSS	20	10	–	15000	60000	60000	18000	0.8	200000	0.0002	30	1e-4
Soft clay (8-16 m)	HSS	17	–	20	3000	5000	5000	15000	1	30000	0.0002	22	1e-8
Dense silty sand (16-20 m)	HSS	19	70	350	51000	200000	200000	600000	1	670000	0.0002	42	1e-8
Very dense silty sand (20-30 m)	HSS	21	150	750	99000	400000	400000	1200000	1	900000	0.0002	44	1e-8

Table 3.5 Structural Properties at Syed Alwi Project

Structural members	E (kN/m²)	A (m²/m)	Preload (kN/m)
Strut (at -2 m)	2.07×10^8	0.004125	25
Strut (at -5.5 m)	2.07×10^8	0.004125	100
Diaphragm wall 600 mm	2.8×10^7	–	–

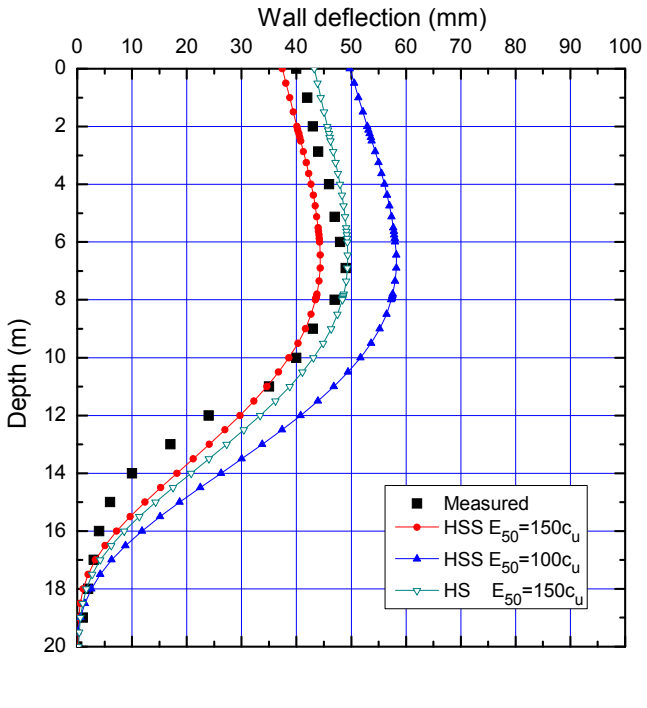

Figure 3.4 Wall Deflection at Syed Alwi Project

3.3.2 Rochor Complex

Figure 3.5 shows a typical cross-section of this project. The excavation support system consisted of a 24 m long sheet pile braced at three levels. The original ground water table was about 1.5 m below ground surface. The HSS soil parameters and structural properties adopted in the analysis are shown in Table 3.6 and Table 3.7, respectively. The computed and measured wall deflection profiles are shown in Figure 3.6. The computed ground settlements for different soil models are shown in Figure 3.7. The results show the shape of the wall deflection is matched well when taking $E_{50} = 100c_u$ for the HSS model in the analysis. The shape of wall deflections and soil settlements predicted by HSS with different ratio of E_{50}/c_u are very similar. The soil settlement profile modeled by MC (method B) with $E_{50} = 200c_u$ is significantly different from HS and HSS even when the magnitudes of wall deflection are similar. For the same E_{50}/c_u ratio, the HSS

model results in slightly smaller wall deflections and settlements than the HS model.

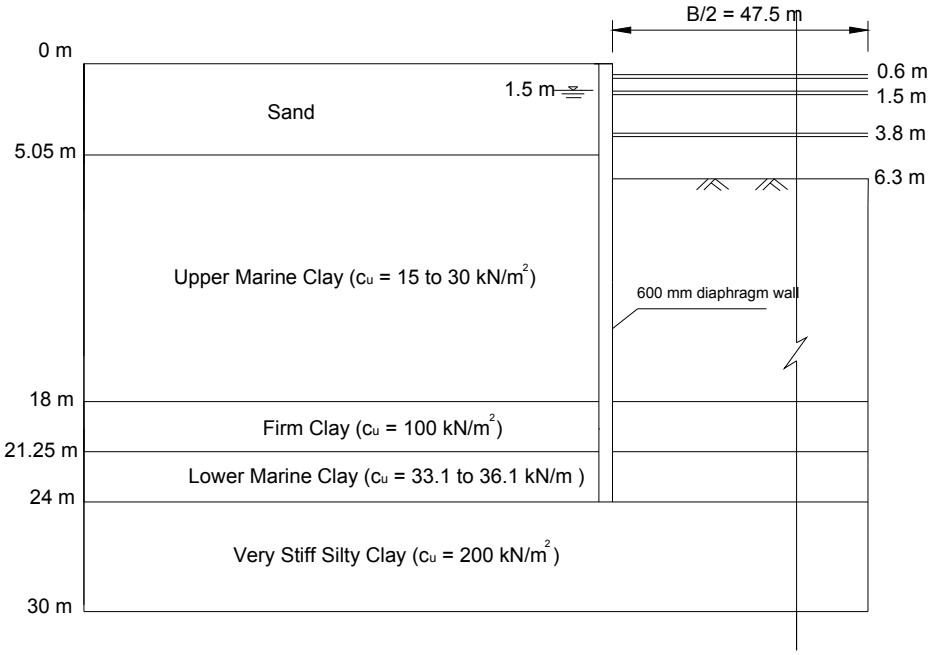

Figure 3.5 Cross-section of Excavation at Rochor Complex Project (Lim et al., 2003)

Table 3.6 Soil Properties at Rochor Complex Project (for clay, $E_{50} = 100c_u$)

Soil type	model	γ (kN /m^3)	N	c_u (kPa)	E_{50} (kPa)	E_{50}^{ref} (kPa)	E_{oed}^{ref} (kPa)	E_{ur}^{ref} (kPa)	m	G_0^{ref} (kPa)	$\gamma_{0.7}$	φ (°)	k (m/ sec)
Sand (0-5.05 m)	HSS	20	25	–	10000	40000	40000	120000	0.8	15000	0.0002	30	1e-4
Upper marine clay (5.05-18.5 m)	HSS	16	–	22.5	2250	3500	3500	10500	1	20000	0.0002	26	1e-8
Firm clay (18.5-21.25 m)	HSS	17	–	100	27000	40000	40000	120000	0.8	150000	0.0002	38	1e-8
Lower marine clay (21.25-24 m)	HSS	16	–	34	3400	4000	4000	12000	1	20000	0.0002	27	1e-8
Very stiff silty sand (24-40 m)	HSS	18	–	200	150000	150000	150000	450000	0.8	560000	0.0002	38	1e-8

Table 3.7 Structural Properties at Rochor Complex Project

Structural members	E (kN/m^2)	A (m^2/m)	I (m^4/m)	Preload (kN/m)
Strut (at -0.6 m)	2.07×10^8	0.004	–	28
Strut (at -1.5 m)	2.07×10^8	0.004	–	104.3
Strut (at -3.8m)	2.07×10^8	0.008	–	175.1
Diaphragm wall 600 mm	2.07×10^7	0.0186	0.000228	–

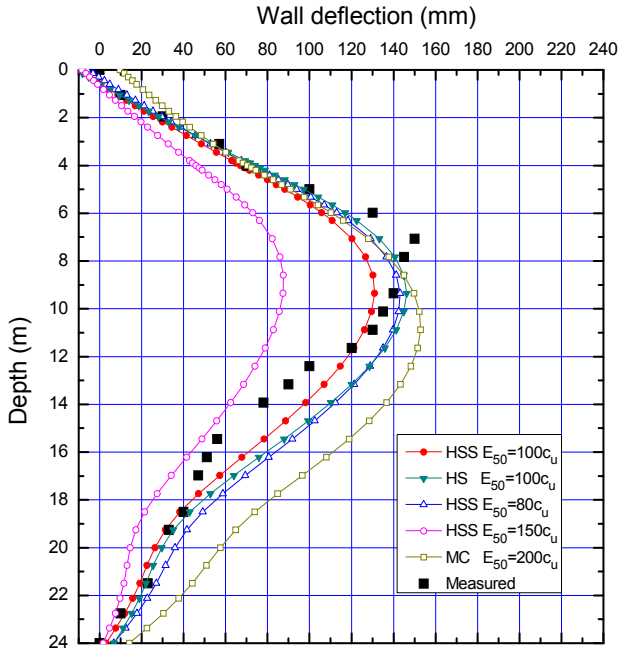

Figure 3.6 Wall Deflection at Rochor Complex Project

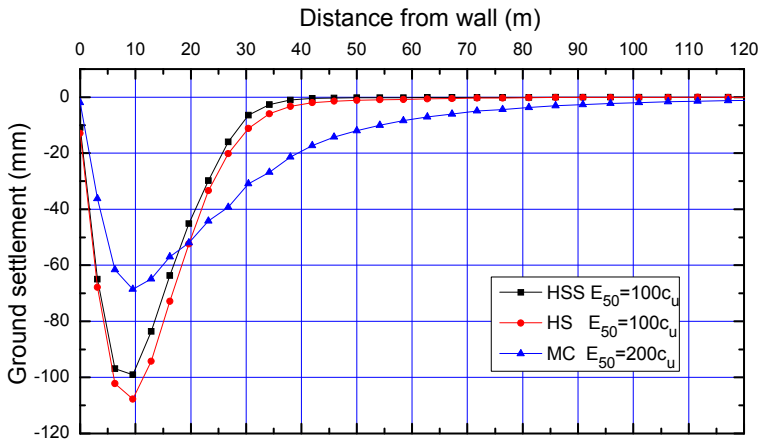

Figure 3.7 Surface settlement at Rochor Complex Project

3.3.3 Lavender MRT Station

A cross-section of the excavation is shown in Figure 3.8. The support system consisted of a 1000 mm thick diaphragm wall and six levels of struts. The ground water table was about 1.5 m below ground surface. The HSS soil parameters and structural properties are listed in Table 3.8 and Table 3.9, respectively. The computed and measured wall deflections are presented in Figure 3.9, which show good prediction except for the top part of the wall. A smaller displacement is predicted at the toe of the wall by the HSS model compared with the HS model. The predicted soil settlements by the HSS, HS and MC models are shown in Figure 3.10.

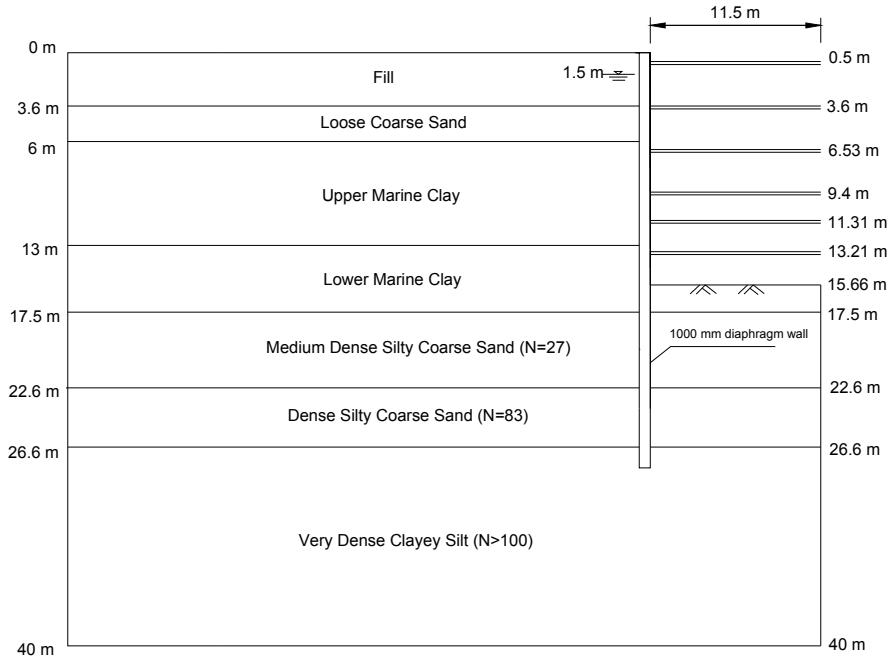

Figure 3.8 Cross-Section of Excavation at Lavender MRT Station (Lim et al., 2003)

Table 3.8 Soil Properties at Lavender MRT Station (for clay, $E_{50} = 100c_u$)

Soil type	model	γ (kN/m³)	N	c_u (kPa)	E_{50} (kPa)	E_{50}^{ref} (kPa)	E_{oed}^{ref} (kPa)	E_{ur}^{ref} (kPa)	m	G_0^{ref} (kPa)	$\gamma_{0.7}$	φ (°)	k (m/sec)
Fill (0-3.6 m)	HSS	18	17	–	8000	24000	24000	72000	0.8	80000	0.0002	33	1e-4
Coarse Sand (3.6-6 m)	HSS	20	25	–	10000	80000	80000	240000	0.8	300000	0.0002	38	1e-4
Upper marine clay (6-13 m)	HSS	16	–	23	2500	5200	5200	156000	1	26500	0.0002	25	1e-8
Lower Marine Clay (13-17.5 m)	HSS	16	–	35	3500	5400	5400	16000	1	25000	0.0002	26	1e-8
Dense sand (17.5-30 m)	HSS	20	70	–	40000	35000	35000	105000	1	130000	0.0002	40	1e-8

Table 3.9 Structural Properties at Lavender MRT Station

Structural members	E (kN/m²)	A (m²/m)	I (m⁴/m)	Preload (kN/m)
Strut (at -1 m)	2.07×10^8	0.0040	–	190
Strut (at -4.5 m)	2.07×10^8	0.0058	–	390
Strut (at -7.0m)	2.07×10^8	0.0073	–	327
Strut (at -10.0m)	2.07×10^8	0.0058	–	260
Strut (at -12.0m)	2.07×10^8	0.0058	–	233
Strut (at -14.0 m)	2.07×10^8	0.0058	–	220
Diaphragm wall 1000 mm	2.80×10^7	1.0000	0.083	–

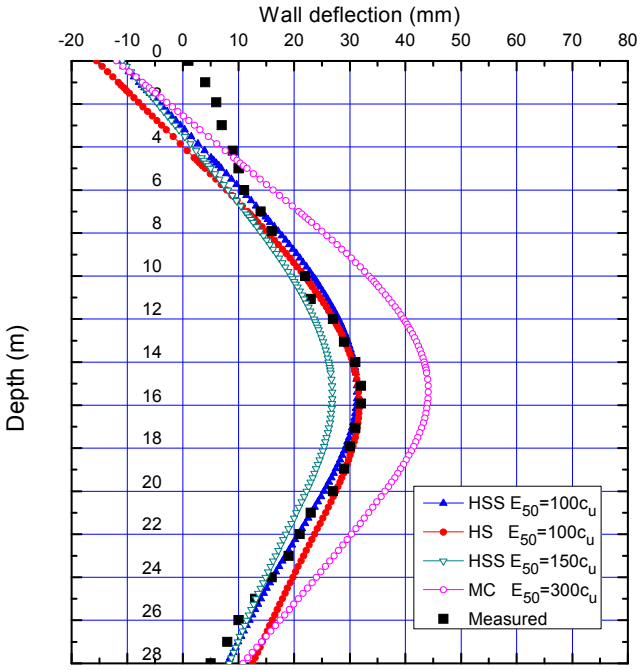

Figure 3.9 Wall Deflection at Lavender MRT Station

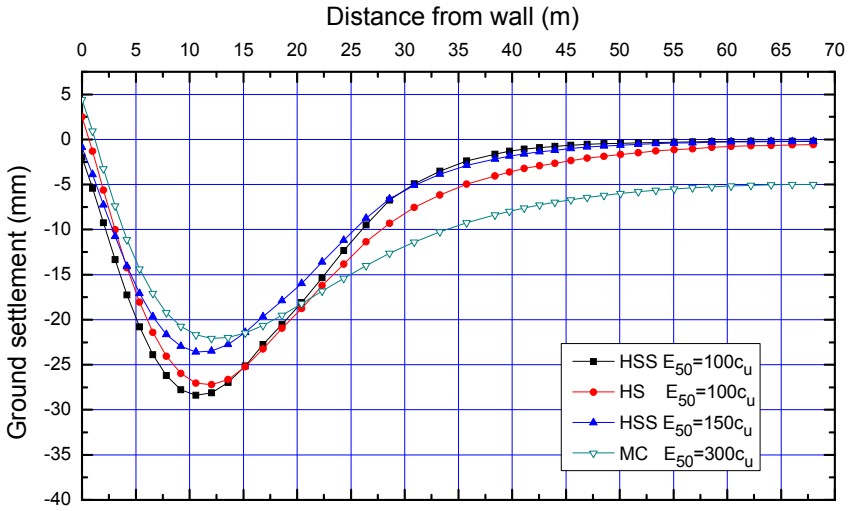

Figure 3.10 Ground Settlement at Lavender MRT Station

3.3.4 Farrer Park–Kandang Kerbau

The cross-section of the excavation is shown in Figure 3.11. The 800 mm thick diaphragm wall was constructed to a depth of 28 m. The excavation width was 21 m. The original ground water table was about 1 m below ground surface. The HSS soil parameters and structural properties are shown in Table 3.10 and Table 3.11, respectively. The computed wall deflection and ground settlement modeled by HSS HS and MC are presented in Figure 3.12 and Figure 3.13, respectively. They show the predicted result agrees with the maximum measured wall deflection when using HSS model with $E_{50} = 150c_u$. The plot in Figure 3.12 shows that modeling the Old Alluvium (OA) with the HSS model results in slightly smaller wall deflections at the wall toe compared with modeling the OA with the Mohr Coulomb model with $E_{50} = E_u$.

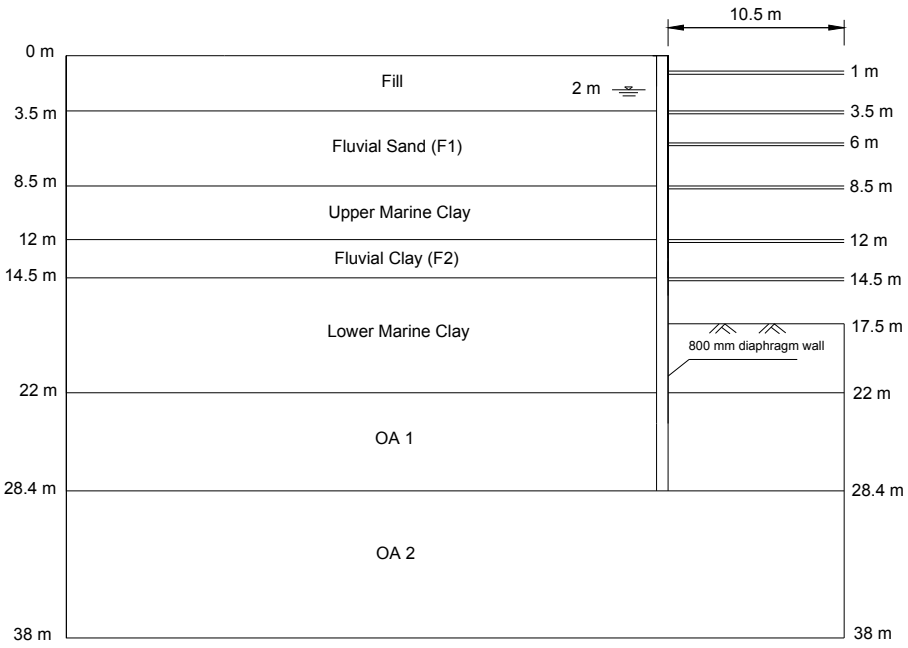

Figure 3.11 Cross-Section of Excavation at Farrer Park–Kandang Kerbau (CH 31+895) (Halim, 2008)

Table 3.10 Soil Properties at Farrer Park–Kandang Kerbau (CH 31+895)

$(E_{50} = 150c_u)$

Soil type	model	γ (kN /m^3)	N	c_u (kPa)	$\frac{c_u}{\sigma_v'}$	E_{50} (kPa)	E_{50}^{ref} (kPa)	E_{oed}^{ref} (kPa)	E_{ur}^{ref} (kPa)	m	G_0^{ref} (kPa)	$\gamma_{0.7}$	φ (°)	k (m/ sec)
Fill (0-3.5 m)	HSS	19	6	–	–	5250	33000	33000	100000	0.8	130000	0.0002	30	1e-4
Fluvial sand (3.5-8.5 m)	HSS	19	15	–	–	7500	23000	23000	69000	0.8	67000	0.0002	35	1e-5
Upper marine clay (8.5-12 m)	HSS	16	–	25	0.26	3750	6300	6300	19000	1	39000	0.0002	23	1e-8
Fluvial clay (12-14.5 m)	HSS	17	–	30	–	4500	6400	6400	19000	1	29000	0.0002	23	1e-8
Lower marine clay (14.5-22 m)	HSS	16	–	44	0.3	6600	7950	7950	23800	1	30000	0.0002	26	1e-8
OA 1 (22-28.4 m)	HSS	20	30	150	–	90000	107000	107000	320000	0.8	380000	0.0002	40	1e-8
OA 1 (28.4-38 m)	HSS	20	100	500	–	300000	270000	270000	900000	0.8	820000	0.0002	45	1e-8

Table 3.11 Structural Properties at Farrer Park–Kandang Kerbau(CH 31+895)

Structural members	E (kN/m^2)	A (m^2/m)	Preload (kN/m)
Strut (at -1 m)	2.07×10^8	0.0019	No information
Strut (at -3.5 m)	2.07×10^8	0.00228	No information
Strut (at -6 m)	2.07×10^8	0.00258	No information
Strut (at -8.5 m)	2.07×10^8	0.00396	No information
Strut (at -12 m)	2.07×10^8	0.00396	No information
Strut (at -14.5 m)	2.07×10^8	0.002586	No information
Diaphragm wall 800 mm	2.8×10^7	–	–

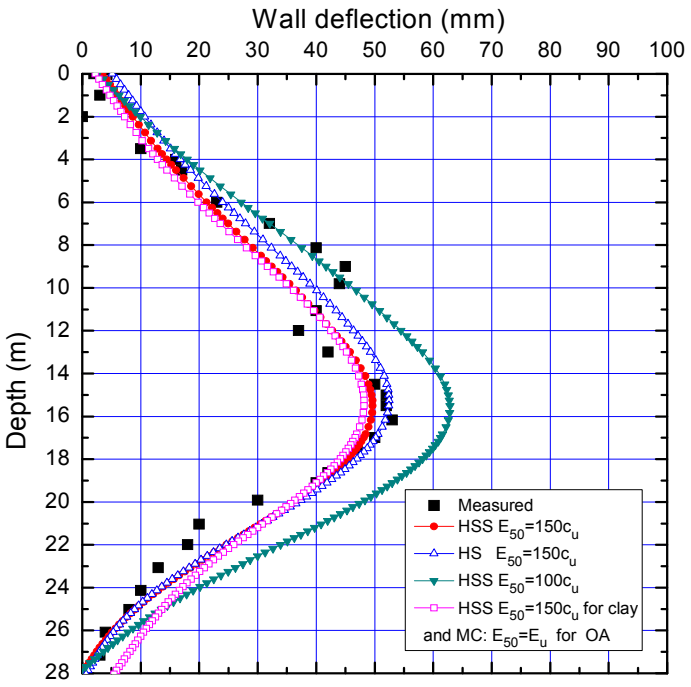

Figure 3.12 Wall Deflection of Excavation at Farrer Park–Kandang Kerbau (CH 31+895)

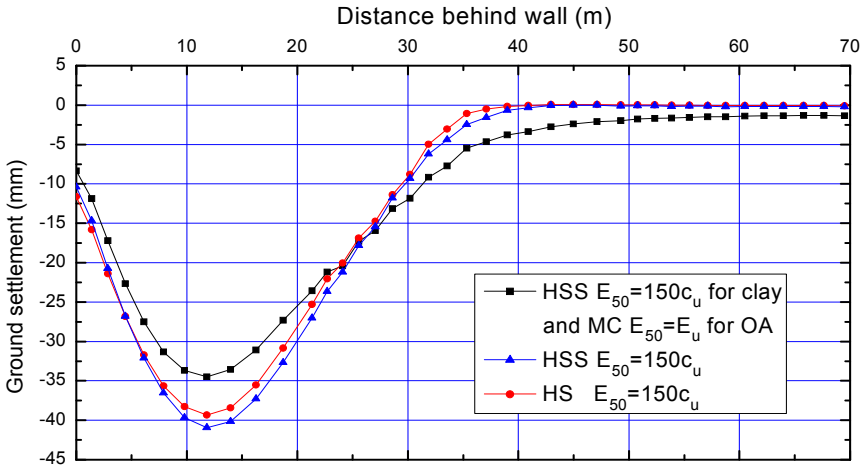

Figure 3.13 Ground settlement of Excavation at Farrer Park–Kandang Kerbau (CH 31+895)

3.3.5 Project Kotoku

This project constructed in Tokyo was reported by Miyoshi (1977) for a subway. A typical cross-section is shown in Figure 3.14. The 400 mm thick diaphragm wall combined with H piles was braced by five strut levels. The ground water level was about 2 m below ground surface. The HSS soil parameters and structural properties are summarized in Table 3.12 and Table 3.13, respectively. The computed and measured wall deflections are shown in Figure 3.14. The ground surface settlements predicted by the HS and HSS model are shown in Figure 3.15. The plots show that the magnitude of G_0^{ref} for the HSS model affects the wall deflection more significantly than the soil settlement when G_0^{ref} increases from 30000 kPa to 40000 kPa. The definition of G_0^{ref} which controls the small strain behavior has been discussed in Chapter 2.

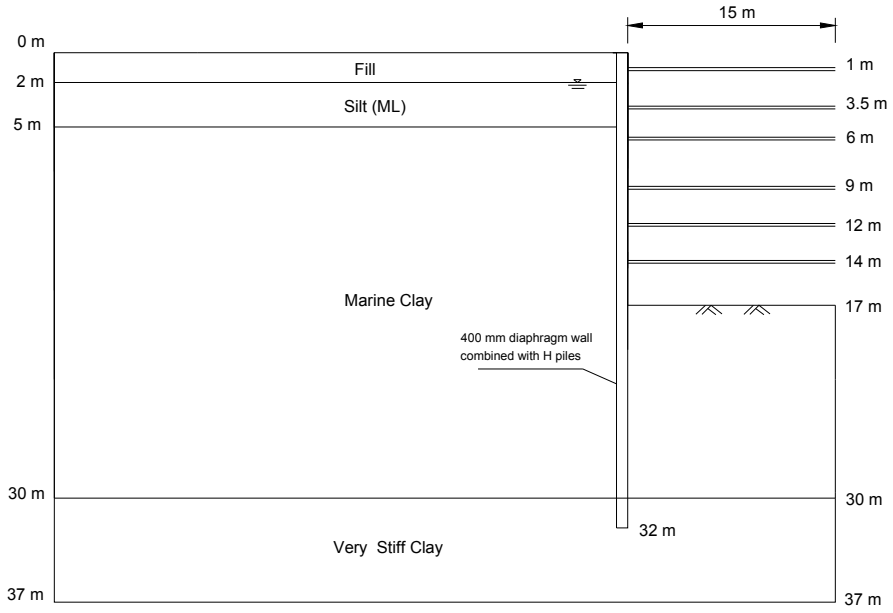

Figure 3.14 Cross-Section of Excavation at Kotoku Project (Halim, 2008)

Table 3.12 Soil Properties at Kotoku Project (for clay, $\frac{c_u}{\sigma_v'} = 0.34, E_{50} = 100c_u$)

Soil type	model	γ (kN/m³)	N	c_u (kPa)	E_{50} (kPa)	E_{50}^{ref} (kPa)	E_{oed}^{ref} (kPa)	E_{ur}^{ref} (kPa)	m	G_0^{ref} (kPa)	$\gamma_{0.7}$	φ (°)	k (m/sec)
Fill (0-2 m)	HSS	19	15	–	7500	40000	40000	120000	0.8	150000	0.0002	30	1e-4
Silt (2-5 m)	HSS	16	–	12	1200	30000	30000	90000	1	30000	0.0002	28	1e-8
Marine clay (5-30 m)	HSS	16	–	45	4500	7500	7500	22500	1	30000 40000	0.0002	28	1e-8
Very stiff silty clay (30-37 m)	HSS	16	–	250	150000	150000	150000	450000	0.8	560000	0.0002	33	1e-8

Table 3.13 Structural Properties at Kotoku Project

Structural members	E (kN/m²)	A (m²/m)	Preload (kN/m)
Strut (at -1 m)	2.07×10^8	0.0028	No information
Strut (at -3.5 m)	2.07×10^8	0.0028	No information
Strut (at -6 m)	2.07×10^8	0.0028	No information
Strut (at -9 m)	2.07×10^8	0.0074	No information
Strut (at -11.5 m)	2.07×10^8	0.0074	No information
Strut (at -14 m)	2.07×10^8	0.0074	No information
Diaphragm wall 800 mm	2.8×10^7	–	–

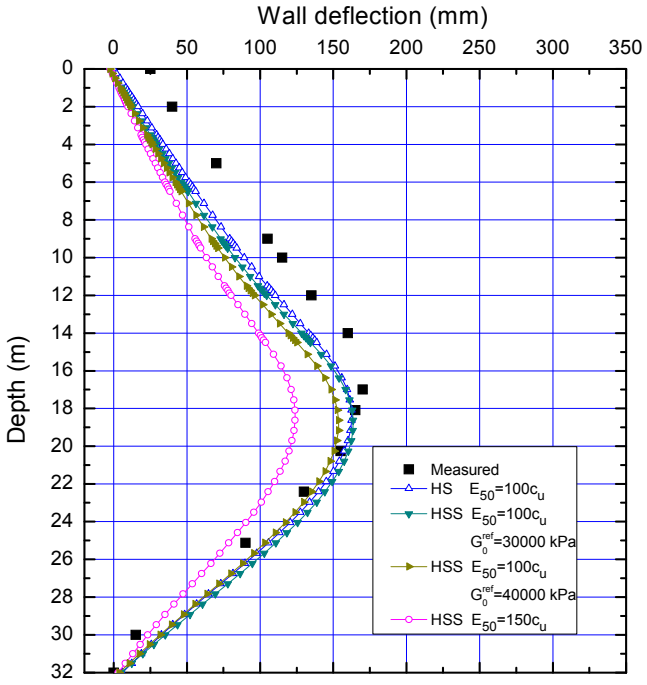

Figure 3.15 Wall Deflection at Kotoku Project

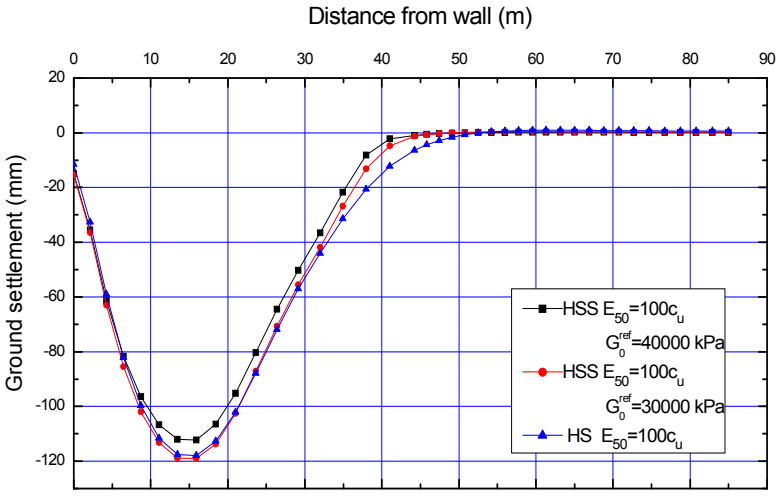

Figure 3.16 Ground Settlement at Kotoku Project

3.3.6 Formosa Project in Taipei

This case was reported by Ou et al. (1993) and Hsieh and Ou (1998). The cross-section is shown in Figure 3.17. The excavation is braced by six levels of struts with no preloading included. The HSS soil parameters adopted in the analysis are shown in Table 3.14. The structural information is presented in Table 3.15. The measured and computed results of wall deflection and soil settlement are shown in Figure 3.18 and Figure 3.19, respectively. It shows the HS and HSS model can match well with the measured wall deformation and soil settlement when taking suitable ratio of E_{50}/c_u. The plots show that shape of the wall deflection is similar but not the soil settlement when using the MC model compared with the HS and HSS models. For this case, the HSS model does not result in significantly different wall deflection compared with the HS model as the G_0^{ref} is only slightly larger than E_{ur}^{ref} for the silty clay.

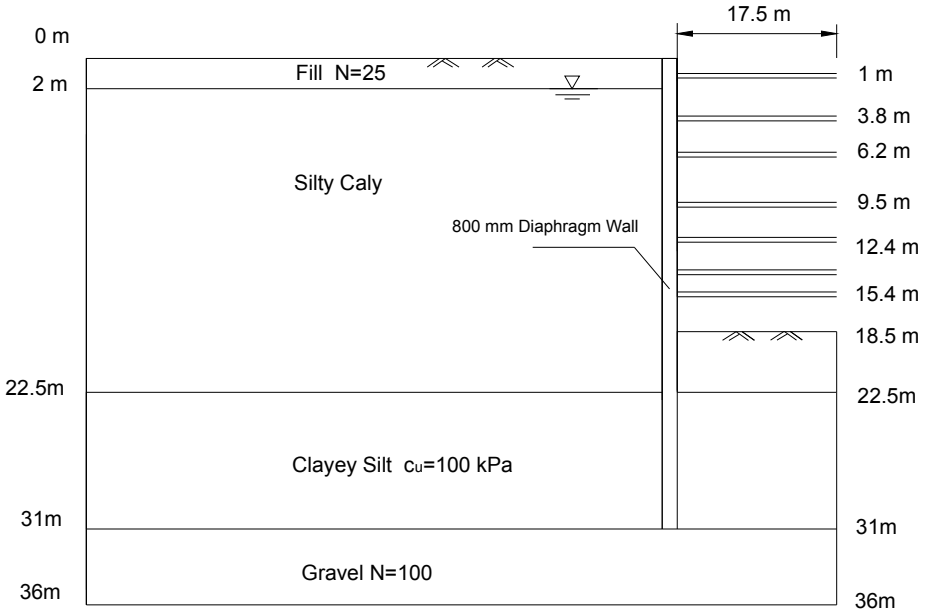

Figure 3.17 Cross-Section of Excavation at Formosa Project (Halim, 2008)

Table 3.14 Soil Properties at Formosa Project (for clay, $E_{50} = 200c_u$)

Soil type	model	γ	N	c_u	E_{50}	E_{50}^{ref}	E_{oed}^{ref}	E_{ur}^{ref}	m	G_0^{ref}	$\gamma_{0.7}$	φ	k
		(kN/m^3)		(kPa)	(kPa)	(kPa)	(kPa)	(kPa)		(kPa)		(°)	(m/sec)
Fill (0-2 m)	HSS	19	25	–	10000	80000	80000	240000	0.8	500000	0.0002	33	1e-4
Silty clay (2-22.5 m)	HSS	19	–	45	9000	20000	20000	60000	1	76000	0.0002	32	1e-8
Clayey silt (22.5-31 m)	HSS	19	–	100	20000	40000	40000	120000	1	130000	0.0002	40	1e-8
Gravel (31-36 m)	HSS	20	100	–	69000	60000	60000	180000	0.8	200000	0.0002	44	1e-4

Table 3.15 Structural Properties at Formosa Project

Structural members	E (kN/m^2)	A (m^2/m)	Preload (kN/m)
Strut (at -1 m)	2.07×10^8	0.0028	No information
Strut (at -3.8 m)	2.07×10^8	0.0028	No information
Strut (at -6.2 m)	2.07×10^8	0.0028	No information
Strut (at -9.5 m)	2.07×10^8	0.0028	No information
Strut (at -12.4 m)	2.07×10^8	0.0046	No information
Strut (at -15.4 m)	2.07×10^8	0.0046	No information
Diaphragm wall 800 mm	2.8×10^7	–	–

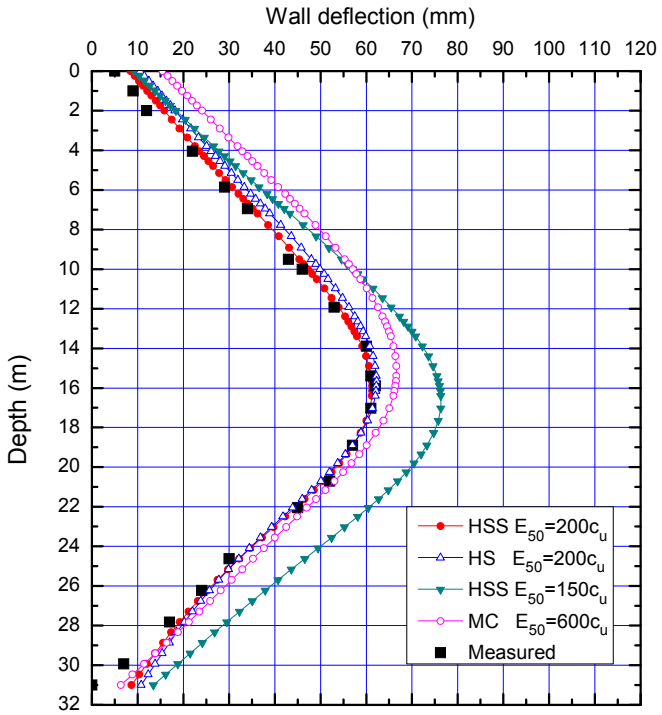

Figure 3.18 Wall Deflection at Formosa Project

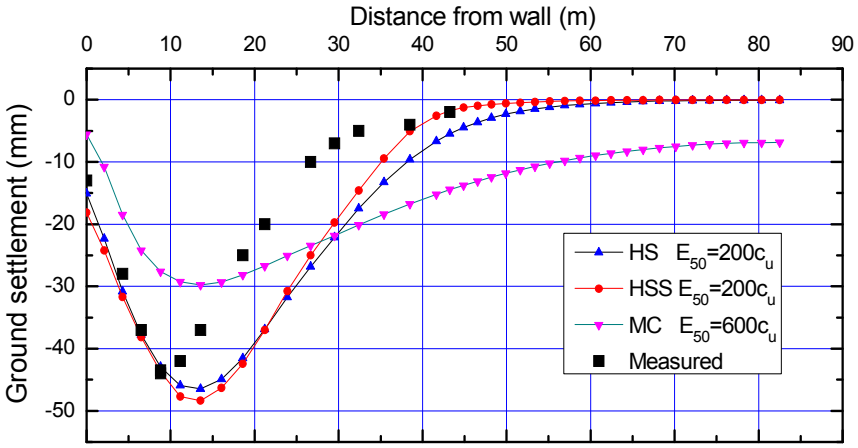

Figure 3.19 Soil Settlement at Formosa Project

3.3.7 TNEC Project

This study case was reported by Ou et al. (1998) in Taipei. It used the top-down construction method. The cross-section of the project is shown in Figure 3.20. The depth and width of excavation were 19.7 m and 43 m, respectively. The wall length was 35 m. The HSS soil parameters and structural properties adopted in the analysis are shown in Table 3.16 and Table 3.17, respectively. The computed and measured wall deflections and ground settlement are shown in Figure 3.21 and Figure 3.22, respectively. It illustrates the magnitude of measured maximum wall deflection and ground settlement match well with the computed results when using HSS model with E_{50}/c_u in the range of 100 to 150.

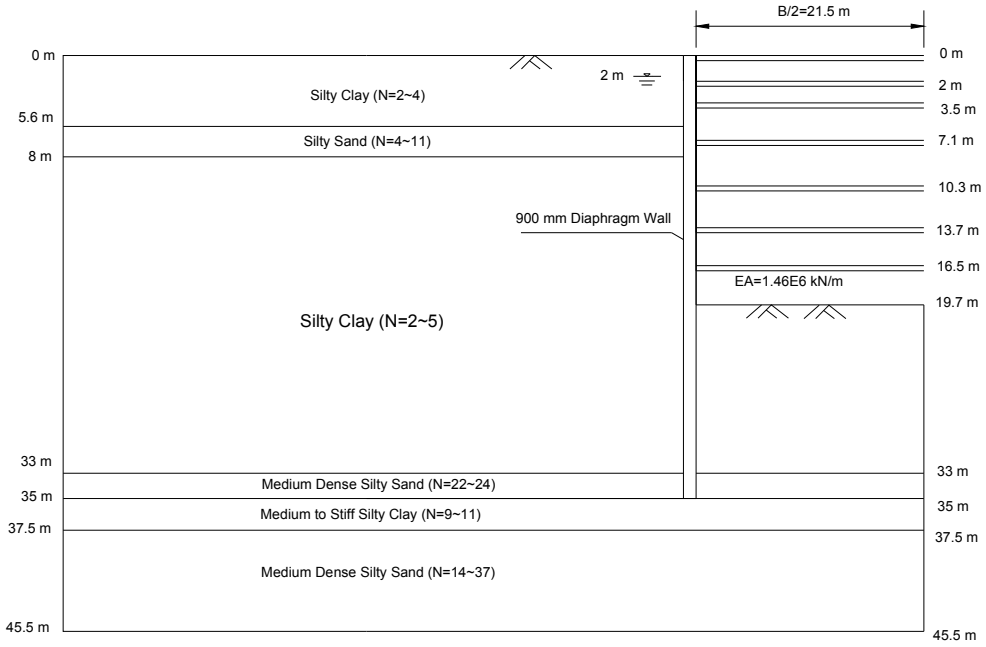

Figure 3.20 Cross-Section of Excavation at TNEC Project (Halim, 2008)

Table 3.16 Soil Properties of Excavation at TNEC Project(for clay, $E_{50} = 100c_u$)

Soil type	model	γ (kN/m³)	N	c_u (kPa)	E_{50} (kPa)	E_{50}^{ref} (kPa)	E_{oed}^{ref} (kPa)	E_{ur}^{ref} (kPa)	m	G_0^{ref} (kPa)	$\gamma_{0.7}$	φ (°)	k (m/sec)
Silty Clay (0-5.6 m)	HSS	19	–	20	2000	6600	6600	19800	1	25000	0.0002	33	1e-8
Silty Sand (5.6-8 m)	HSS	20	7	–	5500	15000	15000	45000	0.8	56000	0.0002	35	1e-8
Silty Clay (8-33 m)	HSS	19	–	66	6600	6600	6600	19800	1	29000	0.0002	30	1e-8
Medium Dense Silty Sand (33-35 m)	HSS	20	25	–	24000	30000	30000	90000	0.8	112500	0.0002	36	1e-8
Medium to Stiff Silty Clay (35-37.5 m)	HSS	19	–	150	15000	15000	15000	45000	1	33000	0.0002	32	1e-8
Medium to Dense Silty Sand (37.5-46 m)	HSS	20	32	–	47000	40000	40000	120000	0.8	130000	0.0002	38	1e-8

Table 3.17 Structural Properties of Excavation at TNEC Project

Structural members	E (kN/m²)	A (m²/m)	Preload (kN/m)
Strut (at 0 m)	2.8×10^8	0.6	–
Strut (at -2 m)	2.07×10^8	0.0015	98.1
Strut (at -3.5 m)	2.8×10^8	0.6	–
Strut (at -7.1 m)	2.8×10^8	0.6	–
Strut (at -10.3 m)	2.8×10^8	0.6	–
Strut (at -13.7 m)	2.8×10^8	0.6	–
Strut (at -16.5 m)	2.07×10^8	0.0073	392
Diaphragm wall 800 mm	2.8×10^7	–	–

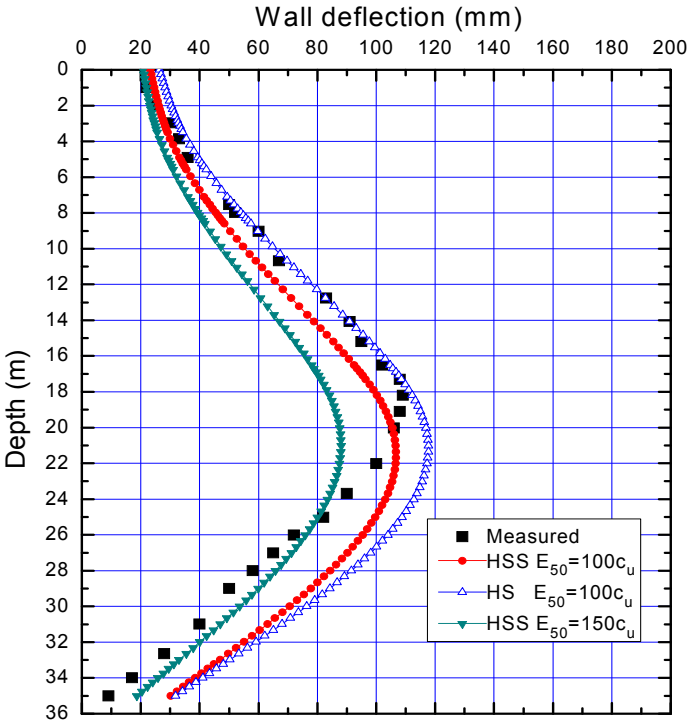

Figure 3.21 Wall Deflection of Excavation at TNEC Project

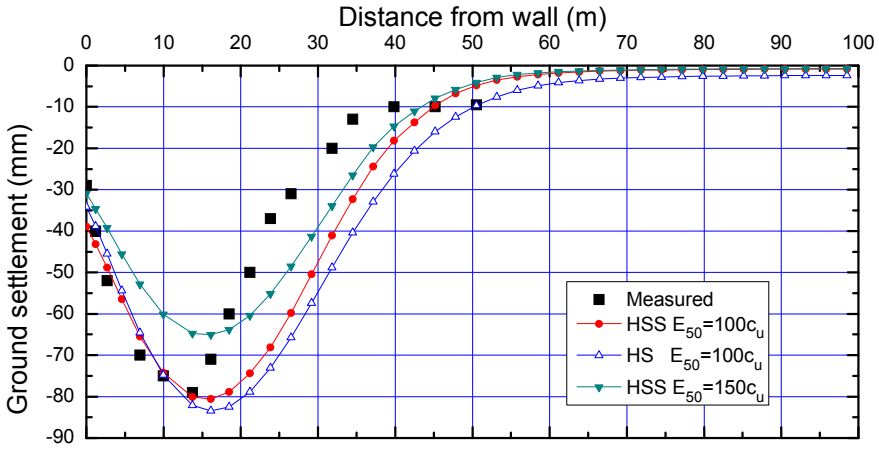

Figure 3.22 Ground Settlement of Excavation at TNEC Project

3.4 Comparison of HSS and HS

3.4.1 Introduction

Since some of the case studies show that there are small differences in wall deflections between using the HS model and HSS model, and at the same time, it is difficult to obtain the small strain parameters for different soils in sites when using HSS model, parametric studies have been conducted to study the relation of the two models, and to see if the HS model can be used in place of the HSS model to give reasonable predictions for excavation problems. The studies can also help users know when they should use small strain model and when the HS is enough.

3.4.2 Parametric Study

A series of parametric studies using the HSS model were carried out to investigate the influence of small strain behavior with different G_0 compared with the HS model. Figure 3.23 shows the geometry of the hypothetical case which is adopted, and is typical of a soil profile in coastal areas with stiff clay layer underlying the thick soft clay layer. The analyses consider a plane-strain excavation supported by a diaphragm wall with thickness of 0.9 m and length of 33 m. The construction sequence comprises the following steps: (1) the wall is installed and the soil is initially excavated to a depth of 2 m; (2) the strut is then installed at 1 m higher than excavation level; (3) subsequent excavation is continued with struts at 3 m vertical spacings until the final depth of 20 m is reached.

For simplicity, the water table is assumed to be at ground surface with hydrostatic pore pressure and the soil is subject to undrained shearing during excavation. This Section focuses on the influence of soil properties on small strain behavior and excavation deformation at different excavation stages.

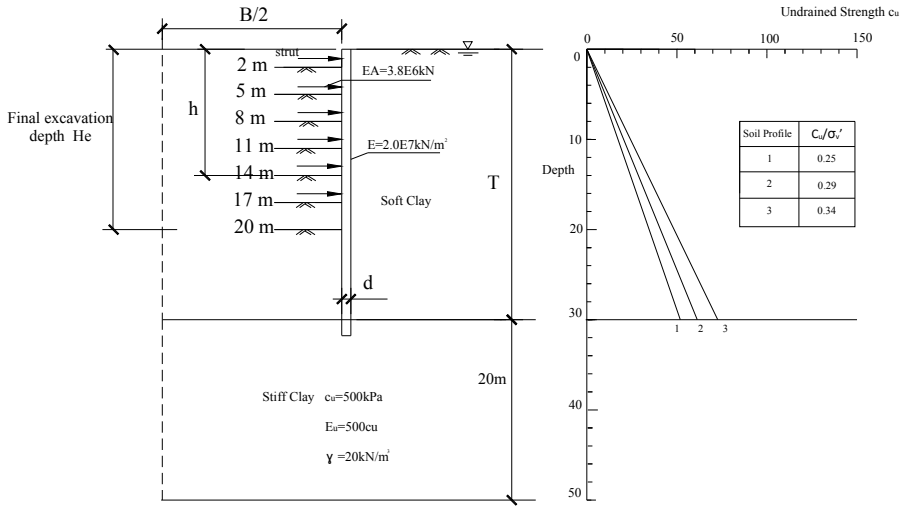

Figure 3.23 Excavation Geometry and Soil Properties

Undrained shear strength and stiffness modulus are the two basic parameters to model the stress-strain behavior of soil in FEM analysis of undrained excavation problems. PLAXIS permits users to model undrained behavior of soil with effective parameters. Two coefficients $\alpha = c_u/\sigma_v'$ and $\beta = E_{50}/c_u$ in undrained analysis are used to describe the HS and the HSS model, where c_u is the undrained shear strength, σ_v' is the vertical effective stress and E_{50} is the 50% secant stiffness in drained triaxial test. The effective friction angle φ is obtained from coefficient α through Eq. (3.3):

$$\frac{c_u}{\sigma_v'} = 0.5743 \frac{3 \sin \varphi}{3 - \sin \varphi} \tag{3.3}$$

The soil is assumed to be a normally consolidated soft clay. The PLAXIS default values are used to define the parameters of K_0^{nc}, υ_{ur} and E_{ur} with $K_0^{nc} = 1 - \sin \varphi$, $\upsilon_{ur} = 0.2$ and $E_{ur} = 3E_{50}$. Table 3.18 lists various values of α and β for eight groups of different cases. For each HS case which is represented by the subscript 0, four different HSS cases are considered and are represented by

subscript i with $i = 1, 2, 3$ or 4. Table 3.19 shows the variation of parameter G_0 for HSS cases in each group at the mid-depth in the soft clay layer. G_0 is deduced by the coefficients and Eq. (2.21) and Eq. (2.24):

$$G_0 = \frac{E_0}{2(1+\upsilon_{ur})} \tag{2.21}$$

$$E_0 = tE_{ur} \tag{2.24}$$

This results in

$$G_0 = \frac{3\alpha\beta t\gamma' h}{2(1+\upsilon_{ur})} \tag{3.6}$$

The reference value of E_{50}^{ref} and G_0^{ref} can be evaluated by stress dependent equations Eq. (2.15 ~ 2.17) at $p^{ref} = 100$ kPa.

There were many factors such as strain amplitude, confining stress, void ratio, plasticity index, etc affecting the G_0 of soft clay (Benz, 2007). Some relationships between G_0 and these factors were proposed to evaluate the G_0 by researchers (Hardin & Richard, 1963; Hardin & Black, 1968; Hardin & Drnevich, 1972 and Wroth, et al., 1979). Anderson & Woods (1976) suggested the dimensionless soil parameter I_R for many clays were in the range of 300 to 1800, where I_R is the ratio of G_0/c_u. Chew et al. (1997) reported I_R of about 700 for Singapore marine clay. Kung et al. (2008) indicated I_R for Sungshan Formation in Taipei was approximately 1000. Eq. (3.5) indicates the ratio of G_0/c_u equals to $1.25t\beta$ or $3k\beta$, which is shown in Table 3.19. Table 3.20 shows the value of k for the two kinds of clays according to the value of I_R.

Table 3.18 Basic Parameters for HS and HSS Model ($i = 1$~4)

Case	A		B		C		D		E		F		H		J	
	A_0	A_i	B_0	B_i	C_0	C_i	D_0	D_i	E_0	E_i	F_0	F_i	H_0	H_i	J_0	J_i
$\alpha = c_u/\sigma_v'$	0.25		0.25		0.25		0.29		0.29		0.29		0.34		0.34	
$\beta = E_{50}/c_u$	100		150		200		100		200		300		100		200	

Table 3.19 Initial Shear Modulus for HSS Model

Cases	$t = E_0/E_{ur}$	$k = G_0/E_{ur}$	$I_R = G_0/c_u$	G_0
$i = 1$	4	1.67	5β	$525\alpha\beta$
$i = 2$	6	2.50	7.5β	$787\alpha\beta$
$i = 3$	8	3.33	10β	$1050\alpha\beta$
$i = 4$	10	4.17	12.5β	$1312\alpha\beta$

Table 3.20 k Value for the Two Kinds of Clays

Soft Clay	$I_R = G_0/c_u$	k		
		$\beta = 100$	$\beta = 150$	$\beta = 200$
Singapore marine clay	700	2.33	1.56	1.17
Taipei Sungshan Formation	1000	3.33	2.22	1.67

3.4.3 Wall Deflection

To illustrate the small strain effect on wall deflection, the maximum wall deflection ratio is defined as

$$\mu_{ss} = \delta_{\mathrm{HSS}}/\delta_{\mathrm{HS}} \tag{3.7}$$

where δ_{HS} is the maximum wall deflection for the cases modeled by the HS model, and δ_{HSS} is the maximum wall deflection of the cases modeled by HSS model.

Table 3.21 shows the value of E_{ur} for case H_0, and the values of G_0 corresponding to cases H_1 to H_4. The results of cases H_0 to H_4 are shown in the following figures. Figure 3.24 shows the shape of lateral wall deflections at $h = 8$ m and final stage ($H_e = 20$ m) are similar for the various cases but magnitude of wall deflection decreases when small strain effect is distinct because of the increasing G_0. The wall deflection ratio μ_{ss} at various excavation stages (represented by depth of excavation H_e) with different maximum horizontal strain $\varepsilon_{x,max}$ of case H_0 is presented in Figure 3.25. It demonstrates the maximum wall deflections are similar when $G_0/E_{ur} = 1.67$ at various stages and decreases linearly when the ratio of G_0/E_{ur} increases. For example for $G_0/E_{ur} = 1.67$ and $h = 5$ m, μ_{ss} is approximately equal to 0.97. For $G_0/E_{ur} = 1.67$ and $h = 14$ m, μ_{ss} is close to unity. For $G_0/E_{ur} = 4.17$ and $h = 5$ m, μ_{ss} is approximately 0.69 compared with $\mu_{ss} = 0.85$ for $h = 14$ m .The reduction effect is more distinct at the initial excavation stages because of the small strain effect in which the soil has higher stiffness at lower strains.

Table 3.21 Results of Cases H

Cases	E_{ur}(kPa)	$k = G_0/E_{ur}$	G_0	$h = 8$ m	$H_e = 20$ m
H_0	10688	–	–	–	–
H_1	10688	1.67	17850	1	1
H_2	10688	2.50	26775	0.9	0.97
H_3	10688	3.33	35700	0.8	0.93
H_4	10688	4.17	44625	0.73	0.89

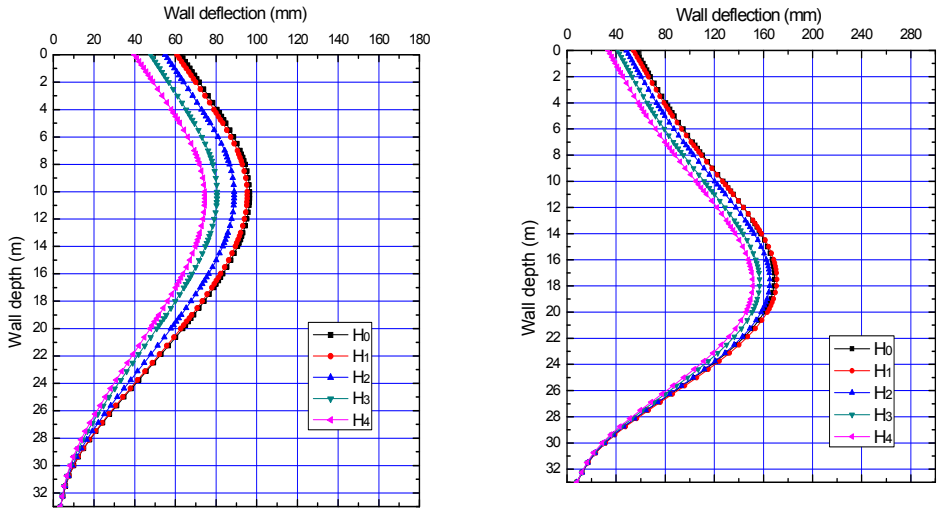

(a) (b)

Figure 3.24 Wall Deflection at Excavation Depth (a) $h = 8\text{m}$ (b) $\text{H}_\text{e} = 20\text{m}$

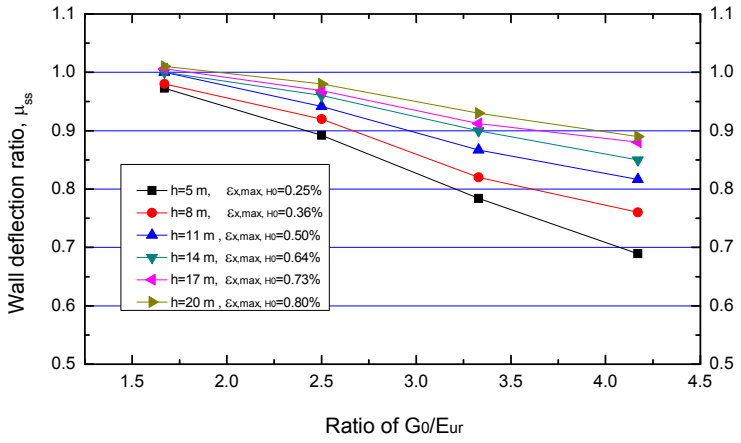

Figure 3.25 Wall Reduction Ratio for Different Cases at Different Depths of Excavation h

The two important factors that have been found to influence the excavation performance are the ratio G_0/E_{ur} and *the excavation stages* (which essentially reflects the strain level in the soil). Figure 3.26 shows the wall deflection ratio μ_{ss} at three excavation depths $h = 8\text{ m}$, $h = 14\text{ m}$ and $h = 20\text{ m}$ for all the cases

listed in Table 3.18. Defining $k = G_0/E_{ur}$, the plots in Figure 3.26 can be approximated by Eq. (3.8) or the chart in Figure 3.27. Although the other factors may affect the strain level of excavations, the influence is relatively smaller compared with k and h.

$$\mu_{ss} = 1 - 0.4(k - 1.67)(1 - \tfrac{1}{3}\sqrt[3]{h}) \tag{3.8}$$

Figure 3.27 or Eq. (3.8) can be used to assess if it is necessary to use the small strain HSS model instead of the HS model. For example for $k = 4.17$ and $h = 8$ m, $\mu_{ss} \approx 0.67$ which means that the maximum wall deflection predicted using the HSS would be about 2/3 times of the value predicted by the HS model. For $k = 4.17$ and $h = 18$ m, the overestimation by the HS model is approximately 16%. For $k = 1.67$, $\mu_{ss} = 1.0$ which means the HS model and the HSS model will give similar wall deflections.

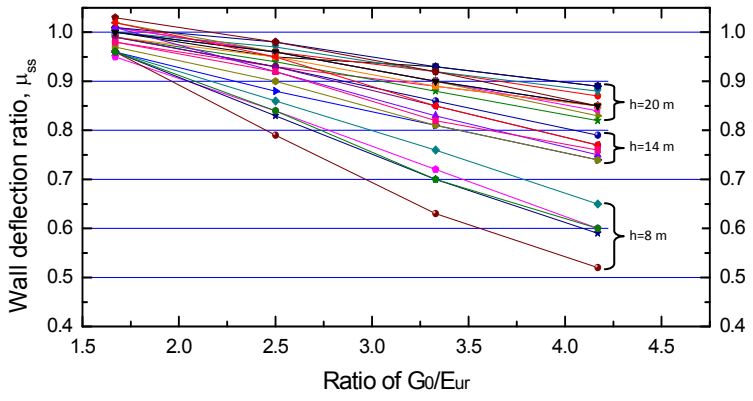

Figure 3.26 Reduction Ratio μ_{ss} at $h = 8$ m, $h = 14$ m and $h = 20$ m

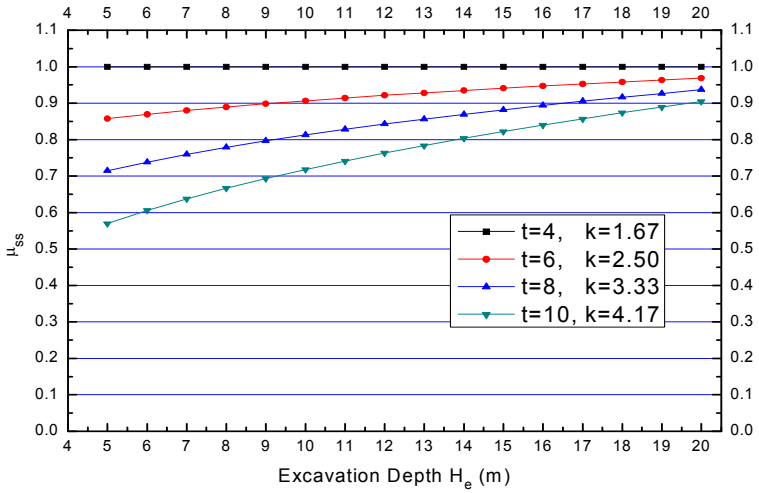

Figure 3.27 Chart for Estimating Reduction Ratio at Different Excavation Depths H_e $(t = E_0/E_{ur}\,,\ k = G_0/E_{ur})$

3.4.4 Surface Settlement

Another design consideration is the differential soil settlement behind the wall which can potentially damage nearby existing buildings. The settlement in the soil is related to the strain distribution, which in turn is related to the small strain behavior. Figure 3.28 presents the surface settlement at final excavation depth of 20 m for cases H_0, H_2 and H_4. The results indicate that the magnitude and settlement shape are similar for H_0 and H_2. For case H_4 with the higher value G_0, the shape and magnitude of the settlement is more distinct compared with case H_0, because of the small strain effect. The contours of vertical strain and shear strain at final depth of case H_2 and H_4 are compared in Figure 3.29 and Figure 3.30, respectively. The results show the region of lower strain at far distance behind wall is smaller in case H_4 than case H_2 while the differences are small in the region close to the wall. It accounts for the HSS models giving more distinct settlement troughs. The settlement ratios for the Case H are plotted in Figure 3.31, where the

settlement ratio is $R_v = \delta_{HSS,v}/\delta_{HS,v}$, $\delta_{HSS,v}$ and $\delta_{HS,v}$ are the maximum surface settlement modeled by HSS and HS, respectively. The results show that small strain effect has less influence on the magnitude of the soil settlement when the ratio of G_0/E_{ur} is low.

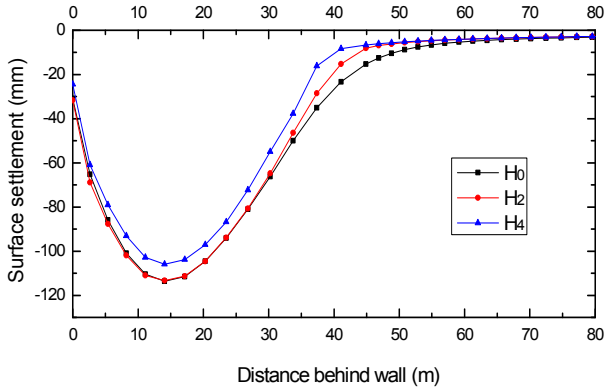

Figure 3.28 Surface Settlement at $H_e = 20$ m for Cases H_0, H_2 and H_4

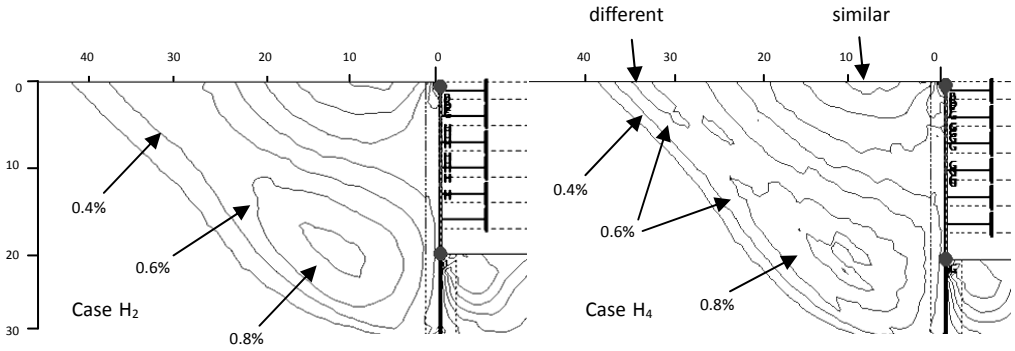

Figure 3.29 Comparison of Vertical Strain for Cases H_2 and H_4

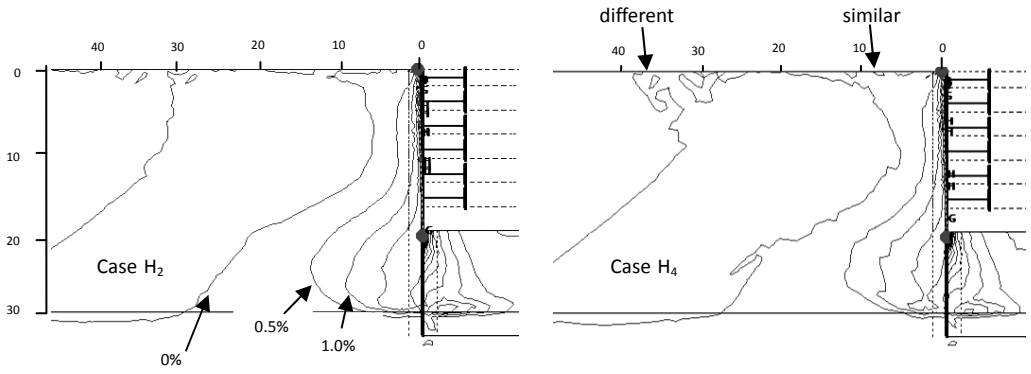

Figure 3.30 Comparison of Shear Strain for Cases H_2 and H_4

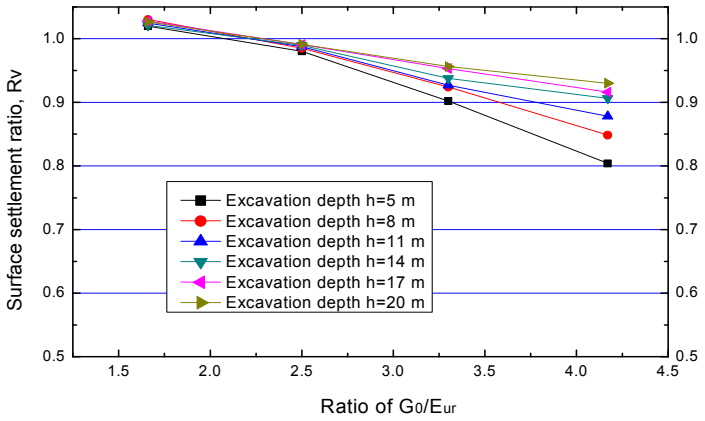

Figure 3.31 Surface Settlement Ratio for Different Cases at Different Excavation Depth h

3.4.5 Case History Validation

Additional analyses were also carried out for two cases from the literature to evaluate the influence of G_0.

3.4.5.1 Formosa Project

Details of this case are described in Section 3.3.6. In the FEM analyses, all soil layers are modeled by HS model first. The small strain effect is then investigated by applying HSS model to the dominant silty clay layer. The values for G_0 are shown in Table 3.22. Figure 3.32 and Figure 3.33 show the predicted wall deflection and surface settlement profiles. The results show the small strain effect is not distinct even with high G_0 when the excavation depth is large ($H_e = 20$ m). The small strain influence is more distinct at shallow excavation depth ($h = 10.15$ m). The result of μ_{ss} for the two stages in Table 3.22 coincides with the reduction ratio shown in Figure 3.37.

Table 3.22 Parameters and Results of Formosa

Case	$t = E_0/E_{ur}$	$k = G_0/E_{ur}$	G_0(kPa)	$h = 10.15$ m			$H_e = 20$ m		
				δ_h(mm)	μ_{ss}	δ_v(mm)	δ_h(mm)	μ_{ss}	δ_v(mm)
HS	–	–	–	40	–	28.5	64	–	48
HSS-1	4	1.67	29000	38.4	0.96	28.5	64.6	1	49
HSS-2	6	2.50	45000	35.4	0.88	26.4	61.4	0.96	47
HSS-3	8	3.33	60000	32.7	0.82	24.6	58.6	0.92	46
HSS-4	10	4.17	100000	28.3	0.71	21.1	53.8	0.84	42

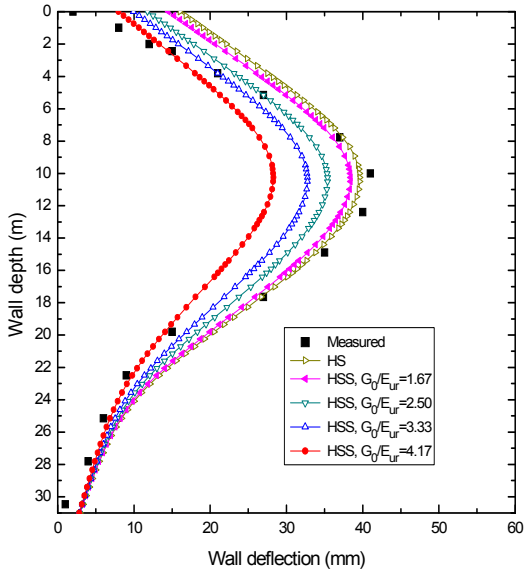

(a)

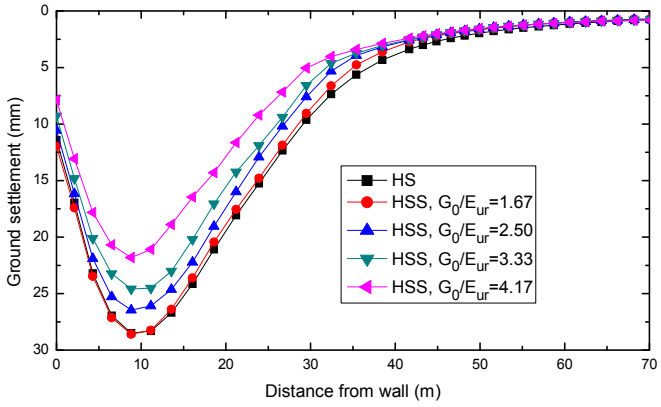

(b)

Figure 3.32 (a) Wall Deflection and (b) Surface Settlement for $h = 10.15$ m

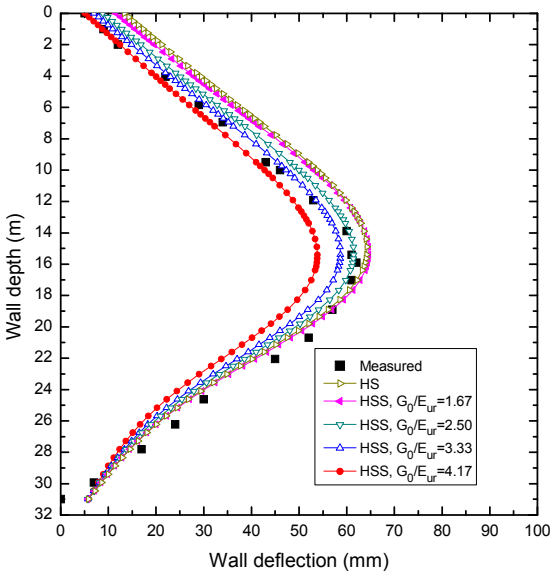

(a)

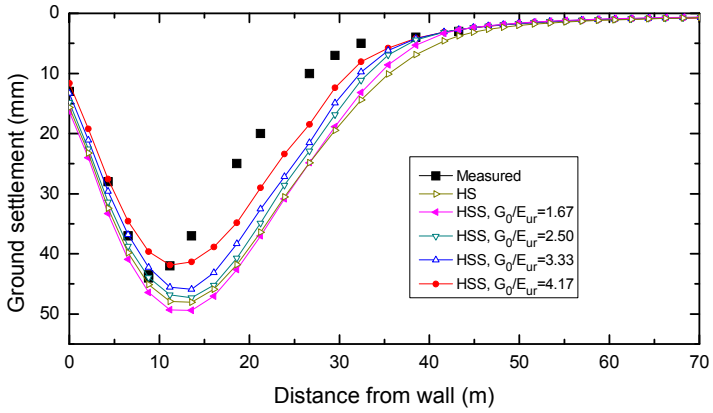

(b)

Figure 3.33 (a) Wall deflection and (b) Surface settlement for $H_e = 20$ m

3.4.5.2 Bugis MRT station

The excavation is located at Bugis MRT station in Singapore. The cross-section

adopted in the analysis is shown in Figure 3.34. The excavation was supported by 1.2 m thick diaphragm walls and seven levels of struts. The ground water table was 1.5 m below the ground surface. The dominant soft clay layers are the upper marine clay and lower marine clay, with soil strength ratio c_u/σ'_v of 0.33 and 0.25, respectively. The soil stiffness E_{50}/c_u for the marine clay in back-analysis is taken to be 100. Although the predicted wall deflections shown in Figure 3.36 are less than the measured wall deflection which was 135 mm, it can be used to study the small strain effect with different initial shear modulus G_0 in Table 3.23. The wall deflections and surface settlements at excavation depths of $h = 10.5$ m and $H_e = 18$ m of HS case and HSS cases are shown in Figure 3.35 and Figure 3.36, respectively. The maximum shear strains in soil body at $h = 10.5$ m and $H_e = 18$ m are 0.38% and 0.91%, respectively. The results of reduction ratio μ_{ss} in Table 3.23 at different excavation depths coincide with the reduction curve in Figure 3.27.

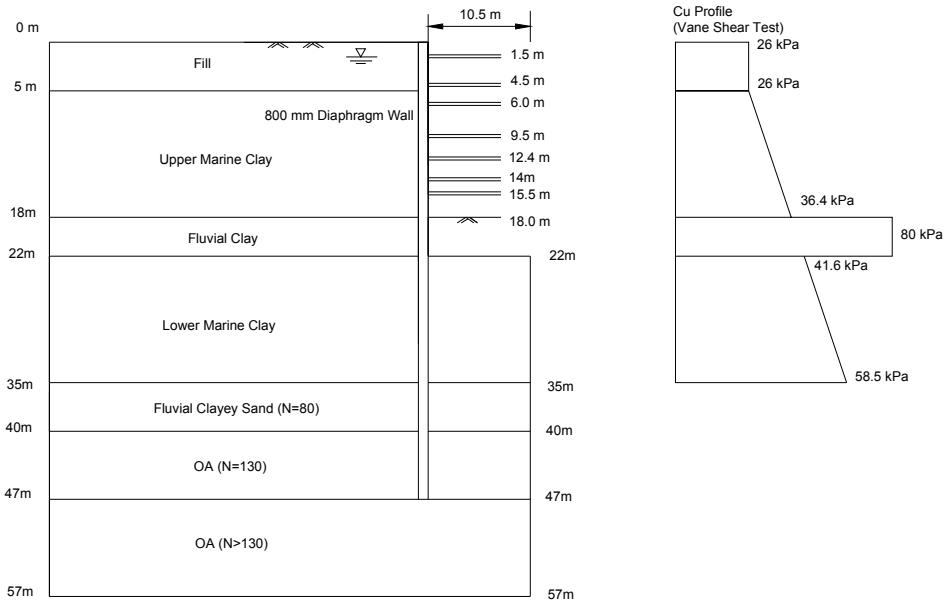

Figure 3.34 Cross-Section of Excavation at Bugis MRT Station (Halim, 2008)

Table 3.23 Parameter and Result of Bugis MRT Station

Case	$t = E_0/E_{ur}$	$k = G_0/E_{ur}$	G_0(kPa)		$h = 10.5\ m$			$H_e = 18\ m$		
			Upper marine	Lower marine	δ_h(mm)	μ_{ss}	δ_v(mm)	δ_h(mm)	μ_{ss}	δ_v(mm)
HS	–	–	–		60.7	–	44.6	107	–	80
HSS-1	4	1.67	16000	58.6	105	0.97	105	0.98	0.98	44.8
HSS-2	6	2.50	23000	54.4	101	0.90	101	0.94	0.94	42.1
HSS-3	8	3.33	31000	50	95.8	0.82	95.8	0.90	0.90	39
HSS-4	10	4.17	39000	41.1	85.3	0.68	85.3	0.80	0.80	31.3

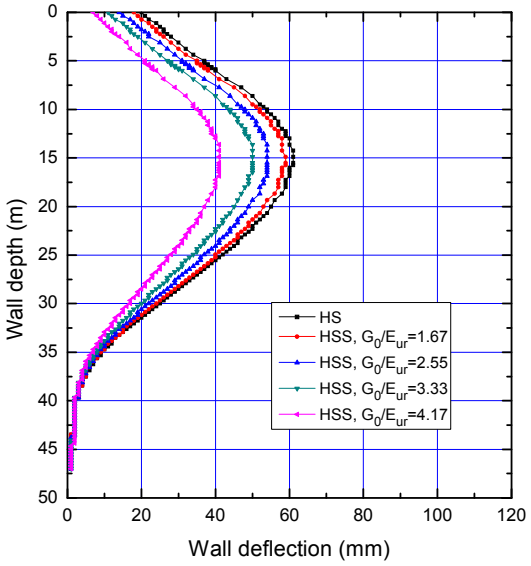

(a)

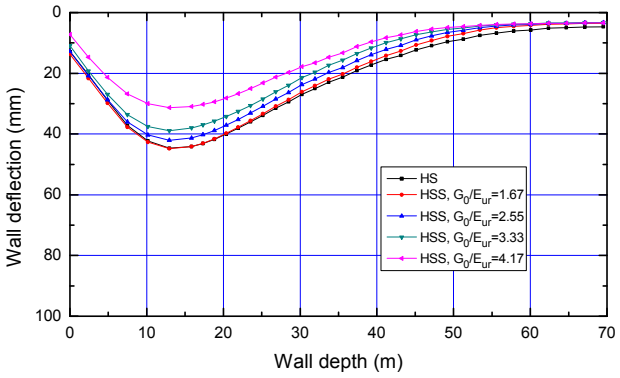

(b)

Figure 3.35 (a) Wall Deflections and (b) Surface Settlements for $h = 10.5$ m

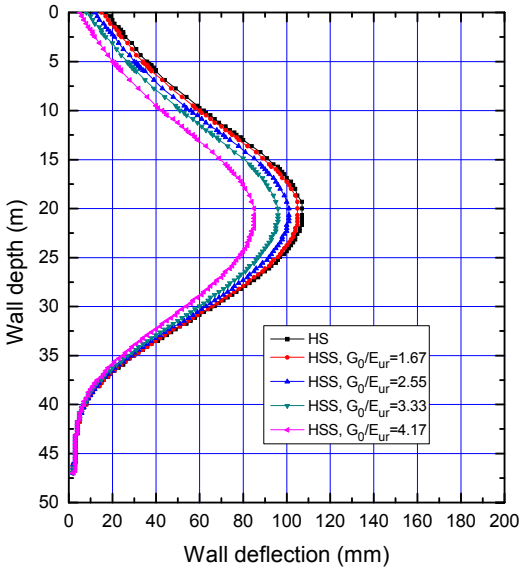

(a)

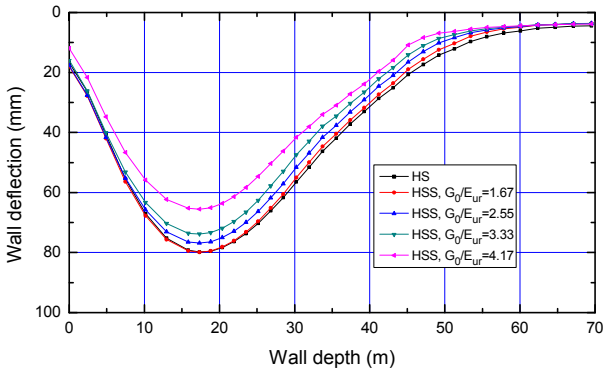

(b)

Figure 3.36 (a) Wall Deflections and (b) Surface Settlements for $H_e = 18$ m

3.4.6 Summary of this Section

Comparisons have been made between HSS and HS through a series of parametric study and two case histories. The results show the small strain effect is significantly dependent on the ratio k and excavation depth H_e for excavation problems. A coefficient μ_{ss} is introduced to assess the small strain effect if the effect is significant. Since the ratio of k for Singapore marine clay and Taipei clay is approximately defined in Table 3. This indicates the coefficient μ_{ss} for excavation problems in these two cities can be assessed properly.

3.5 Summary

1. It is suitable to use $E_{50} = 100\sim150c_u$ to model the stiffness of soft clay in HSS model except for the Formosa project when $E_{50} = 200c_u$ was more suitable.
2. The wall deflection and soil settlement of the cases modeled by HSS is slightly smaller than HS due to larger stiffness at small strain. The difference between

these two models is investigated through parametric study, which provides a coefficient to measure the small strain effect.

3. The small strain effect is illustrated in the Project Kotoku case when varying the value of small strain parameter G_0^{ref}. As explained in Chapter 2, the soft soil with smaller stiffness generates larger value of G_0^{ref}, which can show distinct effect of small strain both in wall deflection and soil settlement. However, for Singapore marine clay, the small strain effect is not significant due to lower ratio of G_0/c_u.
4. In the case for Lavender MRT Station and Farrer Park, smaller displacement close to the wall toe predicted by the HSS model shows the small strain effect compared with HS model and MC model.
5. The nonlinear effect especially on soil settlements is illustrated in the case studies when using the HSS and HS model. The HSS model more closely follows the shape of the measured soil settlement profiles compared with the MC model.

Chapter 4

PARAMETRIC STUDY FOR DIAPHRAGM WALLS IN SOFT CLAY

4.1 Introduction

With rapid economic development, more and more excavations are carried out in urban areas of coastal cities. The soil profiles in many of these locations comprise mostly of thick soft clays overlying stiff clay. To prevent basal heave failure and to reduce the movement of the wall toe, extending the wall length in the soft clay layer or even penetrating into the stiff clay layer is commonly carried out. Diaphragm walls are commonly used in these cases to minimize ground movement. To date, many empirical methods that have been proposed assume the wall is "floating" in the soft clay, without restraint at the wall toe. This chapter focuses on the specific situation of the wall penetrating into the stiff stratum. Parametric studies were carried out to evaluate the behavior of excavations with diaphragm walls in soft clay. The software PLAXIS 8.5 with the soil model HSS described in Chapter 3 that considers the small strain effect is used in all the analyses. Firstly, the influence of the various parameters such as soil stiffness and wall stiffness on the excavation behavior are investigated. Based on these findings, several simplified models to estimate wall deflection, ground movement and apparent pressure (for calculating strut forces) are proposed and presented in this Chapter.

4.2 Empirical Methods for Deep Excavations

Chapter 2 has introduced several empirical and semiempirical methods for estimating the excavation-induced maximum wall deflection (Mana and Clough

1981; Wong and Broms 1989; Clough and O'Rourke 1990; Hashash and Whittle 1996; Kung et al. 2007b), surface settlement profile (Peck 1969; Mana and Clough 1981; Clough and O'Rourke 1990; Ou et al. 1993; Hsieh and Ou 1998; Kung et al. 2007b) and apparent earth pressure diagrams (Terzaghi and Peck 1967; Peck 1969; Chang and Wong 1996). From these studies, the following factors have been shown to affect the excavation performance: excavation width and depth, wall stiffness, strut spacing, stiffness and preloading, depth to an underlying hard stratum, soil stiffness and strength distribution, dewatering operation, adjacent surcharge, soil consolidation and creep, and quality of workmanship.

4.3 Parametric Study

4.3.1 Factors Affecting Excavation Behavior

In this study, only the excavation geometry, soil parameters, and structural parameters are considered to evaluate their influence on the behavior of the specified profile of excavation. The seven factors evaluated are the excavation width B, excavation depth H_e, soil shear strength ratio c_u/σ_v', soil stiffness E_{50}/c_u, system stiffness $EI/\gamma_w h_{avg}^4$, and the soft clay thickness T as shown in Figure 4.1. The ranges of the parameters are shown in Table 4.1.

4.3.2 Geometry and Soil Conditions

Figure 4.1 shows the geometry of the hypothetical problem considered. The construction sequence comprises the following steps: (1) the wall is installed and the soil is initially excavated to a depth of 2 m; (2) the strut is then installed at 1 m higher than excavation level; (3) subsequent excavation is continued with struts at 3 m vertical spacing until the final excavation depth of 20 m is reached. For simplicity,

the water table is assumed to be at ground surface with hydrostatic pore pressure and the soil is subject to undrained shearing during excavation.

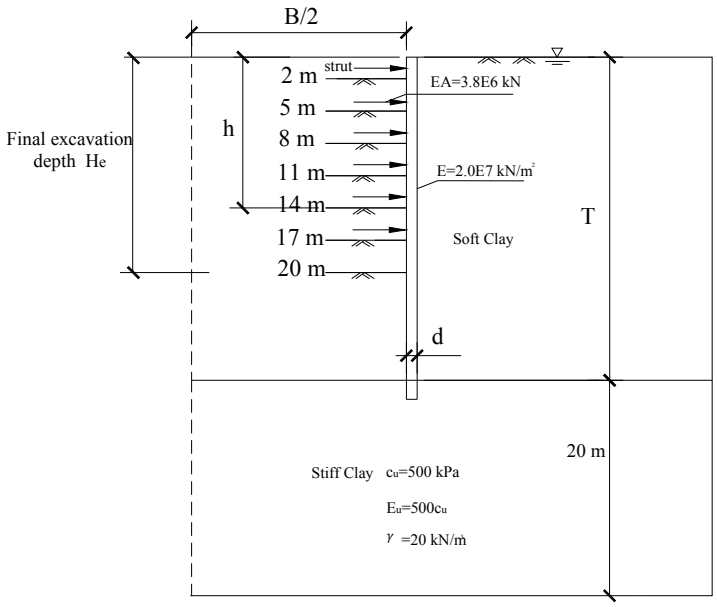

Figure 4.1 Geometry of Parametric Study

Table 4.1 Range of Parameters

Parameter	Range
c_u/σ_v'	$0.21, 0.25, 0.29, 0.34$
E_{50}/c_u	$100, 200, 300$
γ (kN/m^3)	$15, 17, 19$
T (m)	$25, 30, 35$
B (m)	$20, 30, 40, 50, 60$
H_e (m)	$8, 11, 14, 17, 20$
Wall stiffness $EI(\times 10^6$ kNm^2/m)	$0.36, 1.21, 2.88, 5.63$

4.3.3 Soil Parameters Adopted in FEM

As described in Chapter 2, the main parameters of the HSS model are the effective friction angle φ, the reference secant stiffness E_{50}^{ref}, and the reference initial shear modulus G_0^{ref}. When the ground water table is at the ground surface and assuming m = 1, $c_u/\sigma_v' = \alpha$, $E_{50}/c_u = \beta$ and $\sigma_3' = K_0\sigma_1'$ in the HSS model, E_{50}^{ref} is the same for different T and γ in Eq. (4.1). The value of φ is derived from Eq. (3.3). The various φ and E_{50}^{ref} values are shown in Table 4.2 and 4.3, respectively.

$$E_{50}^{ref} = \frac{E_{50}}{\left(\frac{-\sigma_3'}{p^{ref}}\right)^{\overline{m}}} = \frac{\alpha c_u}{\left(\frac{K_0 \times c_u}{\beta \times p^{ref}}\right)^{\overline{m}}} = \frac{\alpha\beta p^{ref}}{K_0} \tag{4.1}$$

Table 4.2 Effective Friction Angle for Soft Clay in HSS

c_u/σ_v'	0.21	0.25	0.29	0.34
φ(°)	19	22.3	25.6	29.6
K_0	0.67	0.62	0.57	0.51

Table 4.3 Reference Secant Stiffness for Soft Clay in HSS

c_u/σ_v'	E_{50}^{ref} (kPa)			
	$\frac{E_{50}}{c_u} = 100$	$\frac{E_{50}}{c_u} = 200$	$\frac{E_{50}}{c_u} = 300$	$\frac{E_{50}}{c_u} = 400$
0.21	3114	6228	9342	12456
0.25	4031	8062	12093	16124
0.29	5105	10210	15315	20420
0.34	6721	13442	20163	26884

The small strain parameters $\gamma_{0.7}$ is assumed to be 2×10^{-4} and G_0^{ref} is obtained from the following equation which is described in Section 2.9.3:

$$G_0^{ref} = 0.42tK_0E_{ur}^{ref} \tag{4.2}$$

4.4 Results of Parametric Study

More than 200 hypothetical cases were analyzed in this study and the results are presented in this section. Sensitivity studies of the various parameters on the wall deflection were also carried out.

4.4.1 Effect of Wall Penetration on Deflection

Hashash and Whittle (1996) pointed out that the wall length has a minimal effect on the prefailure deformations for excavations in deep deposits of clay where there is no restraint on toe movement, although it is believed to have a significant influence on the location of the failure mechanism within the soil. Ashraf and Bolton (2006) proposed a method to predict wall deflection depending on the defined relationship of wall length and 'wavelength' according to whether the wall toe is fixed or free, suggesting that the wall deflection is very much related with its fixity condition. In this study, the wall is assumed to penetrate into the stiff clay stratum resulting in a restraint of the wall toe movement. To study the influence of the wall toe restraint, cases for $B = 40$ m, $H_e = 20$ m, $c_u/\sigma_v' = 0.29$, $E_{50}/c_u = 200$, $\gamma = 17$ kN/m^3, and $T = 30$ m with different penetration depths ($D = -2$ m~5 m, positive represents penetrating into the stiff clay) were analyzed to investigate the penetration effect on excavation behavior. The results in Figure 4.2 with penetration depths of -2 m and 5 m show that the penetration effect significantly influences the profiles of wall deflection for deep excavation depths ($h \geq 17$ m) whereas the wall deflection

profiles are similar during the initial excavation stages. Defining the deflection ratio μ_D as the maximum wall deflection divided by the maximum wall deflection for the case with $D = 3$ m, Figure 4.3 presents μ_D at two different excavation depths with two different wall thickness d. The plot indicates that as long as the wall penetrates into the stiff clay (positive D values) μ_D is almost constant for different wall penetration depths. The reason for the different performance of wall deflections with different penetration depths is analogous to the different deformation mechanisms for cantilever and simply supported beams.

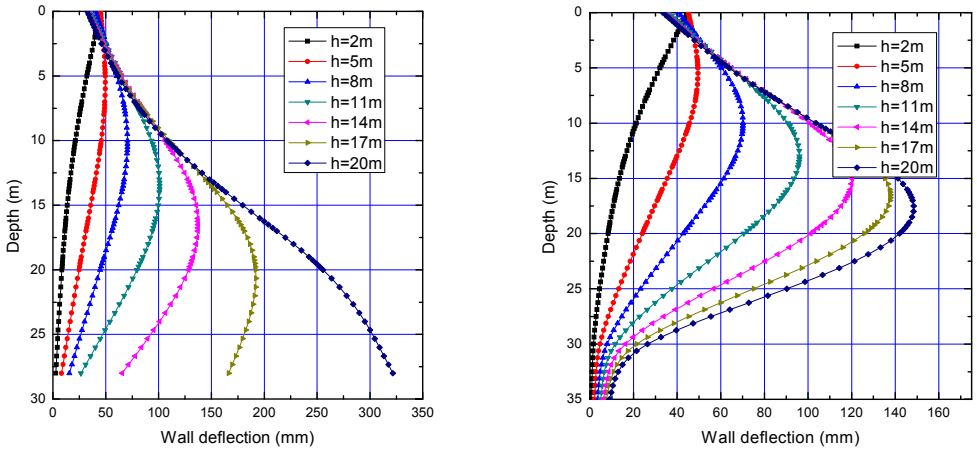

Figure 4.2 Wall Deflection for (a) $D = -2$ m and (b) $D = 5$ m

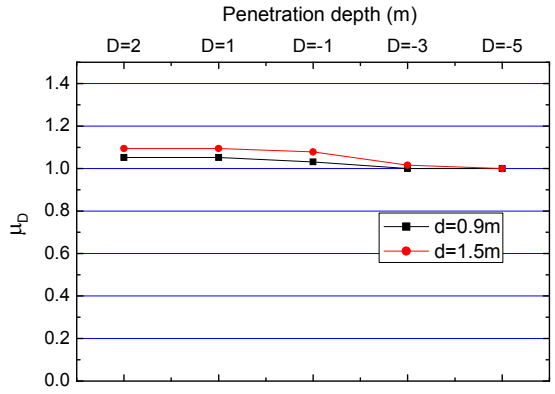

(a)

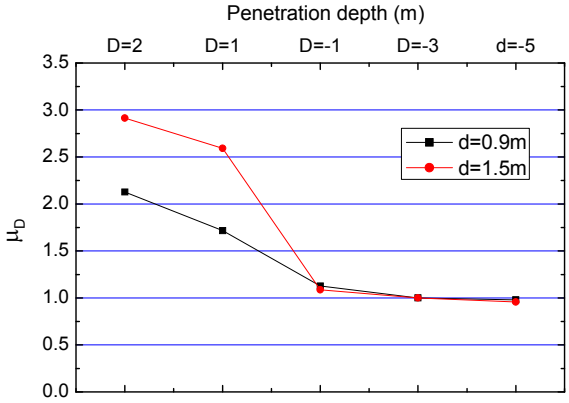

(b)

Figure 4.3 μ_D Plots at (a) $h = 11$ m and (b) $h = 20$ m

4.4.2 Effect of Strut Stiffness on Wall Deflection

The excavation strutting system is one of structural components affecting the wall deflection. In this study, the vertical strut spacing h_{avg} is fixed at 3 m as is common in many excavation sites. The strut type adopted in the analysis is a typical steel column with width 350 mm, flange thickness 19 mm, web thickness 12 mm and weight 137 kg/m. The sectional area is $17400\ \text{mm}^2$. Assuming the Young's modulus E of the strut is $2 \times 10^8\ \text{kN/m}^2$ and horizontal strut spacing as 4 m, the

strut stiffness per meter can be obtained as

$$EA = 2 \times 10^8 \text{ kN/m}^2 \times 17400 \text{ mm}^2 \times 10^{-6}/4 \text{ m}$$
$$= 8.7 \times 10^5 \text{ kN/m} \quad (4.3)$$

To investigate the effect of strut stiffness, a series of analyses for $B = 40$ m, $H_e = 20$ m, $c_u/\sigma_v' = 0.34$, $E_{50}/c_u = 200$, $\gamma = 17 \text{ kN/m}^3$, and $T = 30$ m with different strut stiffness were carried out to study the effect of strut stiffness. The results as presented in Figure 4.4 show that the deflection ratio μ_s (which is defined as the maximum wall deflection divided by the maximum wall deflection for the case with $EA = 8.7 \times 10^5$ kN/m) decreases with increasing strut stiffness, but the effect is not very significant when the strut is stiff. Similar findings were reported by Poh et al. (1997). The results also show there is no correlation between strut stiffness and wall stiffness. The factor μ_s will be used later in section 4.5.3 to predict deflections.

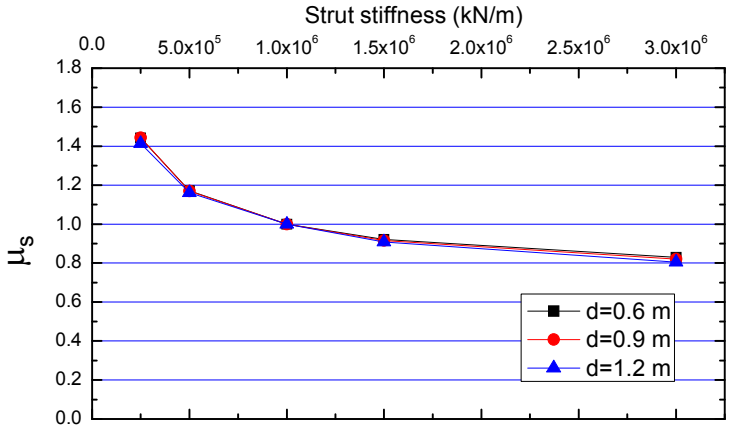

Figure 4.4 Plot of μ_s versus Strut Stiffness

4.4.3 Effect of Ground Water Table on Deflection

In all the analyses the ground water table was assumed at the ground surface, which is the most unfavorable condition. In many situations with soft clay, the water could be $1-2$ m below the ground surface. To study the influence of the ground water table, analyses (Table 4.4) were carried out for various ground water levels. Defining the deflection ratio μ_w as the maximum wall deflection divided by the maximum wall deflection for the case where the ground water table is at the ground surface, the results as plotted in Figure 4.5 show that μ_w decreases almost linearly with decreasing ground water level. The factor μ_w can be estimated as $\mu_w = 1 - 0.1l$, where l is the depth of the ground water table below the ground surface (in metres) and $l \leq 2$. The factor μ_w will be used later in section 4.5.3 to predict deflections as well.

Table 4.4 Parameters of Cases for μ_w

Case 1w	B=40 m, T=30 m, γ=17 kN/m^3, c_u/σ'_v =0.29, E_{50}/c_u=200, H_e = 20 m, d=0.9 m
Case 2w	B=40 m, T=30 m, γ=19 kN/m^3, c_u/σ'_v =0.29, E_{50}/c_u=200, H_e = 20 m, d=0.9 m
Case 3w	B=40 m, T=30 m, γ=19 kN/m^3, c_u/σ'_v =0.29, E_{50}/c_u=200, H_e = 20 m, d=1.2 m
Case 4w	B=30 m, T=25 m, γ=17 kN/m^3, c_u/σ'_v =0.29, E_{50}/c_u=200, H_e = 20 m, d=0.9 m
Case 5w	B=50 m, T=35 m, γ=17 kN/m^3, c_u/σ'_v =0.29, E_{50}/c_u=200, H_e = 20 m, d=0.9 m

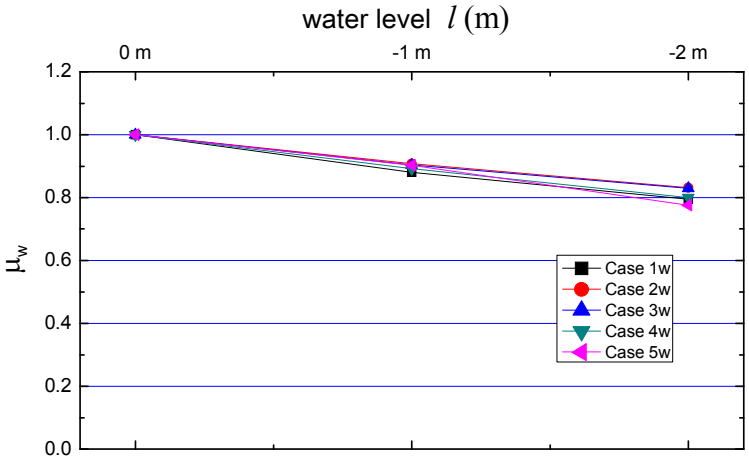

Figure 4.5 Plot of μ_w versus Water Level l

4.4.4 Effect of Wall Stiffness on Deflection

This study only considered the use of diaphragm walls which has been widely used in the last three decades. A series of analyses with different wall stiffness for $B = 30$ m, $c_u/\sigma'_v = 0.29$, $E_{50}/c_u = 200$, $\gamma = 19$ kN/m^3, and $T = 30$ m were conducted to study its effect on wall deflection. Figure 4.6 shows the maximum wall deflections for different wall thickness d at various stages of excavation. The results show the wall stiffness plays a significant role on wall deflection for excavations at greater depths whereas the effect is smaller in the initial few excavation stages. The conclusions are similar to the findings by Yoo (2001), which showed the significant influence of wall stiffness on maximum wall deflection when the wall was embedded in a rock stratum.

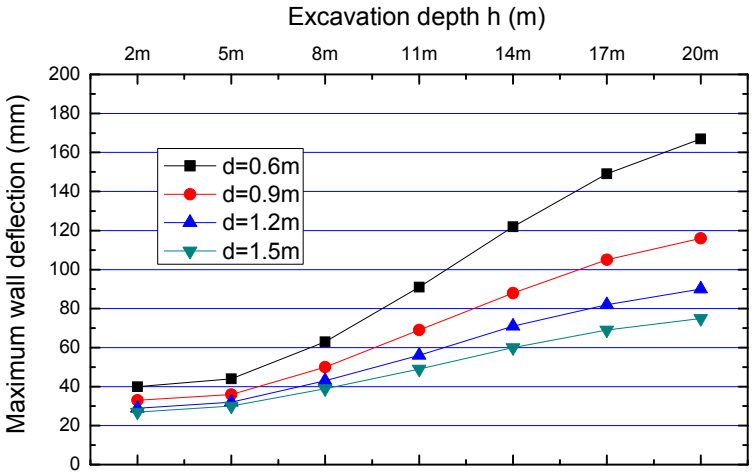

Figure 4.6 Effect of Wall Stiffness on Deflection

4.4.5 Effect of E_{50}/c_u on Wall Deflection

The influence of soil stiffness ratio was also investigated for cases with $B = 30$ m, $c_u/\sigma_v' = 0.29$, $\gamma = 17\,\text{kN/m}^3$, and $T = 30$ m. The plots of maximum wall deflection at $H_e = 20$ m for different wall stiffness are presented in Figure 4.7. The influence of E_{50}/c_u is more significant for lower soil stiffness ratios especially for cases with lower wall thickness. Yoo (2001) also reported similar findings. Figure 4.8 presents the maximum wall deflections at various excavation stages for different soil stiffness. The result shows that the shape of wall deflection versus excavation depth plot is a function of the E_{50}/c_u ratio.

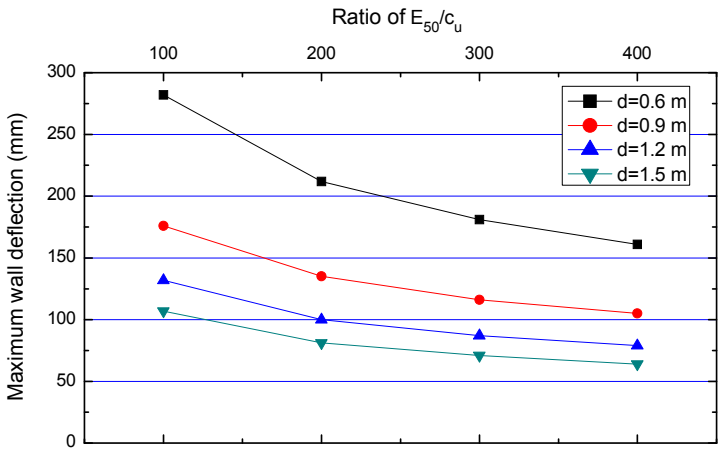

Figure 4.7 Effect of Soil Stiffness on Wall Deflection at $H_e = 20$ m

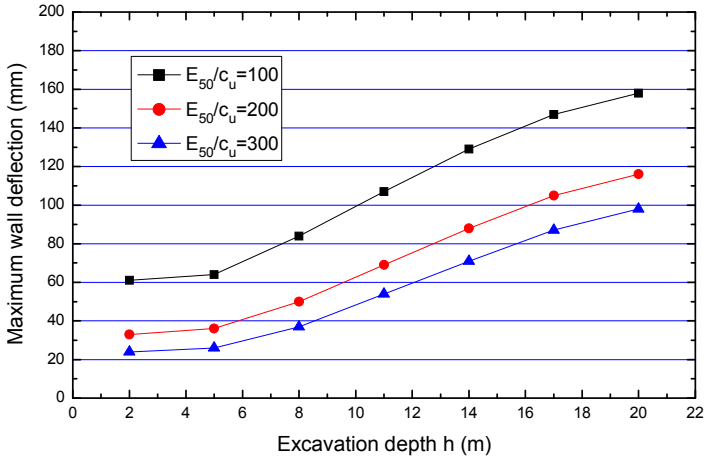

Figure 4.8 Effect of Soil Stiffness on Wall Deflection ($d = 0.9$ m)

4.4.6 Effect of Soil Unit Weight on Wall Deflection

The influence of the soil unit weight for the cases with $B = 30$ m, $H_e = 20$ m, $c_u/\sigma_v' = 0.29$, $E_{50}/c_u = 200$, and $T = 30$ m is shown in Figure 4.9. The soil unit weight does not significantly influence the maximum wall deflection at higher

wall stiffness, but the effect is significant at lower wall stiffness (thickness). Figure 4.10 shows the shapes of plots of maximum wall deflection versus excavation depth h (wall deflection path, which will be defined and introduced in Section 4.4.9) are approximately the same for different soil unit weight.

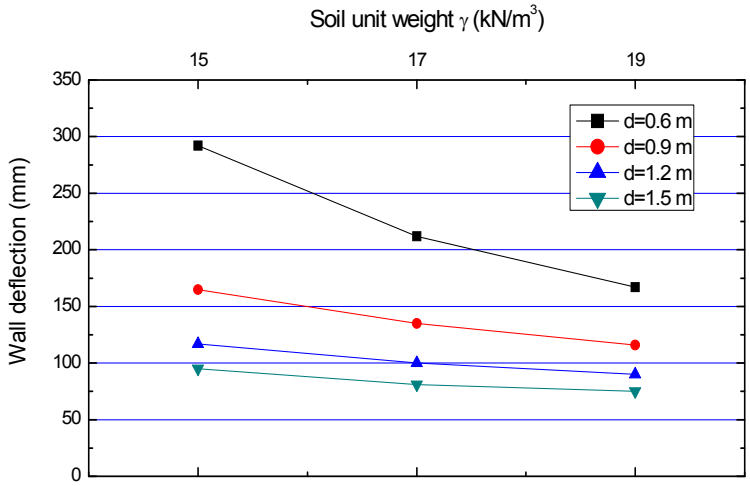

Figure 4.9 Effect of Soil Unit Weight at $H_e = 20$ m

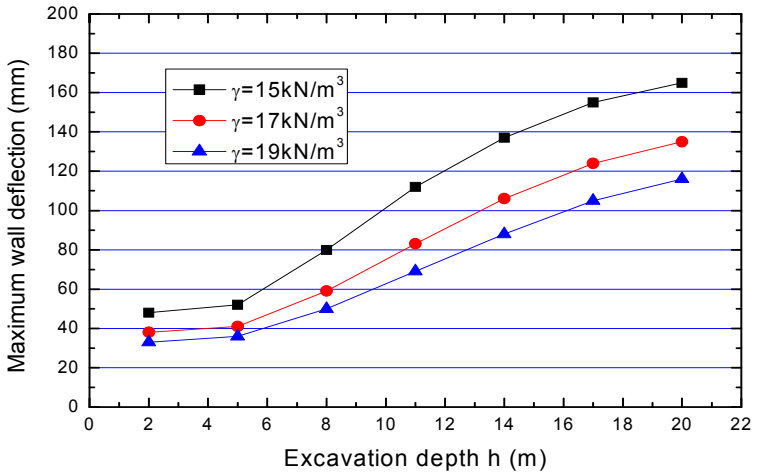

Figure 4.10 Effect of Soil Unit Weight on Wall Deflection ($d = 0.9$ m)

4.4.7 Effect of Soil Strength Ratio on Wall Deflection

The influence of the soil strength ratio c_u/σ_v' for the cases with $B = 40$ m, $\gamma = 17$ kN/m^3, $E_{50}/c_u = 200, d = 0.9$ m, $T = 30$ m is presented in Figure 4.11. The results show the maximum wall deflection decreases with the increase of soil strength.

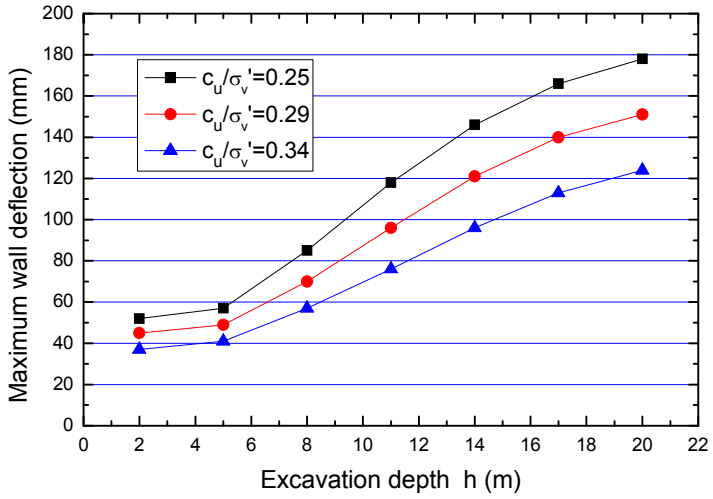

Figure 4.11 Effect of Soil Strength Ratio on Wall Deflection

4.4.8 Effect of Clay Thickness and Excavation Width on Deflection

A previous study by Wong and Broms (1989) pointed out that the wall deflection is significantly affected by the presence of the hard stratum both in the cases of wall penetrating and not penetrating into the hard stratum. Kung et al. (2007b) introduced a factor K that considered the effect of hard stratum to modify the regression model for wall deflection.

$$K = 1.5\,T'/B + 0.4 \qquad \text{for } T'/B \leq 0.4 \qquad (4.4\text{ a})$$

$$K = 1 \qquad \text{for } T'/B > 0.4 \qquad (4.4\text{ b})$$

where T' is the depth to hard stratum measured from the current excavation level.

However, the factors of hard stratum, excavation width and excavation depth are complex to be incorporated in one coefficient. In this study, analyses have been conducted to study the effect of clay thickness T and excavation width B on wall deflection. The results of cases for $B = 40$ m, $c_u/\sigma_v' = 0.29$, $E_{50}/c_u = 300, d = 0.9$ m, $\gamma = 19$ kN/m^3 with different clay thickness are presented in Figure 4.12. The ratio μ_T is defined as the maximum wall deflection divided by the maximum wall deflection for the case with $T = 40$ m. The maximum wall deflection at various excavation depths indicate that the effect of hard stratum $(T' = T - H_e)$ will be significant when the ratio of H_e/T is larger. Since the wall penetrates into the harder stratum in all these cases, the effect of H_e/T considered here is essentially the combined effect of hard stratum thickness and toe fixity.

Figure 4.13 shows the effect of excavation width on maximum wall deflection. The result shows the maximum wall deflection increases with the increase of excavation width B at various excavation depths. The shapes of plots of maximum wall deflection versus excavation depth h are approximately the same.

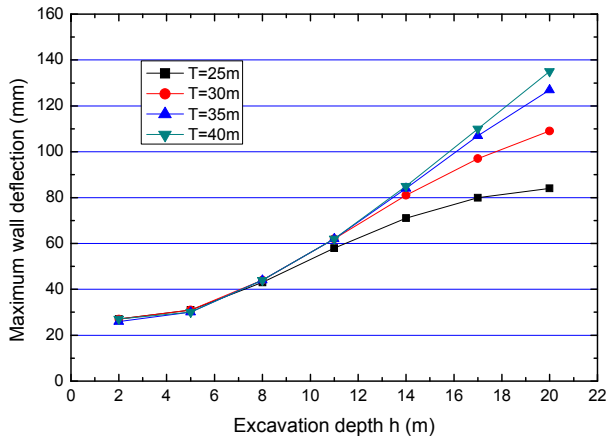

(a)

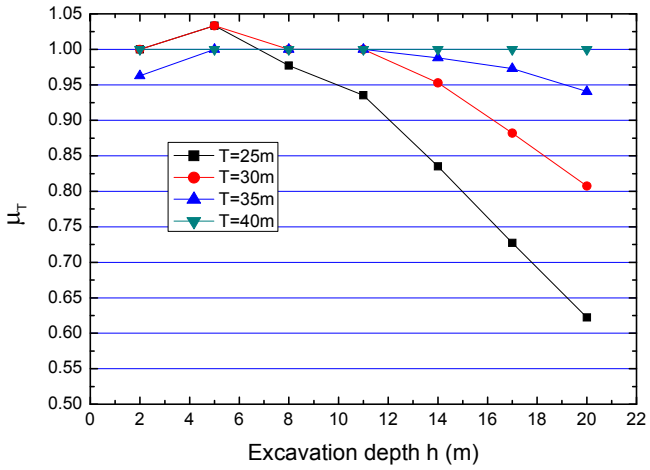

(b)

Figure 4.12 Effect of Clay Thickness on (a) Maximum Wall Deflection (b) μ_T

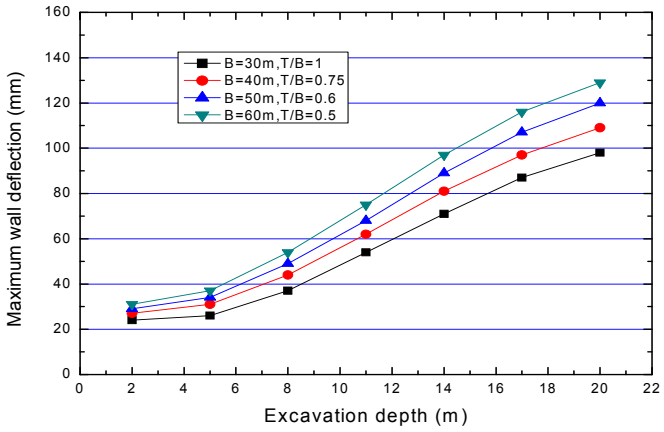

Figure 4.13 Effect of Excavation Width on Maximum Wall Deflection ($T = 30$ m)

Since the diaphragm wall stiffness (Figure 4.6) does not affect the shape of wall deflection as much as the clay thickness, as an approximation, the effect of hard stratum may expressed by the factor μ_T as a function of H_e/T

$$\mu_T = -2.5\left(\frac{H_e}{T} - 0.4\right)^2 + 1\,, \quad \text{for} \quad H_e/T > 0.4 \tag{4.5a}$$

$$\mu_T = 1, \quad \text{for} \quad H_e/T \leq 0.4 \tag{4.5b}$$

Eq. (4.5) was found to agree with the results of the cases in Figure 4.12 (b). Eq. (4.5) may also be expressed in chart form as shown in Figure 4.14.

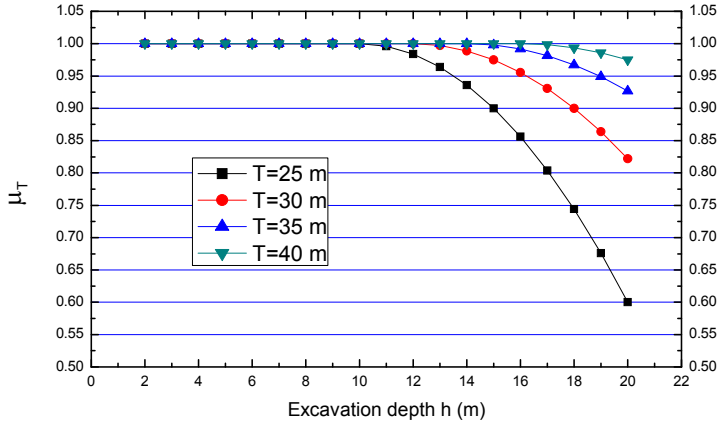

Figure 4.14 Chart for reduction ratio μ_T

4.4.9 Wall Deflection Path

The concept of wall deflection paths herein are the plots of maximum wall deflections versus depths of excavation. The wall deflection paths converge to a narrow band as excavation goes beyond a depth of approximately 10 m (Hwang and Moh, 2007). Figure 4.15 shows the typical wall deflection profiles and deflection paths of diaphragm walls in soft ground, which consists of a cantilever shape in the initial stage and spindle shapes at subsequent excavation stages. In Figure 4.15, the 'x axial' represents the maximum wall deflection at each stage and 'y axial' represents the corresponding excavation depth for each stage.

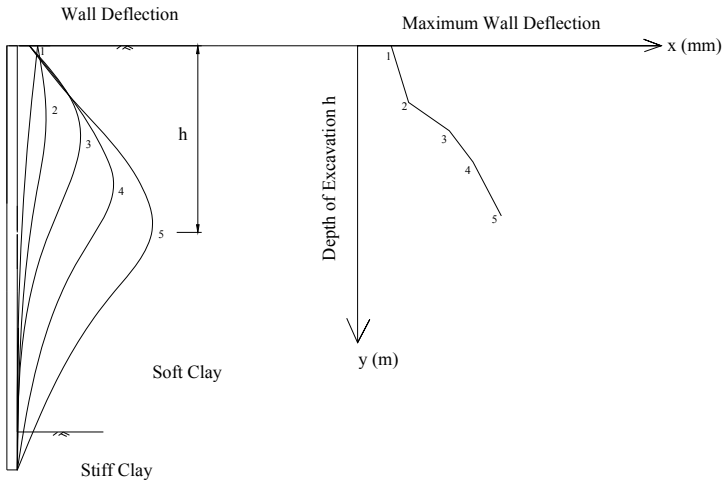

Figure 4.15 Deflection Profiles and Deflection Paths of Diaphragm Walls in Soft Ground (modified from Hwang and Moh, 2007)

Different wall deflection paths have been illustrated for different parameters in previous sections. The shape of wall deflections at initial excavation stages is cantilever which is mainly affected by excavation width B, soil strength ratio c_u/σ_v', soil stiffness ratio E_{50}/c_u, and soil unit weight γ. The wall stiffness (EI) plays an important role on wall deflection path after the struts are installed, as has been shown in Figure 4.6. The shapes of the wall deflection paths are almost similar for cases with different values for parameters in previous section excluding for the clay thickness T in Section 4.4.8. The relationship between wall deflection path and excavation depth $(h \geq 8\ \text{m})$ is linear for the case with $T = 40\ \text{m}$ in Figure 4.12(a), where h/T is small $(h/T \leq 0.5)$ that the effect of hard stratum can be neglected. The deflection path tends to be with the same slope η at the following stages when the wall deflection profile is spindle if there is no effect of hard stratum $(H_e/T \leq 0.4)$ as shown in Eq. (4.5). Since the main factor affected the shape of wall deflection path is the effect of hard stratum, the wall deflection path can be estimated considering this factor as outlined below.

The simple method is used for predicting the wall deflection path when measured data for wall deflections are available provided the wall profile is spindle. Assuming the excavation depth and the measured wall deflection at the first stage of spindle is h_{e1} and δ_1, respectively, the excavation depth and measured wall deflection of the next stage is h_{e2} and δ_2, respectively ($h_{e1}/\mathrm{T} \leq 0.4$, $h_{e1}/\mathrm{T} \leq 0.4$). So the slope is:

$$\eta_1 = \frac{\delta_2 - \delta_1}{h_{e2} - h_{e1}} \tag{4.7}$$

As excavation proceeds,

$$\eta_i = \frac{\delta_{i+1} - \delta_i}{h_{e(i+1)} - h_{ei}} = \lambda_i \eta_1, \ i \geq 2 \tag{4.8}$$

where λ_i is the reduction factor. As an approximation, the effect of hard stratum may expressed as

$$\lambda_i = \frac{1}{1.5h_i/T + 0.4}, \quad \text{for} \quad h_i/T > 0.4 \tag{4.9a}$$

$$\lambda_i = 1, \quad \text{for} \quad h_i/T \leq 0.4 \tag{4.9b}$$

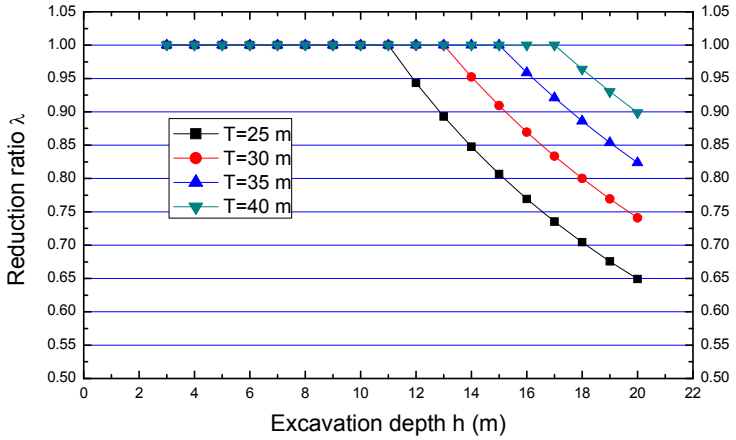

Figure 4.16 Chart for Reduction Ratio λ_i

Hence

$$\delta_{i+1} = \delta_i + \lambda_i \eta_1 \left(h_{(i+1)} - h_i\right),\ i \geq 2 \tag{4.10}$$

The finial wall deflection can be determined as

$$\delta_n = \delta_2 + \eta_1 \sum_{i=2}^{n} \lambda_i \left(h_{(i+1)} - h_i\right) \tag{4.11}$$

In the following, the results for four case histories are shown to demonstrate the validity of Eq. (4.10) and Eq. (4.11).

4.8.1.1 TNEC and Formosa Case

The measured wall deflections of TNEC and Formosa Case are presented in Figure 4.17. The soil properties and excavation depths are shown in Figure 4.18. The hard stratum level for the two cases is 33 m and 31 m, respectively. The wall deflection at stage 3 and 4 are assumed to be as δ_1 and δ_2, respectively, and are listed in Table 4.5 to predict the wall deflection at the next stages 5, 6, 7. The result shows the difference between the predicted deflections and measured deflections for TNEC case are small. For the Formosa case, the differences are slightly larger, with the maximum difference being 23%.

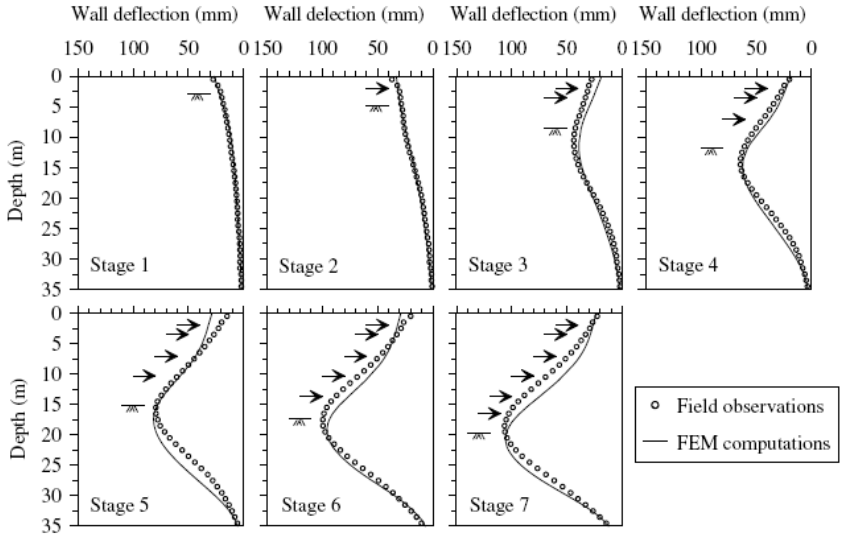

(a)

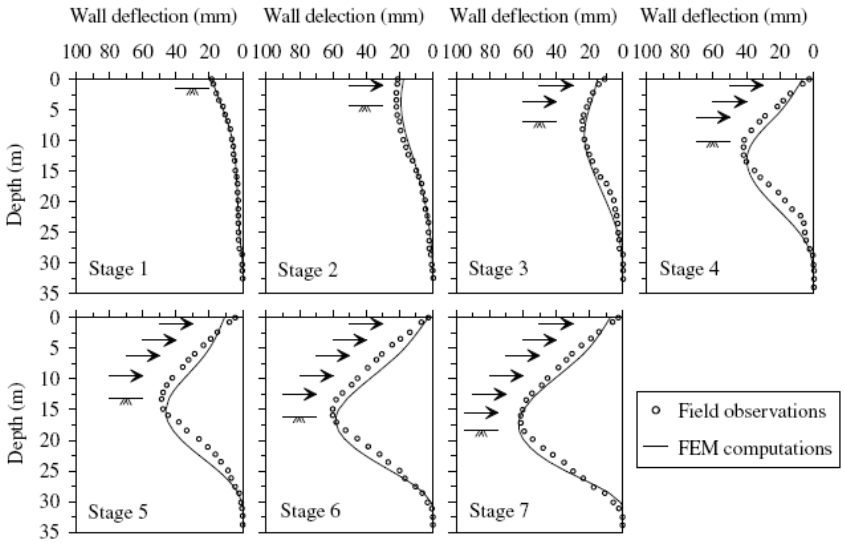

(b)

Figure 4.17 Wall Deflection Profiles of (a) TNEC and (b) Formosa (Tang and Kung, 2008)

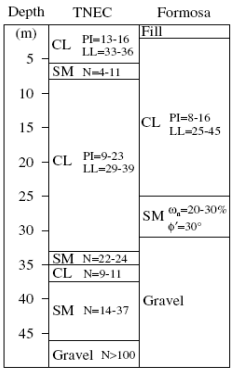

Excavation depth and depth where strut was installed in the TNEC and Formosa excavation case histories

Stage No.	TNEC case		Formosa case	
	H_e (m)	H_s (m)	H_e (m)	H_s (m)
1	2.8	–	1.6	–
2	4.9	2.0	4.3	1
3	8.6	3.5&0	6.9	3.7
4	11.8	7.1	10.15	6.2
5	15.2	10.3	13.2	9.5
6	17.3	13.7	16.2	12.5
7	19.7	16.5	18.45	15.5

H_e is the excavation depth H_s is the depth where the strut was installed.

Figure 4.18 Soil Profile and Excavation Depths for TNEC and Formosa (Tang and Kung, 2008)

Table 4.5 Prediction of Wall Deflection Path for TNEC and Formosa

Case	η_1	δ_1 (mm)	δ_2 (mm)	λ_2	λ_3	λ_4	Stage 5		Stage 6		Stage 7	
							δ_p (mm)	δ_m (mm)	δ_p (mm)	δ_m (mm)	δ_p (mm)	δ_m (mm)
1-TNEC	5.94	49	68	0.91	0.84	0.77	86.5	82	97.0	100	108.0	108
2-Formosa	4.92	25	41	0.96	0.84	0.77	55.4	50	67.9	60	76.4	62

Notes: δ_p = predicted deflection, δ_m = measured deflection

4.8.1.2 Kotoku and Farrer Park

Two case histories described in Chapter 3 are used to valid the wall deflection path. The wall deflection profiles at every stage and every excavation depth of the two cases are shown in Figure 4.19 and Figure 4.20, respectively. The analyses assume wall deflection predicted by FEM as 'measured deflection'. Since only the measured data at the end of excavation to formation level are available for these two cases. The wall deflection at stage 3 and 4 are assumed to be as δ_1 and δ_2, respectively. The predicted wall deflection paths from stage 5 to stage 7 are presented in Table 4.6, which show that reasonable results are obtained for the case

of Farrer Park whereas a slightly smaller wall deflection is predicted for case of Kotoku because the wall toe did not penetrated into the stiff clay.

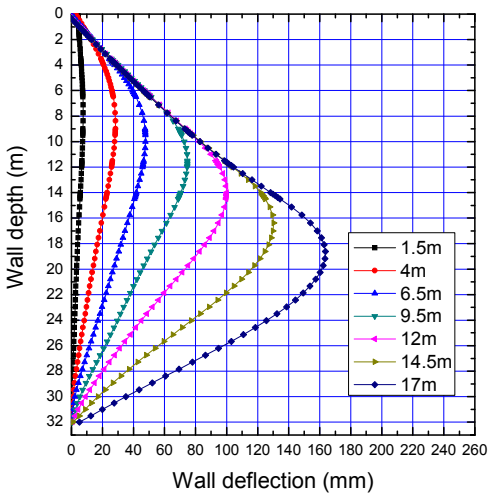

Figure 4.19 Wall Deflection Profiles of Kotoku at Various Stages

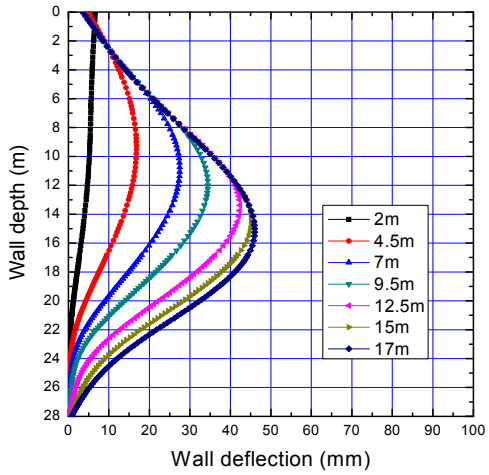

Figure 4.20 Wall Deflection Profiles of Farrer Park at Various Stages

Table 4.6 Prediction of Wall Deflection Path for TNEC and Formosa

Case	η_1	δ_1 (mm)	δ_2 (mm)	λ_2	λ_3	λ_4	Stage 5		Stage 6		Stage 7	
							δ_p (mm)	δ_m (mm)	δ_p (mm)	δ_m (mm)	δ_p (mm)	δ_m (mm)
3-Kotoku	8.96	47.8	74.7	1	0.88	0.8	97	100	117	130	135	163
4-Farrer Park	2.76	25	41	0.80	0.70	0.64	41	42	46	45	49	47

4.5 Response Surface for Deformations

4.5.1 Response Surface Method (RSM)

Response surface methodology (RSM) is a collection of statistical design and numerical optimization techniques used to optimize process and product designs (Myers, et al. 2004). RSM was first introduced by Box and Wilson (1951) which laid the foundations for the method.

The basic concept of RSM involves the approximation of the unknown implicit performance function by using a simple and explicit function. The response surface is constructed from data obtained from a set of designed experiments or numerical analyses. Coefficients in the explicit function can be obtained by performing regression analysis. Once the response surface is determined, reliability analysis can be carried out as presented in Chapter 5. The second-order polynomial is adopted herein:

$$y = a + \sum_{i=1}^{n} b_i x_i + \sum_{i=1}^{n} c_i x_i^2 + \sum_{i=1}^{n} \sum_{\substack{j=1 \\ i<j}}^{n} d_{ij}\, x_i x_j \tag{4.12}$$

where a, b_i, c_i, d_{ij} are coefficients to be determined from multiple linear regression, and x_i, x_j are the independent variables and y is the dependent variable.

4.5.2 Multiple Linear Regression

The response surface is determined using multiple linear regression. The coefficients are estimated by the least squares method. Suppose that there are independent variables x_i and n observations, $(\mathrm{x_{i1}}, \mathrm{x_{i2}}, \cdots \mathrm{x_{ik}}, \mathrm{y_i})$, $(\mathrm{i} = 1,2, \cdots, \mathrm{n})$ and the model relating the independent variables to the dependent variable $\mathrm{y_i}$ is

$$\mathrm{y_i} = \mathrm{a_0} + \mathrm{a_1 x_{i1}} + \mathrm{a_2 x_{i2}} + \cdots \mathrm{a_k x_{ik}} + \epsilon_\mathrm{i},\ \mathrm{i} = 1,2, \cdots, \mathrm{n} \tag{4.13}$$

where $\mathrm{a_i}$ are the regression coefficients and ϵ_i are the random error terms. The model is a system of n equations that can be expressed in matrix notation as

$$\mathrm{y} = \mathrm{Xa} + \epsilon \tag{4.14}$$

where

$$\mathrm{y} = \begin{bmatrix} \mathrm{y_1} \\ \mathrm{y_2} \\ \vdots \\ \mathrm{y_n} \end{bmatrix} \quad \mathrm{X} = \begin{bmatrix} 1 & \mathrm{x_{11}} & \cdots & \mathrm{x_{1k}} \\ 1 & \mathrm{x_{21}} & & \mathrm{x_{2k}} \\ \vdots & \vdots & \ddots & \vdots \\ 1 & \mathrm{x_{n1}} & \cdots & \mathrm{x_{nk}} \end{bmatrix} \quad \beta = \begin{bmatrix} \mathrm{a_0} \\ \mathrm{a_1} \\ \vdots \\ \mathrm{a_k} \end{bmatrix} \quad \epsilon = \begin{bmatrix} \epsilon_1 \\ \epsilon_2 \\ \vdots \\ \epsilon_\mathrm{n} \end{bmatrix}$$

The least square function is

$$L = \sum_{\mathrm{i}=1}^{\mathrm{n}} \epsilon_\mathrm{i}^2 = \epsilon^\mathrm{T} \epsilon = (\mathrm{y} - \mathrm{Xa})^\mathrm{T} (\mathrm{y} - \mathrm{Xa}) \tag{4.15}$$

The least squares estimator $\hat{a}$ is the solution for a in the equations:

$$\frac{\partial L}{\partial a} = 0 \tag{4.16}$$

The resulting equations that must be solved are

$$X^T X\hat{a} = X^T y \tag{4.17}$$

By the inverse of $X^T X$, therefore the least squares estimate of a is

$$\hat{a} = (X^T X)^{-1} X^T y \tag{4.18}$$

4.5.3 Response Surface for Maximum Wall Deflection

Based on the 1120 hypothetical cases described in the previous section, the response surface method is used to obtain the explicit function for the wall deflection. The ranges of the variables are shown in Table 4.7. The regression equation for wall deflection takes the following form:

$$\delta_{h0} = a_0 + a_1 B + a_2 B^2 + a_3 T + a_4 T^2 + a_5 h + a_6 h^2 + a_7 \frac{c_u}{\sigma_v'} + a_8 \left(\frac{c_u}{\sigma_v'}\right)^2 + a_9 \frac{E_{50}}{c_u} + a_{10} \left(\frac{E_{50}}{c_u}\right)^2 + a_{11} \ln(EI/\gamma_w h_{avg}^4) + a_{12} \ln^2(EI/\gamma_w h_{avg}^4) + a_{13}\gamma + a_{14}\gamma^2 + a_{15} \ln(EI/\gamma_w h_{avg}^4) \cdot h \tag{4.19}$$

Table 4.7 Range of Variables

Soil parameter		Non-soil parameter	
c_u/σ_v'	0.2— 0.4	B (m)	$20 - 75$
E_{50}/c_u	$100 - 335$	T (m)	$25 - 83$
$\gamma(\mathrm{KN/m^2})$	$15 - 20$	h (m)	$8 - 29$
		$ln(EI/\gamma_w h_{avg}^4)$	$6.0 - 9.4$

The values of the coefficients are shown in Table 4.8.

Table 4.8 Response Surface Coefficient for δ_{h0}

a_0	1612.23	a_4	-0.0456	a_8	699.08	a_{12}	8.78
a_1	2.524	a_5	38.76	a_9	-0.881	a_{13}	-118.05
a_2	-0.0169	a_6	-0.256	a_{10}	0.00131	a_{14}	2.978
a_3	7.55	a_7	-1014.39	a_{11}	-119.04	a_{15}	-3.31

Figure 4.21 shows the plot of the maximum wall deflection values computed using Eq. (4.19) versus the FEM values for the 1120 hypothetical cases. Eq. (4.19) is shown to be a fairly accurate with a high coefficient of determination (R^2) of 0.88.

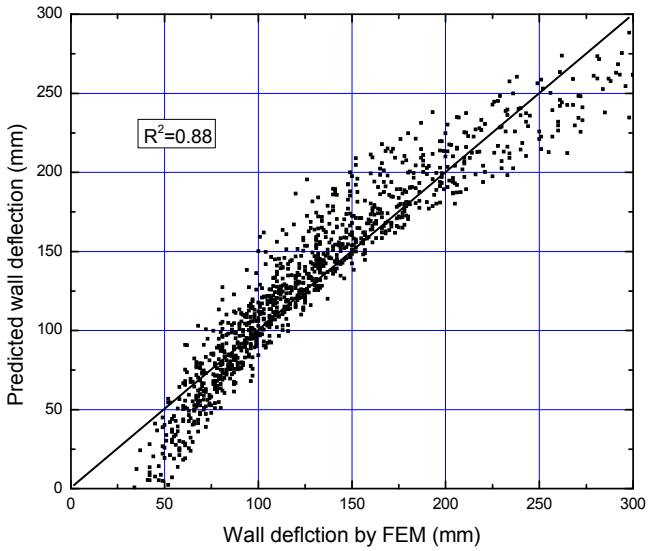

Figure 4.21 Predicted Maximum Wall Deflection versus Deflection by FEM

Corrections for the depth of the ground water table and strut stiffness can be considered using

$$\delta_{hm} = \mu_w \cdot \mu_s \cdot \delta_{h0} \quad (4.20)$$

where μ_w is the correction factor for water table (Figure 4.5), and μ_s is the correction for strut stiffness (Figure 4.4).

4.5.4 Validity of Response Surface for Maximum Wall Deflection

Eq. (4.20) was used for the seven back-analysis cases presented in Chapter 3, as well as additional two cases of Bugis MRT (Halim, 2008) and Ou et al. (2008). The results in Table 4.9 and Figure 4.22 that the predictions using Eq. (4.20) compares well with the measured results except for case 4 and 6, which involved very high preloads and lower wall stiffness, respectively. The average values of parameters of the cases excluding case 6 are presented in the last row of Table 4.9.

Table 4.9 Comparison of Predicted and Measured Maximum Wall Deflection Predictions

Cases	B	T	h	$\frac{c_u}{\sigma'_v}$	$\frac{E_{50}}{c_u}$	$ln(\frac{EI}{\gamma_w h_{avg}^4})$	γ	μ_w	μ_s	δ_{hm}	$\delta_{h,M}$
	m	m	m				kN/m^2			mm	mm
1. Farrer Park	21	22	17.5	0.285	150	7.3	17.3	0.8	1.02	75.0	53
2. TNEC	43	33	19.7	0.32	100	7.30	19	0.8	0.8	115.4	108
3. Kotoku	30	30	17	0.34	100	7.30	16	0.8	1	132.7	170
4. Lavender	23	18	16	0.26	100	7.96	17	0.8	1	69.3	32
5. Formosa	35	27	18.5	0.34	200	7.30	19	0.8	1.05	64.1	60
6. Rochor Complex	95	24	8.3	0.25	100	4.02	16	0.8	1	240.6	150
7. Syed Alwi	28	16	7.8	0.25	150	6.43	16	0.9	1	52.6	50
8. Bugis MRT	21	35	18	0.26	150	8.18	16.5	0.9	1	136.3	135
9. Ou et al. (2008)	42	20	9.31	0.25	150	6.24	17.6	0.95	1	94.3	105
Average Value	30	25	15.4	0.288	137	7.25	17.3	0.84	0.98	92.5	89.12

Notes: $\delta_{h,M}$ = measured maximum wall deflection

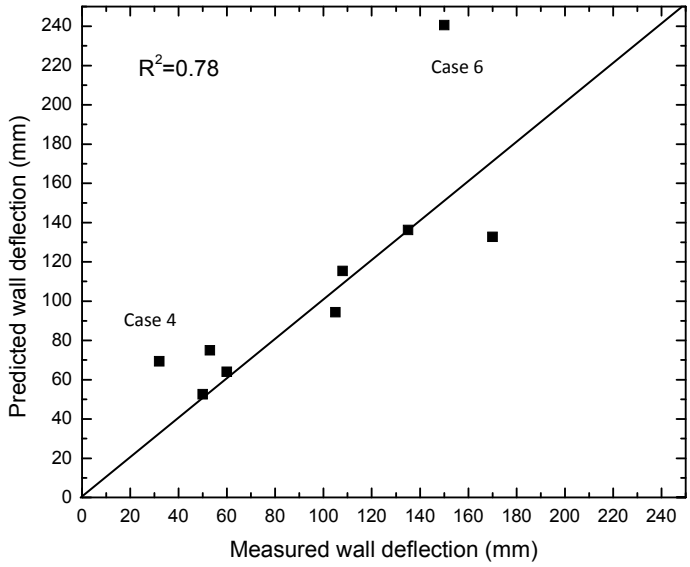

Figure 4.22 Predicted versus measured maximum wall deflection

4.6 Response Surface for Maximum Surface Settlement

Peck (1969), Clough and O'Rouke (1990), and Hsieh and Ou (1998) have developed several profiles to estimate the surface settlement induced by excavation. In their methods, the maximum surface settlement δ_{vm} is an important factor to construct the entire surface settlement profile. Hsieh and Ou (1998) and Kung et al. (2007b) proposed that δ_{vm} could be estimated from the relationship between δ_{hm} and δ_{vm}, which is expressed as:

$$\delta_{vm} = \mu_R \delta_{hm} \tag{4.21}$$

where μ_R = deformation ratio. The results of μ_R for over 120 hypothetical cases by FEM as shown in Figure 4.23, indicate that μ_R is concentrated in the range of $0.65 - 0.7$. Table 4.10 shows the μ_R values for the cases considered in Section 4.5.4 where the maximum settlement was reported with μ_R in the range of 0.66 to

1.04. The high μ_R for Bugis MRT is probably due to the soil consolidation. For simplicity, a slightly conservative μ_R is assumed to be 0.7 and the maximum surface settlement can be estimated as:

$$\delta_{vm} = 0.7\delta_{hm} \tag{4.22}$$

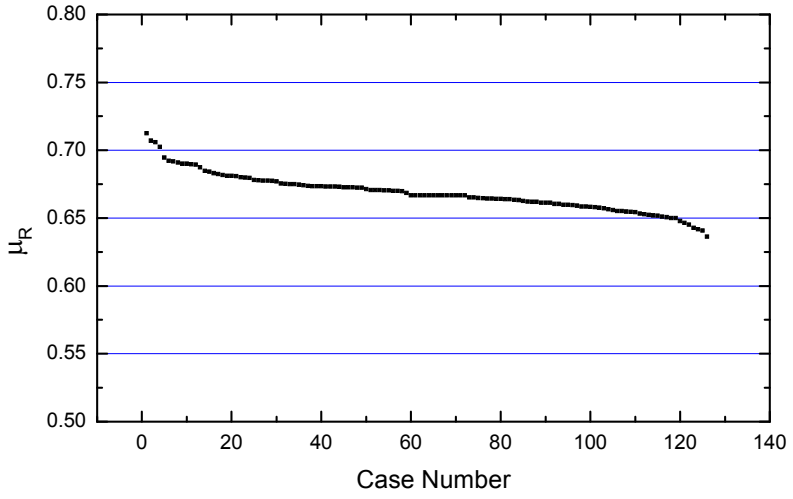

Figure 4.23 Plot of μ_R

Table 4.10 Prediction of Maximum Surface Settlement

Cases	$\delta_{hm,M}$ (mm)	$\delta_{vm,M}$ (mm)	$\delta_{vm,F}$ (mm)	$\delta_{vm,M}/(\delta_{hm,M}$ or $\delta_{vm,F})$
1. Farrer Park	53	—	40	0.75
2. TNEC	108	80	—	0.74
3. Kotoku	170	112	—	0.66
4. Laverder	32	—	27	0.84
5. Formosa	60	45	—	0.75
6. Rochor Complex	150	—	110	0.73
7. Syed Alwi	50	—	—	—
8. Bugis MRT	135	140	—	1.04
9. Ou et al,2008	105	—	—	—

Notes: $\delta_{vm,M}$= measured maximum surface settlement and $\delta_{vm,F}$= maximum surface settlement by FEM

For the case studies considered in Section 4.5.4, Figure 4.24 shows the plot of the maximum surface settlement predicted by Eq. (4.21) versus the "measured" results. For those cases where the measured maximum surface settlement was not reported, the FEM values (evaluated in Chapter 3) were used instead. There was good agreement between the predicted and "measured" results except for Bugis MRT with a high coefficient of determination (R^2) of 0.98.

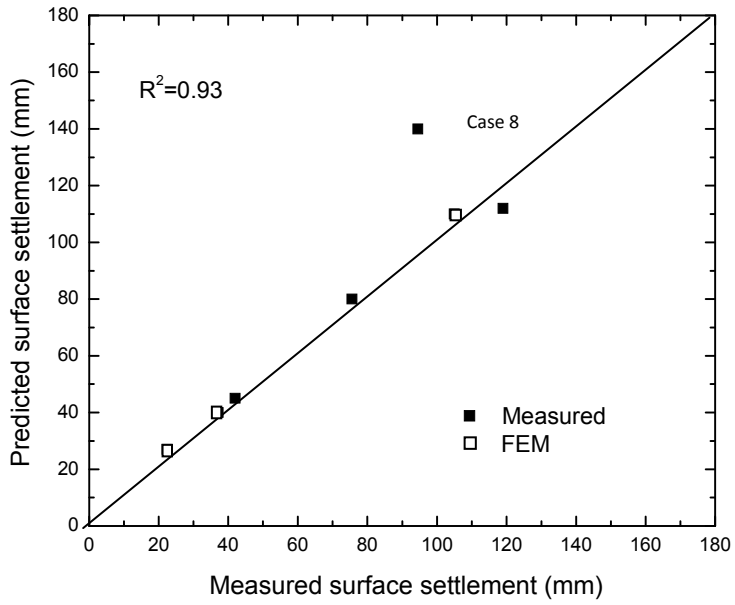

Figure 4.24 Predicted Maximum Surface Settlement versus Measured or FEM Settlement

4.7 Apparent Pressure Diagram (APD)

Arising from the previously described hypothetical cases, the magnitude of the strut forces which are expressed in the form of apparent pressure diagrams (APD) are presented in this section. The proposed APD to estimate the maximum strut forces is applicable for excavations with similar soil conditions to those considered in this study. Two case histories from the literature are used to validate this method.

4.7.1 Background

Terzaghi and Peck (1967) had developed various apparent pressure diagrams for different soils based on measured data from relatively flexible walls. There is some uncertainty as to whether these APDs can be used for excavations with diaphragm wall which are stiffer and widely used in last two decades. Chang and Wong (1996) had found that the Terzaghi and Peck (1967) APD for clay was unconservative and amended it to consider the effects of the thickness of the clay deposit.

4.7.2 Terzaghi-Peck Method

Terzaghi and Peck (1967) had developed the apparent pressure diagram shown in Figure 4.25 for excavations with flexible walls in soft to medium clays. The detailed information is described in Section 2.4. Figure 4.26 shows the variation of σ_{TP} is almost linear with depth of excavation for the cases in which $\gamma = 17\ \mathrm{kN/m^3}$, and undrained strength value is taken at middle depth.

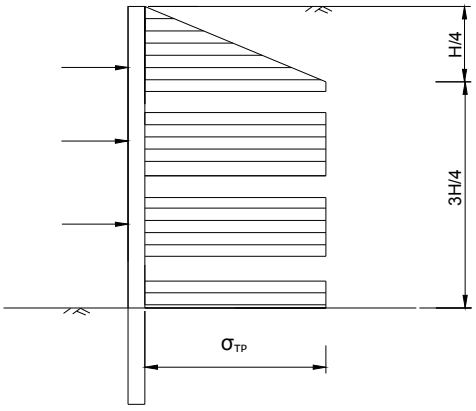

Figrue 4.25 Terzaghi-Peck Method for Soft Clay

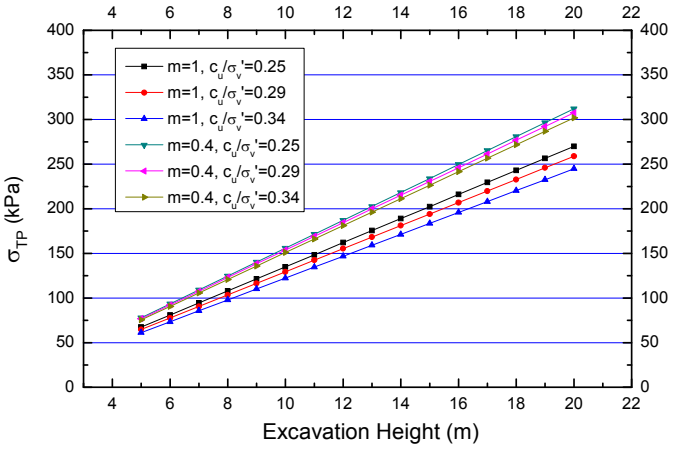

Figure 4.26 Plot of σ_{TP} versus H_e for $\gamma = 17\ \mathrm{kN/m^3}$

4.7.3 Factors Affecting APD

From the parametric study, the more critical and less critical factors that influence the maximum earth pressure have been identified and are presented in this section, in which the maximum earth pressure σ_{max} is defined as the maximum force on the strut divided by the tributary area as used in the Terzaghi & Peck method, and the normalized depth on the vertical axis refers to the depth below ground surface divided by the final excavation depth.

4.7.3.1 Effect of Clay Thickness on σ_{max}

The analyses indicate that the soft clay thickness T is the most important factor that affects the maximum earth pressure. This is demonstrated through one set of cases with parameters $B = 30\ \mathrm{m}$, $H_e = 20\ \mathrm{m}, c_u/\sigma_v' = 0.29$, $E_{50}/c_u = 200$, $d = 0.9\ \mathrm{m}$, $\gamma = 17\ \mathrm{kN/m^3}$. The results in Figure 4.27(a) show that the Terzaghi & Peck APD overestimates maximum earth pressure for cases with $T \leq 25m$. The clay thickness has a significantly effect on the distribution and magnitude of the strut loads. When $T \leq 25\ \mathrm{m}$, the maximum pressure occurs in the top half of the

excavation while for $T \geq 40$ m, it is the opposite. For $T = 25{\sim}40$ m, the shape of the maximum pressure diagram agrees with Terzaghi and Peck (1967). The maximum pressure plotted with different clay thickness as shown in Figure 4.27(b), indicate that the pressure almost linearly increases with the clay thickness.

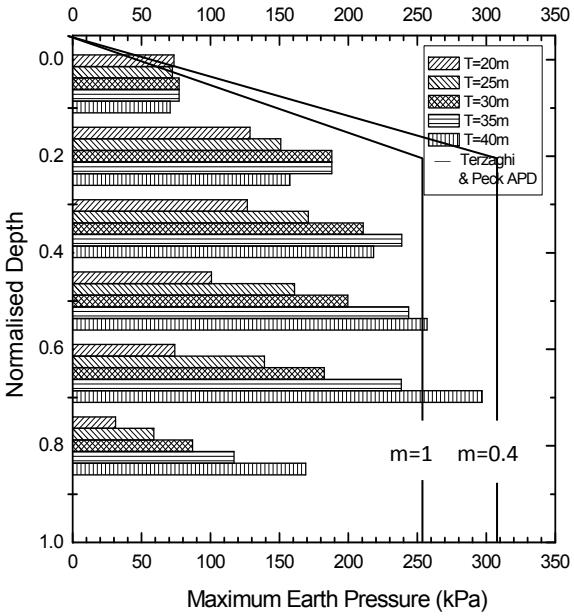

(a)

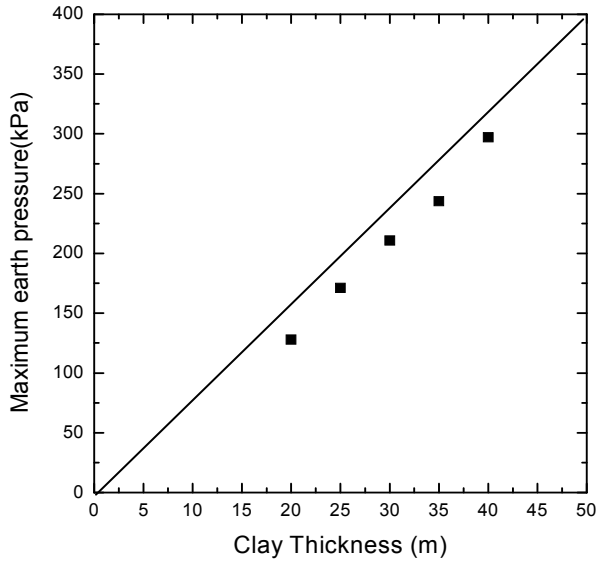

(b)

Figure 4.27 Effect of Clay Depth on Apparent Pressure (a) Apparent Pressure Diagram (b) Relationship between Clay Thickness and Maximum Earth Pressure

4.7.3.2 Effects of c_u/σ_v' and EI on σ_{max}

The influence of the soil strength ratio c_u/σ_v' and wall stiffness EI on the earth pressure for the cases with $B = 30$ m, $H_e = 20$ m, $E_{50}/c_u = 200, d = 0.9$ m, $\gamma = 17$ kN/m^3, $T = 30$ m and for cases with $B = 30$ m, $H_e = 20$ m, $c_u/\sigma_v' = 0.29$, $E_{50}/c_u = 200, \gamma = 17$ kN/m^3, $T = 30$ m are shown in Figure 4.28. Figure 4.28(a) shows the different values of c_u/σ_v' influences the maximum pressure in the top half which means the effect is more distinct for shallower excavation depths while for deeper excavations the influence of c_u/σ_v' is small. Terzaghi & Peck APD for $c_u/\sigma_v' = 0.25, 0.29, 0.34$ with m = 1 and $c_u/\sigma_v' = 0.29$ with m = 0.4 are shown in Figure 4.28(a). Figure 4.28(b) shows the stiffer the wall, the less is the maximum earth pressure. However, the increase of wall stiffness does not significantly decrease the maximum earth pressure.

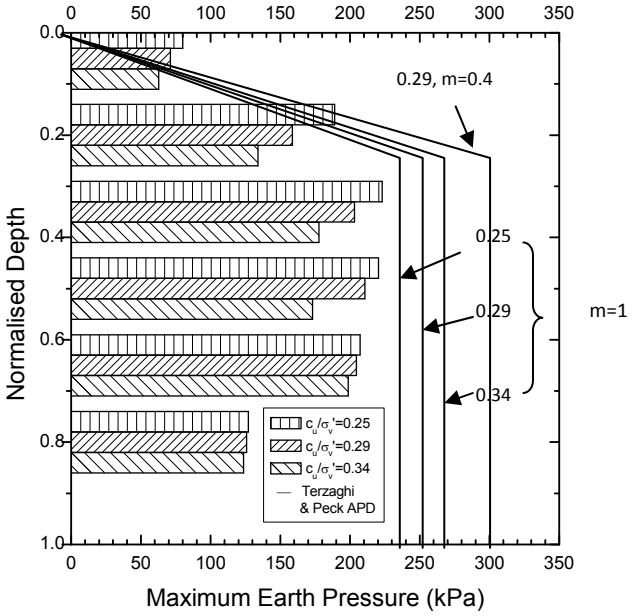

(a)

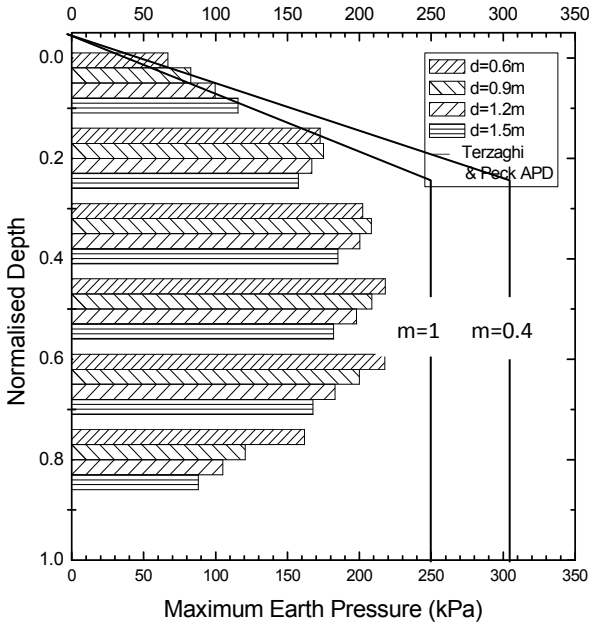

(b)

Figure 4.28 Apparent Pressure Diagram Plot Showing

(a) the Effect of Soil Strength Ratio (b) the Effect of Wall Stiffness

4.7.3.3 Effect of B, γ, and E_{50}/c_u on σ_{max}

To illustrate the influence of the excavation width B, soil unit weight γ and soil stiffness E_{50}/c_u, Figure 4.29 shows the cases with $H_e = 20$ m, $c_u/\sigma_v' = 0.29$, $E_{50}/c_u = 200$, $d = 0.9$ m, $\gamma = 17$ kN/m^3, $T = 30$ m, cases with $B = 30$ m, $H_e = 20$ m, $c_u/\sigma_v' = 0.29$, $E_{50}/c_u = 200$, $d = 0.9$ m, $T = 30$ m and for cases with $B = 30$ m, $H_e = 20$ m, $c_u/\sigma_v' = 0.29$, $d = 0.9$ m, $\gamma = 15$ kN/m^3, $T = 30$ m, respectively. The results show the factors do not affect the maximum earth pressure significantly although the former two parameters can influence the distribution of apparent pressure due to the different basal heave factor safety. This will be discussed later.

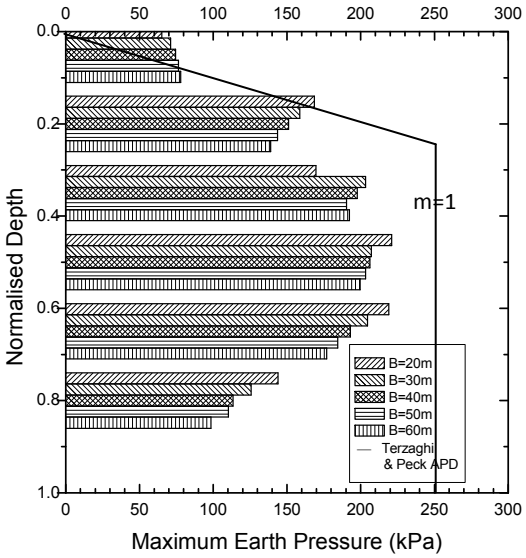

(a)

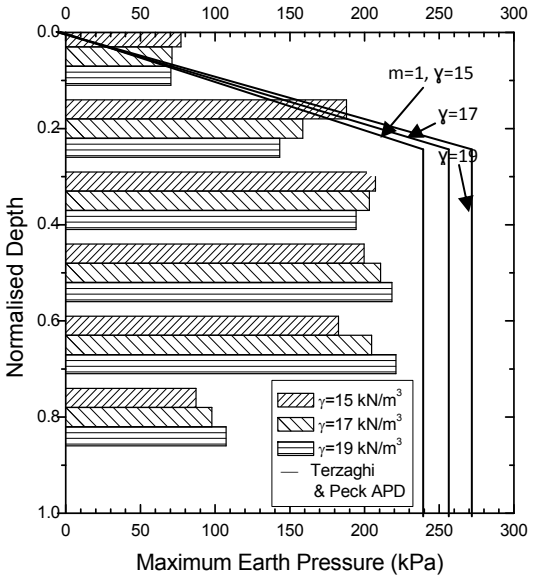

(b)

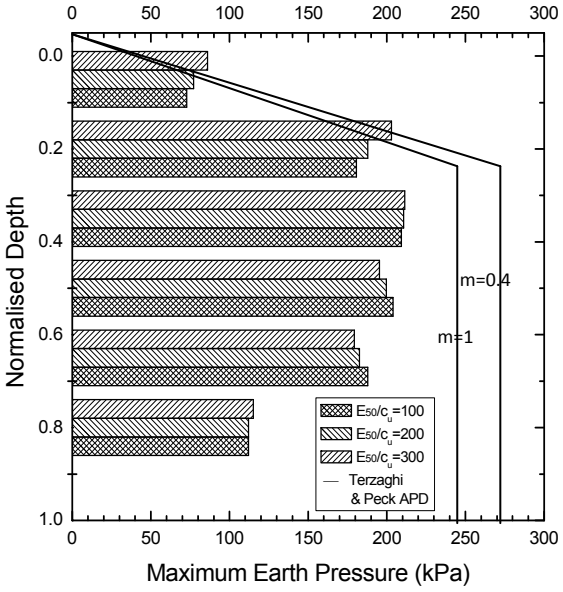

(c)

Figure 4.29 Apparent Pressure Diagram Plot Showing (a) the Effect of Excavation Width (b) the Effect of Soil Unit Weight (c) the Effect of Soil Stiffness

4.7.3.4 Effect of Strut Properties on σ_{max}

To illustrate the influence of the strut stiffness and preloading on the maximum earth pressure, Figure 4.30 shows the cases for $B = 30$ m, $H_e = 20$ m, $c_u/\sigma'_v = 0.34$, $E_{50}/c_u = 100$, $d = 0.9$ m, $\gamma = 17$ kN/m^3, $T = 30$ m and cases for $c_u/\sigma'_v = 0.29$, $E_{50}/c_u = 200$, $d = 0.9$ m, $\gamma = 17$ kN/m^3, $T = 30$ m, respectively. The strut stiffness $k'_{ss} = 1.0 \times 10^6$ kN/m represents a normal steel beam with stiffness $k_{ss} = EA = 4.0 \times 10^6$ kN as strut, and with 4 m horizontal spacing. Figure 4.30(a) shows different strut stiffness can change the distribution of the maximum earth pressure but does not significantly change the magnitude of the maximum earth pressure. Preloading is often applied to reduce the wall deflection. Figure 4.30(b) compares three cases where the applied preloadings are approximate 33%, 66%, and 100% of the design loads. The plot shows the earth pressure increases sharply when the preloading is 66% and 100% of the design load while the change is small in the case of 33% preloading. Hence high preloading should be used with care as it could lead to strut failure.

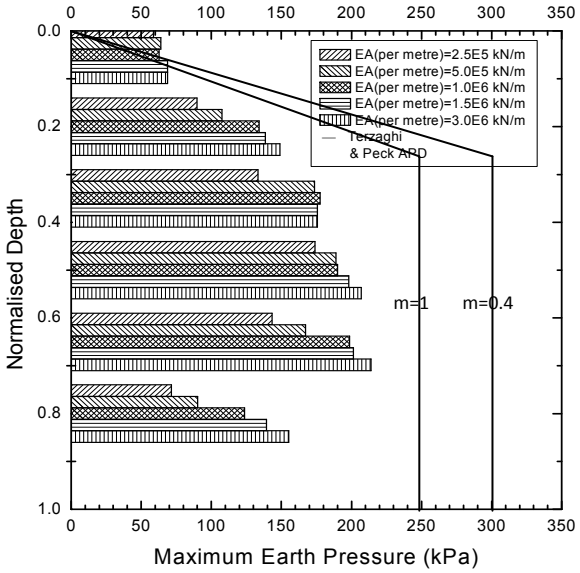

(a)

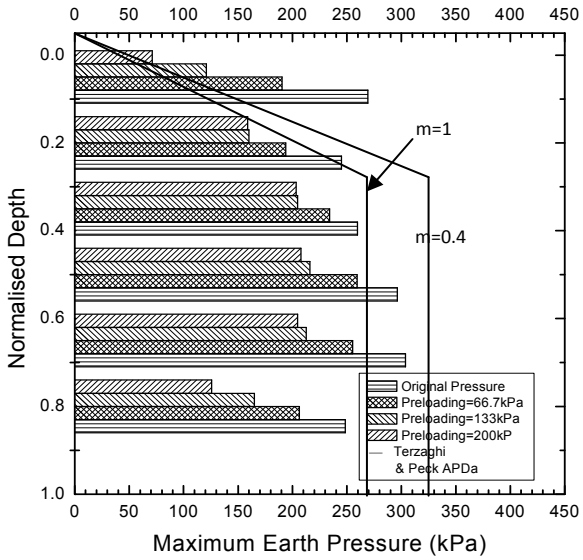

(b)

Figure 4.30Apparent Pressure Diagram Plot Showing (a) the Effect of Strut Stiffness (b) the Effect of Preloading

4.7.3.5 Effect of Strength of Stiff Clay on σ_{max}

This section illustrates that basal heave factor of safety critically influences the maximum earth pressure especially its distribution. This is demonstrated through the cases with $B = 30$ m, $H_e = 20$ m, $c_u/\sigma_v' = 0.29$, $E_{50}/c_u = 200$, $d = 0.9$ m, $\gamma = 17\,\mathrm{kN/m^3}$, $T = 30$ m and cases with $B = 30$ m, $H_e = 20$ m, $c_u/\sigma_v' = 0.29$, $E_{50}/c_u = 200$, $d = 0.9$ m, $\gamma = 17\ \mathrm{kN/m^3}$, $T = 20$ m , which have different clay thickness T. Through changing the soil strength of the bottom stiff clay $c_{u,stiff}$, different ratios of $\mu_{c_u} = c_{u,stiff}/c_{u,soft}$ are presented in Table 4.11.

Table 4.11 μ_{c_u} Values for the Different Cases Considered

$c_{u,stiff}$ (kPa)	μ_{c_u}	
	$T = 30$m	$T = 20$m
80	2.6	4
100	3.3	5
200	6.6	10
300	10	15
400	13.3	20
500	16.6	25

Just as the basal heave factor of safety significantly affects the wall deflection (Mana and Clough, 1981), the results in Figure 4.32 show the maximum earth pressures in the lower struts increase sharply when μ_{c_u} is less than 3 while the influence is minimal when μ_{c_u} exceeds 10. The ratio μ_{stiff} is defined as the maximum earth pressure divided by the maximum earth pressure for the case with $c_{u,stiff} = 500$ kPa. Hence more attention should be given to the pressures of the lower struts in excavations where μ_{c_u} is low.

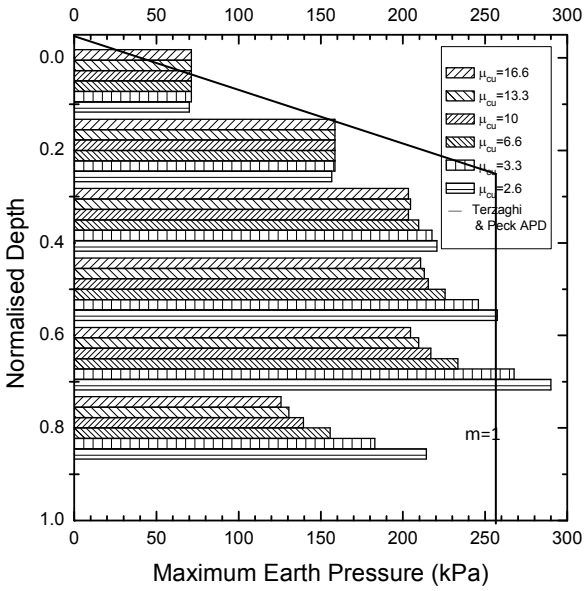

(a)

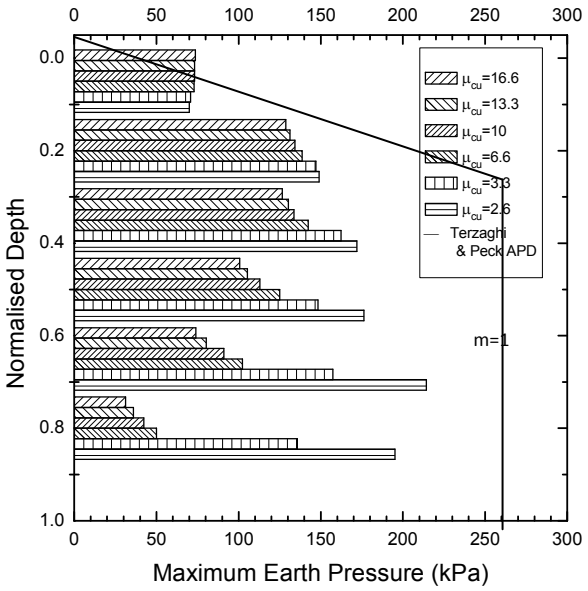

(b)

Figure 4.31 Effect of Strength of Stiff Clay (a) $T = 30$ m (b) $T = 20$ m

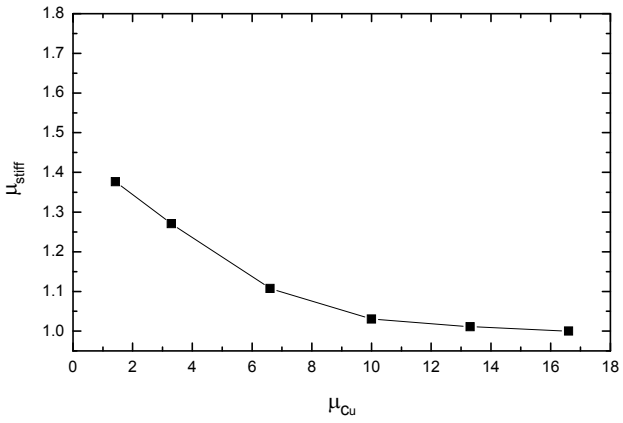

(a)

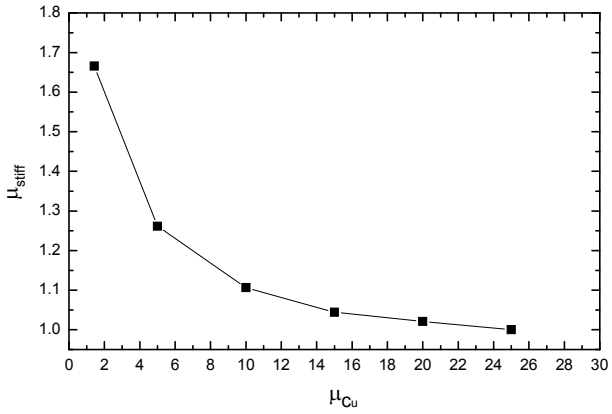

(b)

Figure 4.32 μ_{stiff} for Different μ_{c_u} (a) $T = 30$ m (b) $T = 20$ m

4.7.3.6 Effect of an Intermediate Stiff Clay Layer on $\sigma_{\max}$

Generally, the load on a strut is induced by the increasing wall deflection as a result of soil excavated below the strut (i.e. next stage of excavation). Hence, the strut force is significantly influenced by the properties of the soil directly beneath the strut. Effect is shown for cases with $B = 30$ m, $H_e = 20$ m, $c_u/\sigma'_v = 0.29$,

$E_{50}/c_u = 200,\ d = 0.9$ m, $\gamma = 17$ kN/m^3, $T = 30$ m which have an intermediate a 3m-thick stiff clay layer ($c_u = 150$ kPa, $E_u = 300c_u$) at depths of 2 m to 5 m (Profile B) and depths of 11 m to 14 m (Profile C) in Figure 4.33. Figure 4.34(a) shows there is not distinct influence on earth pressure for 'Profile B'. However, Figure 4.33(b) shows the strut force increases sharply in the fourth level at 10 m for 'Profile C' as the reason of abrupt increment of wall deflection (stiff clay is excavated) but other strut loads decrease compared with 'Profile A'.

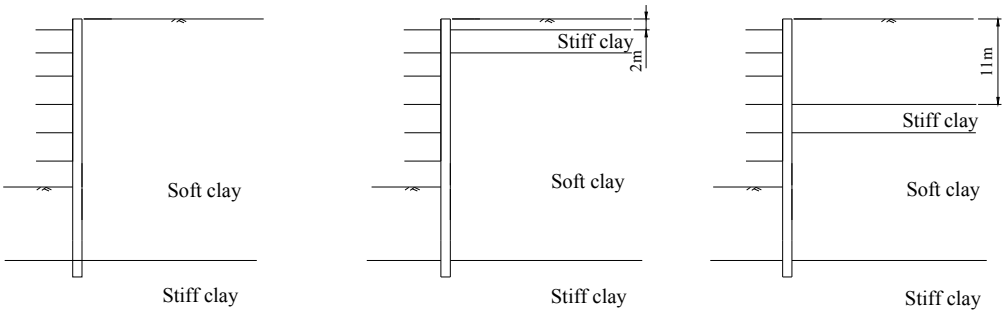

Soil Profile A Soil Profile B Soil Profile C

Figure 4.33 Plot of Soil Profiles

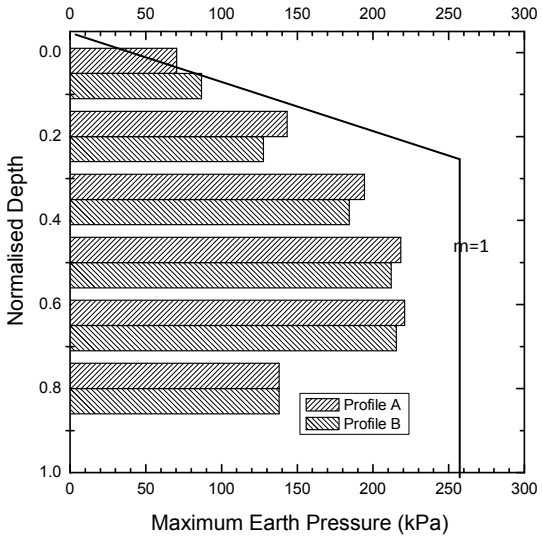

Figure 4.34 (a) Effect of 'Soil Profile B' on Apparent Pressure

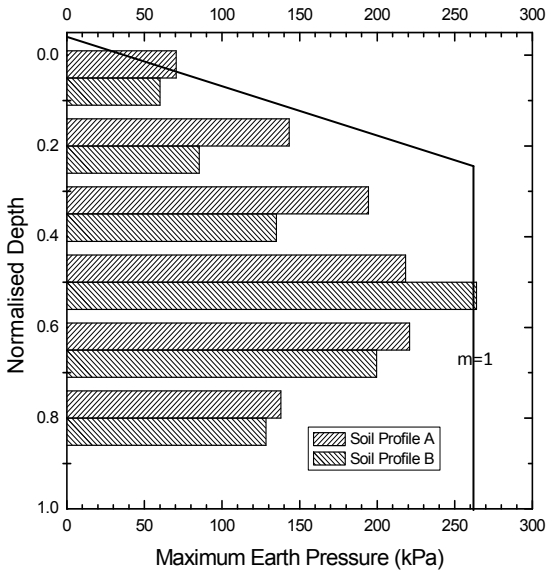

Figure 4.34 (b) Effect of 'Soil Profile C' on Apparent Pressure

4.7.4 The Approximate Estimation of APD

Based on the analyses described in the previous Sections, the simplified APD

shown in Figure 4.35 is proposed for soft clays supported by diaphragm walls. An approximate and conservative formula value to determine the maximum apparent pressure σ_{APD} is

$$\sigma_{APD} = (0.2T + 6)T\ tan(\frac{\pi}{4} - \frac{\varphi}{2}) \tag{4.23}$$

where σ_{APD} is the maximum apparent pressure, T is depth of the soft clay layer, which can be interpreted as the distance from the ground level to the level where the wall is restrained, and φ is the effective friction angle of soft clay layer that can be derived from Eq. (3.3). The simplified APD account for the two most critical factors that influence the maximum pressure, namely T and soil shear strength. The charts are not applicable for excavation with high preloading on the struts.

Figure 4.36 which shows the plot for all the cases considered in this study indicates that the predictions based on Figure 4.35 are slightly conservative. Alternatively, σ_{APD} can be determined from the chart in Figure 4.37.

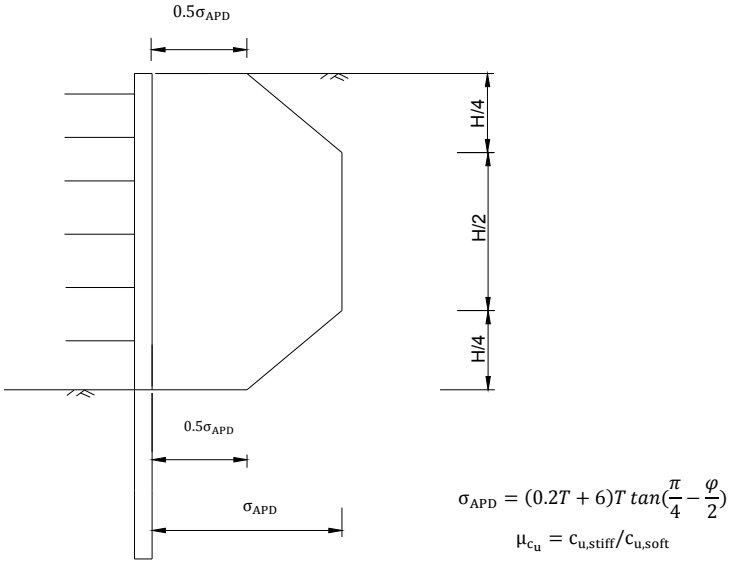

(a)

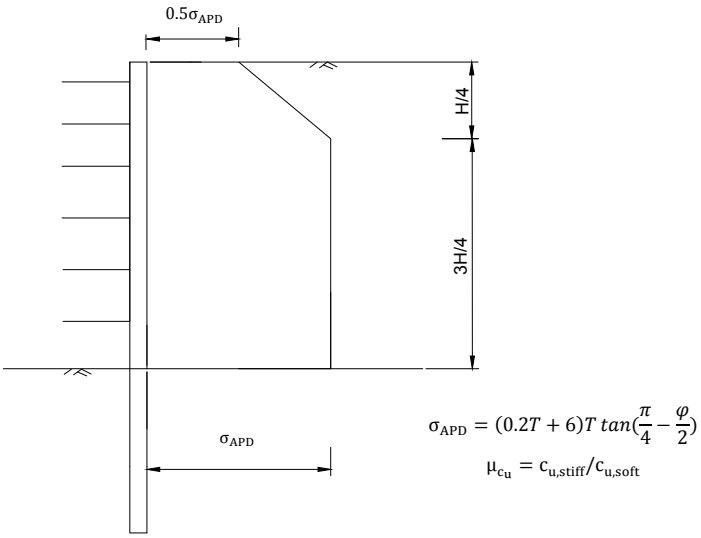

(b)

Figure 4.35 APD for (a) $\mu_{c_u} \geq 6$ (b) $\mu_{c_u} < 6$

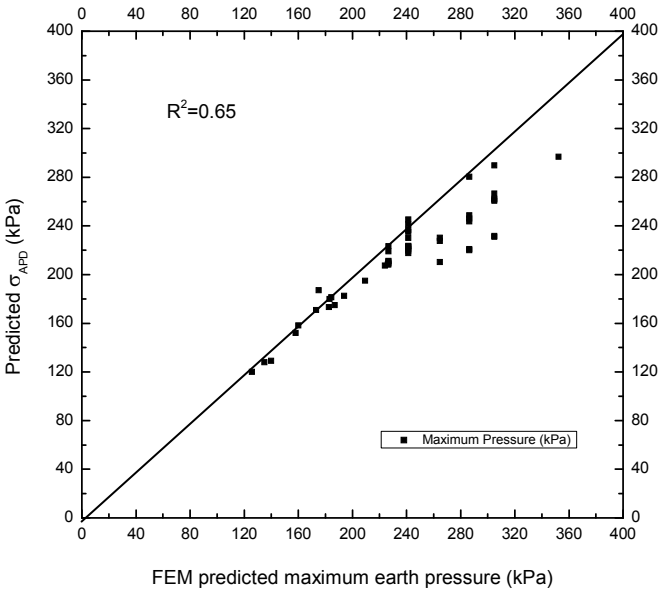

Figure 4.36 FEM Data Validated

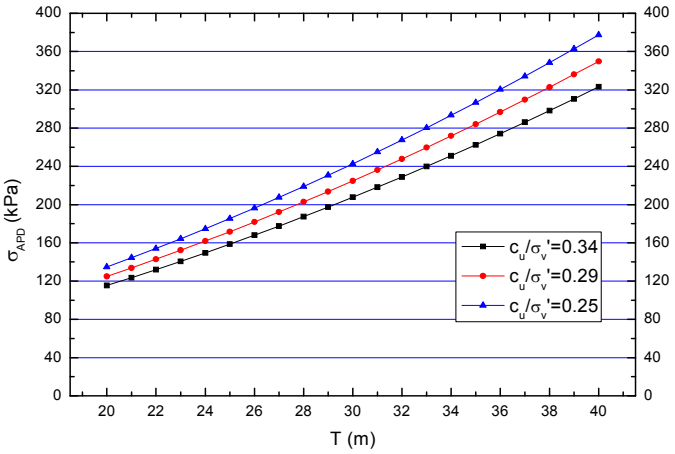

Figure 4.37 Chart for Estimating Maximum Apparent Pressure

Although the charts in Figure 4.36 and 4.37 are based on excavation depth $H_e = 20$ m, the application range may be extended to H_e in the range of 10 m to 20 m. A reduction factor μ_{APD} is introduced to consider the cases with different excavation depth H_e.

$$\mu_{\mathrm{APD}} = \frac{2}{H_e/20+20/H_e} \tag{4.24}$$

A chart for the reduction factor is shown in Figure 4.38. The two charts can be combined to estimate the maximum apparent pressure for cases with different excavation depths.

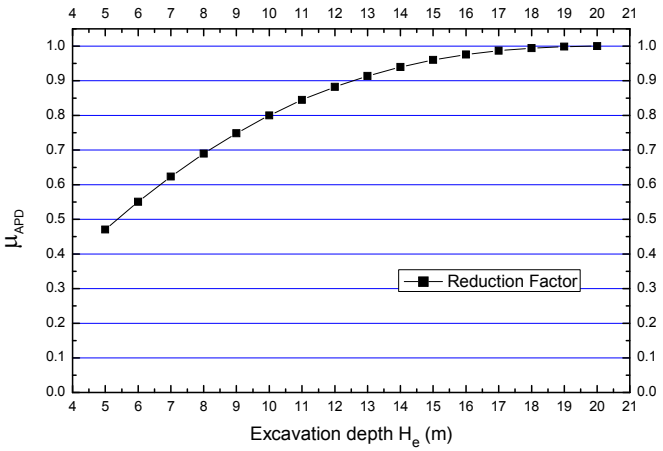

Figure 4.38 Chart for Estimating Reduction Factor

4.7.5 Validation from Measured Case Histories

4.7.5.1 TNEC Project

This case was reported by Ou et al. (1998) in Taipei. More detailed description is presented in Chapter 3. The top-down construction method was used. The cross-section of the project is shown in Figure 4.48. The 35 m long diaphragm wall penetrated into the medium dense silty sand. The distance from ground level to the soft clay depth is 33 m. Since the preloading did not exceed 50% of the measured value, the chart in this study can be used. The APD by this proposed method is plotted in Figure 4.39(b) where the maximum earth pressure is approximately 250 kPa. Ou et al. (1998) reported the measured pressure in the lowest strut was 245.8 kPa while the value estimated by Terzaghi & Peck is 118 kPa and 222 kPa when the average shear strength of Silty Clay is assumed to be 58.6 kPa and 34.5 kPa, respectively.

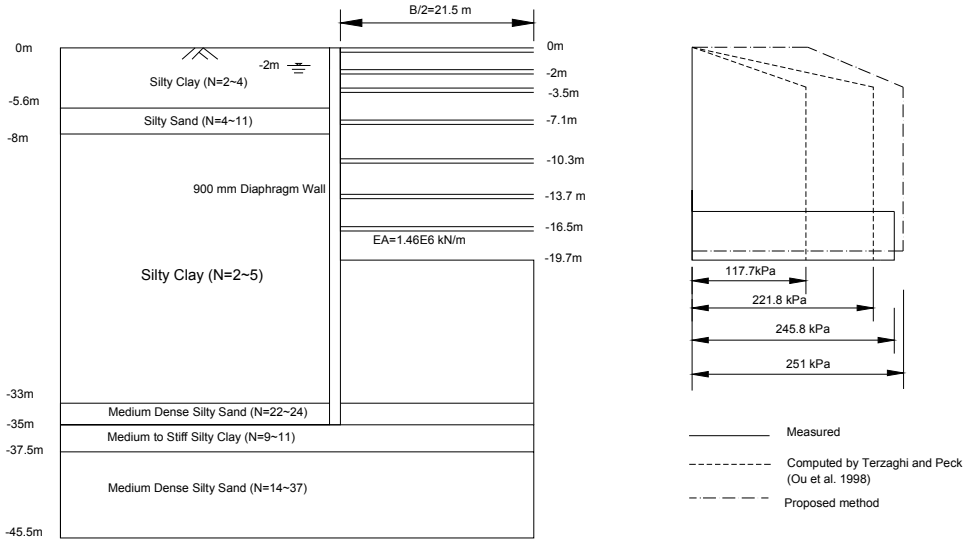

(a) (b)

Figure 4.39 (a) Profile of TNEC Project (Ou et al., 1998)

(b) Apparent Pressure Diagram

4.7.5.2 BL 12 Underground Station

The case is a well-instrumented deep excavation in Taiwan (Hsiung et al., 1999), the BL 12 underground station on the Nankang Line of Taipei Mass Rapid Transit System. The 16 m deep excavation was retained by 33 m diaphragm wall, and was internally braced by seven levels of struts. The soil profile is shown in Figure 4.40, which indicates the thickness of soft clay— Sung-Shan formation layer is 30 m. The measured pressures in District 2, 6 and 14 are shown in Figure 4.41, where the maximum pressure is 160 kPa. Assuming $c_u/\sigma_v' = 0.34$ and $T = 30$ m, the predicted maximum earth pressure is 203 kPa. The predicted APD is shown in Figure 4.41, and the other three plotted diagrams are based on the CIRIA distributed prop load diagrams by Twine and Roscoe (1997) (Hsiung et al., 1999).

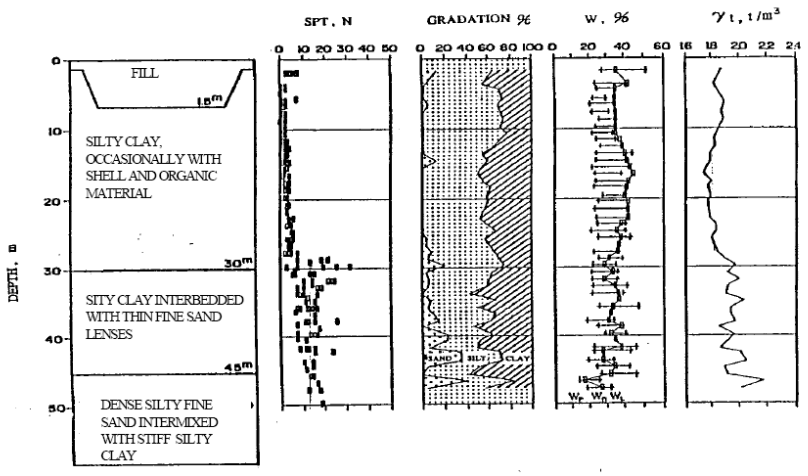

Figure 4.40 Soil Profile of BL 12 Underground Station (Hsiung et al., 1999)

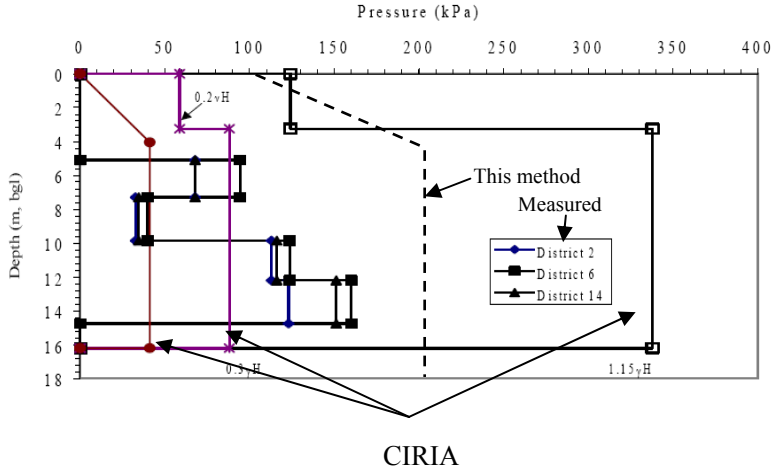

Figure 4.41 APD for BL 12 Underground Station (Hsiung et al., 1999)

4.8 Summary

A series of parametric studies for deep excavations have been carried out to obtain insights into the behavior of excavations in soft clays. Based on these analyses, simplified methods have been proposed.

(a) Response surfaces for maximum wall deflection and maximum surface settlement have been proposed. The ratio of wall deflection and surface settlement can be assumed to be 0.7.

(b) A simple method to predict wall deflection path is presented considering the effect of hard stratum.

(c) A method for estimating the APD is proposed for excavations with diaphragm walls in soft clay.

Chapter 5

RELIABILITY ANALYSIS

5.1 Introduction

In a deterministic approach, the serviceability of excavations and the adjacent buildings are evaluated by whether the "predicted" or designed factors such as basal heave, strut force, wall deflection and ground movement are less than the specified tolerable limits. Generally, the factor of safety is always applied to ensure the safety of the excavation performance. However, many uncertainties exist in the calculation of the safety factors and this approach fails to reflect the degree of uncertainty. The reliability analysis is desirable to evaluate the safety of the excavation and the adjacent buildings. Goh and Kulhawy (2005), Hsiao et al. (2008) and Goh et al. (2008) have provided methods to assess the reliability of wall performance, ground settlement and basal heave, respectively.

The wall deflection and ground movement are the two most critical factors that affect the performance of adjacent structures. Control of excavation deformation serves to protect the adjacent facilities and prevent the collapse of the excavation system. The adoption of limiting displacements for wall and ground surface varies according to the surrounding environment of the excavation and the relative importance of the project. Different criteria are available for different projects. The limiting wall deflection is typically taken to be a percentage of the excavation height. The limiting surface settlement depends on the requirement of the differential settlement of adjacent buildings and the settlement of facilities and is taken to be a percentage of the excavation height as well in this Chapter.

5.2 Reliability Analysis

Based on analyses in Chapter 4, the response surfaces for wall deflection and surface settlement were determined. The response surface provides an explicit function involving soil variables and other variables to predict the performance of the movements associated with excavation. There are many reliability analysis methods available to assess the probability of "failure" (Schweckendiek, 2006). The most widely used method – 'Hasofer-Lind' method is used here to conduct the reliability analysis. The method is readily coupled with a Excel spreadsheet, as described by Low and Tang (1997) and Phoon (2004).

5.3 Performance Function

The performance functions of wall deflection and surface settlement include two basic variables: the maximum wall deflection (or the maximum settlement) and the limiting (tolerable) wall deflection (or limiting surface settlement), which in simplistic term can be described as *load* and *resistance*, respectively. The reliability analysis is conducted to assess the probability of the load exceeding the resistance. So the concept of 'reliability' and 'failure probability' herein is the probability of the wall deflection and the surface settlement exceeding the limiting value.

As described in Chapter 4, the regression equation for the maximum wall deflection response surface derived from parametric studies takes the following form:

$$\delta_{h0} = a_0 + a_1 B + a_2 B^2 + a_3 T + a_4 T^2 + a_5 h + a_6 h^2 + a_7 \frac{c_u}{\sigma'} + a_8 \left(\frac{c_u}{\sigma'}\right)^2 + a_9 \frac{E_{50}}{c_u} + a_{10} \left(\frac{E_{50}}{c_u}\right)^2 + a_{11} \ln(EI/\gamma_w h_{avg}^4) + a_{12} \ln^2(EI/\gamma_w h_{avg}^4) + a_{13}\gamma + a_{14}\gamma^2 + a_{15} \ln(EI/\gamma_w h_{avg}^4) \cdot h \quad (4.19)$$

where the coefficients are listed in Table 4.8. The maximum wall deflection and surface settlement are then calculated using

$$\delta_{hm} = \mu_w \cdot \mu_s \cdot \delta_{h0} \quad (4.20)$$

$$\delta_{vm} = 0.7\delta_{hm} \quad (4.22)$$

If the limiting wall deflection $\delta_{h,lim}$ is specified as 0.5% or 1% of excavation height, then

$$\delta_{h,lim} = \lambda_h H_e = 0.5\% \text{ or } 1\% \cdot H_e \quad (5.1)$$

where λ_h is the percentage of the excavation height for wall deflection. And if 1/300 or 1/500 is used as the 'Angular Distortion δ/L ' (Bjerrum, 1963; Boone, 1996) (where δ is the differential settlement and L is the length of the foundation), the limiting maximum surface settlement is:

$$\delta_{v,lim} = \frac{\delta}{L} \times 1.5H_e = \lambda_v H_e = 0.5\% \text{ or } 0.3\% \cdot H_e \quad (5.2)$$

where λ_v is the percentage of the excavation height for surface settlement.

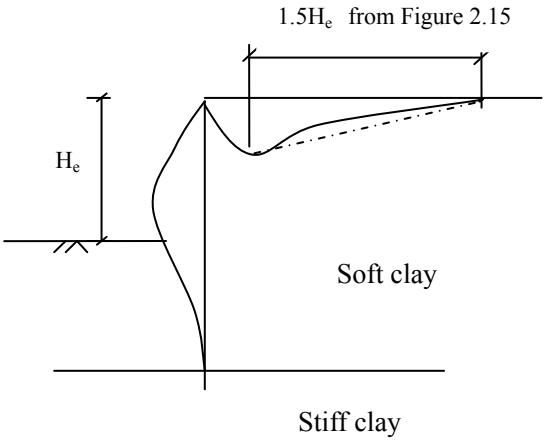

Figure 5.1 Settlement Profile (Hsieh and Ou, 1998; Kung, et al., 2007b)

So the limit state function (LSF) can be expressed as

$$g(x) = \delta_{h,lim} - \delta_{hm} \quad (5.3\ a)$$

$$g(x) = \delta_{v,lim} - \delta_{vm} \quad (5.3\ b)$$

5.4 Mean and COV of Variables

There are seven variables in Eq. (4.19), of which three are soil variables and four are nonsoil variables. The factors μ_w and μ_s are also nonsoil variables that influence the limit state surface. Due to its natural variability and inconsistent testing methods, the soil variables can have large variations. Duncan (2000) suggested the coefficient of variation (COV) of soil variables could be estimated from the published documents for example by Harr (1984), Kulhawy (1992), or Duncan (2000). Unlike soil variables, the nonsoil variables have smaller vibrations. In this study, the coefficients of variation (COVs) of nonsoil variables are assumed to be 0.05.

For any project, the typical reliability analysis consists of the following steps:

1. Determine the mean values and coefficient of variation (COVs) for the variables in the response surfaces for wall deflection and surface settlement (Table 5.1). This is further described in Section 5.4. For the three soil variables γ, c_u/σ'_v and E_{50}/c_u, the soil unit weight γ is taken as the weighted value of the layers overlying the stiff clay. The soil strength ratio c_u/σ'_v is an approximate value which is investigated from the site or based on published literature. Based on the case studies conducted in Chapter 3, the stiffness ratio E_{50}/c_u is mostly concentrated in the range of 100~150. The COV of soil variables can be estimated from Duncan (2000).
2. Calculate the maximum wall deflection δ_{hm} and maximum ground settlement δ_{vm} using the response surfaces (Eq. 4.20 and Eq. 4.22). Define the limiting

wall deflection $\delta_{h,lim}$ and surface settlement $\delta_{v,lim}$.

3. Define the performance function as Eq. 5.3 (a) and Eq. 5.3 (b).
4. Carry out reliability analysis using FORM to obtain the reliability index β (Hasofer and Lind, 1974) and the probability of failure P_f using the spreadsheet function (Low and Tang, 1997).

Table 5.1 COV of Variables

Soil variable (Duncan, 2000)		Non-soil variable	
c_u/σ_v'	5— 15%	B(m)	5%
E_{50}/c_u	Not specified	T(m)	5%
$\gamma(kN/m^3)$	3— 7%	h(m)	5%
		$ln(EI/\gamma_w h_{avg}^4)$	1.9%
		μ_w	5%
		μ_s	5%

5.5 Example Application

The process of reliability analysis for wall deflection and surface settlement is illustrated by two case histories.

5.5.1 Farrer Park — Kandang Kerbau (Wall deflection)

5.5.1.1 Overview

Details for the case are described in Section 3.3.4. The assumed mean value and COV of the variables are listed in Table 5.2. The thick and dominant layer is the Lower Marine Clay. The secondary layers are the Upper Marine Clay and the Fluvial Clay. The weighted c_u/σ_v' value from these three layers is used. The soil

unit weight γ is obtained from the weighted γ for all the soft layers above the Old Alluvium (OA). Since there is no data available for COV of E_{50}/c_u, it is important to conduct sensitivity study of the soil variables. In this study, the uncorrelated relationship between all the variables, as well as the correlation between c_u/σ_v' and E_{50}/c_u are considered. The weighted c_u/σ_v' and E_{50}/c_u are calculated below:

$$c_u/\sigma_v' = \frac{0.26\times3.5+0.27\times2.5+0.3\times7.5}{3.5+2.5+7.5} = 0.285 \tag{5.4}$$

$$\gamma = \frac{19\times8.5+16\times3.5+17\times2.5+16\times7.5}{8.5+3.5+2.5+7.5} = 17.3\ \text{kN/m}^3 \tag{5.5}$$

The predicted maximum wall deflection and maximum surface settlement are 75 mm and 52.5 mm, respectively. The limiting wall deflection is 87.5 mm or 175 mm when the limitation of 0.5% or 1% of the excavation height is adopted. The limiting surface settlement is 87.5 mm or 52.5 mm if the limitation surface settlement is taken as 0.5% or 0.3% of the excavation height, respectively.

Table 5.2 Mean Value and COV for Farrer Park

Soil Variable				Non-soil Variable		
Variable	Mean	COV (Duncan, 2000)	COV Adopted in Case	Variable	Mean	COV Adopted in Case
c_u/σ_v'	0.285	5—15%	15%	B(m)	21	5%
E_{50}/c_u	150	Varied	15%	T(m)	22	5%
$\gamma(kN/m^3)$	17.3	3—7%	7%	h(m)	17.5	5%
				$ln(EI/\gamma_w h_{avg}^4)$	7.3	1.9%
				μ_w	0.8	5%
				μ_s	1.02	5%

The reliability analysis of wall deflection for normally distributed and uncorrelated variables is shown in Figures 5.2. The step-by-step procedure is shown in the following:

1. Input mean values (D5:D20) to calculate the predicted maximum wall deflection (F21). Modify with μ_w (D22) and μ_s (D23) to obtain δ_{hm} (F24).
2. Input mean value in 'x value' (I5:I13) and 'mean' (J5:J13), and transpose 'x value' as $[X'^{T}]$ (C31:R31) which coincides with the coefficient column (E5:E20). Input COV in (L5:L13) and obtain σ in (K5:K13), as well as the column [nx] in (M5:M13) which contains the equation $(x_i - \mu_i)/\sigma_i$. Transpose (built-in spreadsheet function) [nx] in (C28:K28).
3. Input element matrix R, inverse (built-in spreadsheet function) R to obtian $[R]^{-1}$.
4. Invoke 'Solver' in Excel spreadsheet. Minimize reliability index $\beta = \min_{X \in F} \sqrt{[nx]^T [R]^{-1} [nx]}$ in (J16). Change 'x value' in (I5:I13). Constraint $g(x) = \delta_{h,lim} - \delta_{hm}$ in (J25), where $\delta_{h,lim} = 1.0\%$ or $0.5\% \cdot H_e$ and $\delta = (I12) \cdot (I13) \cdot [X'^{T}][E5:E20]$.
5. Obtain β and $P_f = 1 - \text{NORMSDIST}(\beta)$, where NORMSDIST is the spreadsheet function returning the standard normal cumulative distribution.

Low and Tang (2007) proposed an alternative method to calculate the reliability index. Although the results are same, it is faster, robust and more efficient. Step 2 and step 4 are required to be modified in this method. The differences are in the following:

2(b). Input 'mean' (J5:J13). Input COV in (L5:L13) and obtain σ in (K5:K13). The column [nx] $([n_i])$ in (M5:M13) is assumed to be zero. And then obtain the 'x value' (I5:I13) with equation $x_i = \mu_i + \sigma_i n_i$, when it is normally distributed.

4(b). Change [nx] $([n_i])$ in (M5:M13).

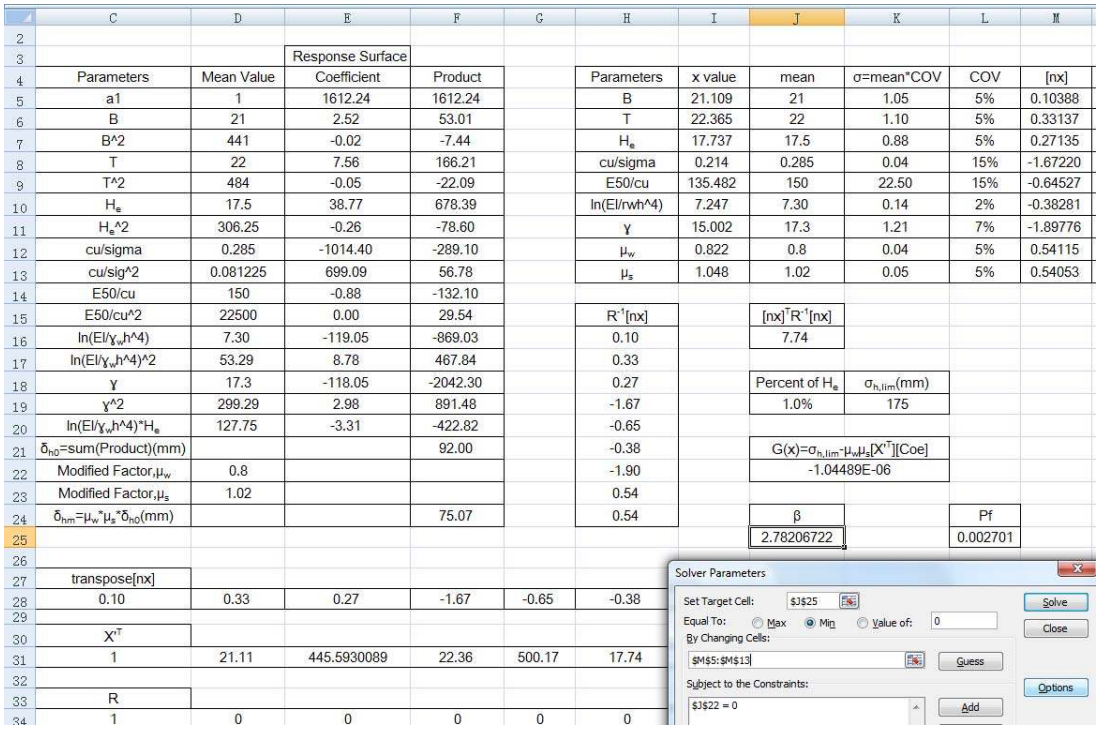

Parameters	Mean Value	Response Surface Coefficient	Product
a1	1	1612.24	1612.24
B	21	2.52	53.01
B^2	441	-0.02	-7.44
T	22	7.56	166.21
T^2	484	-0.05	-22.09
H_e	17.5	38.77	678.39
H_e^2	306.25	-0.26	-78.60
cu/sigma	0.285	-1014.40	-289.10
cu/sig^2	0.081225	699.09	56.78
E50/cu	150	-0.88	-132.10
E50/cu^2	22500	0.00	29.54
ln(El/γ_wh^4)	7.30	-119.05	-869.03
ln(El/γ_wh^4)^2	53.29	8.78	467.84
γ	17.3	-118.05	-2042.30
γ^2	299.29	2.98	891.48
ln(El/γ_wh^4)*H_e	127.75	-3.31	-422.82
δ_{h0}=sum(Product)(mm)			92.00
Modified Factor,μ_w	0.8		
Modified Factor,μ_s	1.02		
$\delta_{hm}=\mu_w*\mu_s*\delta_{h0}$(mm)			75.07

Parameters	x value	mean	σ=mean*COV	COV	[nx]
B	21.109	21	1.05	5%	0.10388
T	22.365	22	1.10	5%	0.33137
H_e	17.737	17.5	0.88	5%	0.27135
cu/sigma	0.214	0.285	0.04	15%	-1.67220
E50/cu	135.482	150	22.50	15%	-0.64527
ln(El/rwh^4)	7.247	7.30	0.14	2%	-0.38281
γ	15.002	17.3	1.21	7%	-1.89776
μ_w	0.822	0.8	0.04	5%	0.54115
μ_s	1.048	1.02	0.05	5%	0.54053

R^{-1}[nx]
0.10
0.33
0.27
-1.67
-0.65
-0.38
-1.90
0.54
0.54

[nx]^TR^{-1}[nx]
7.74

Percent of H_e	$\sigma_{h,lim}$(mm)
1.0%	175

G(x)=$\sigma_{h,lim}-\mu_w\mu_s$[X^T][Coe]
-1.04489E-06

β	Pf
2.78206722	0.002701

transpose[nx]					
0.10	0.33	0.27	-1.67	-0.65	-0.38

X^T					
1	21.11	445.5930089	22.36	500.17	17.74

R					
1	0	0	0	0	0

Figure 5.2 Process of Reliability Analysis

5.5.1.2 Effect of Soil Variables on P_f

To study the influence of the soil variables on the reliability analysis of wall deflection, analyses were carried out by varying the COVs of c_u/σ_v', E_{50}/c_u and γ. The results as presented in Figure 5.3(a) and Figure 5.3(c), respectively, show that P_f is more sensitive to c_u/σ_v' and γ than E_{50}/c_u. The P_f increases from 31% to 42% when COV of c_u/σ_v' increases from 10% to 40%. The P_f increases from 31.7% to 38% when COV of γ increases from 2% to 14%. The effect of correlation coefficient (ρ) between c_u/σ_v' and E_{50}/c_u on P_f is studied. Figure 5.4 shows the influence of ρ on P_f is small.

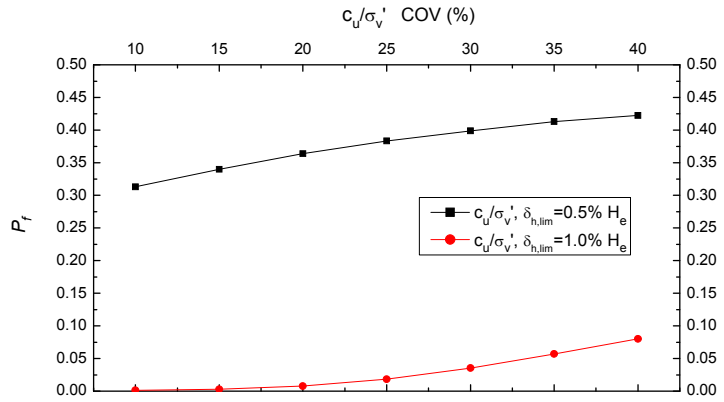

(a)

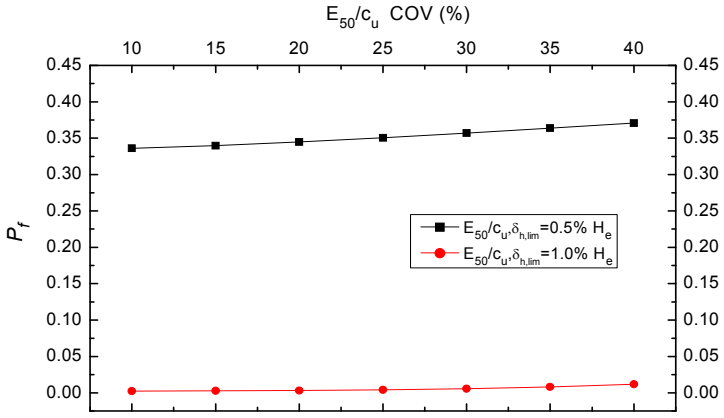

(b)

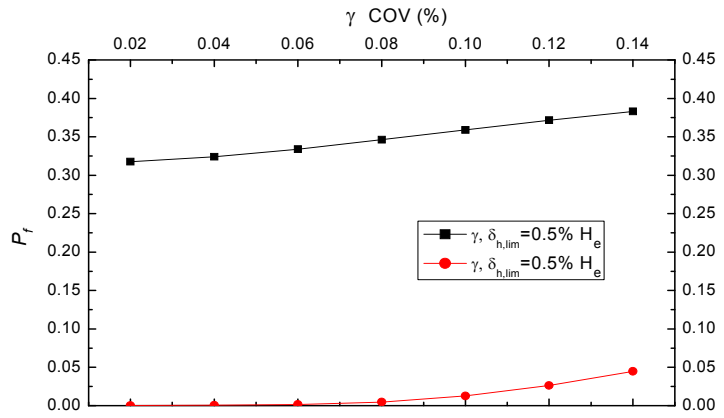

(c)

Figure 5.3 P_f for Various COV (a) c_u/σ_v' (b) E_{50}/c_u (c) γ

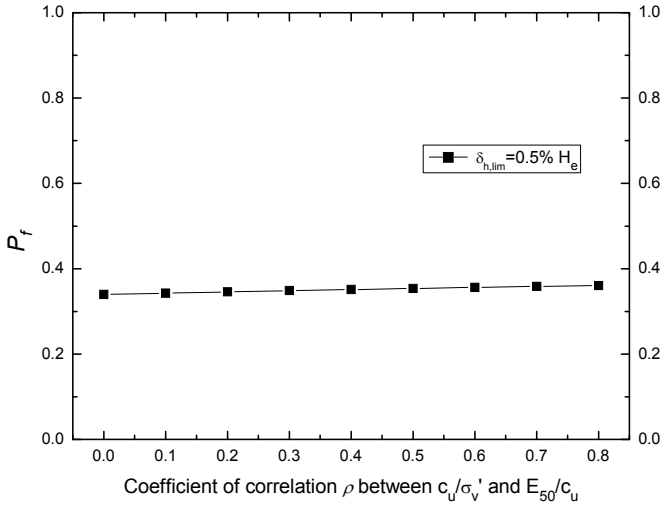

Figure 5.4 P_f for Various Degree of Correlation between c_u/σ_v' and E_{50}/c_u

5.5.1.3 Effect of Limiting Wall Deflection on P_f

As the magnitude of limiting wall deflection may typically vary from $0.5\%H_e$ to $1\%H_e$ for most projects in Singapore, the effect of limiting wall deflection on P_f is investigated. The reliability index β and P_f in Figure 5.5 are obtained from the reliability analyses with different limiting wall deflections. The results show the P_f increases sharply with the decrease of limiting wall deflection. Goh and Kulhawy (2005) also obtained the similar result. For the limiting wall deflection of $0.5\%H_e$, the P_f is 34% which means a high probability of wall deflection exceeding the limiting value. As expected, the limiting wall deflection has a significant effect on P_f.

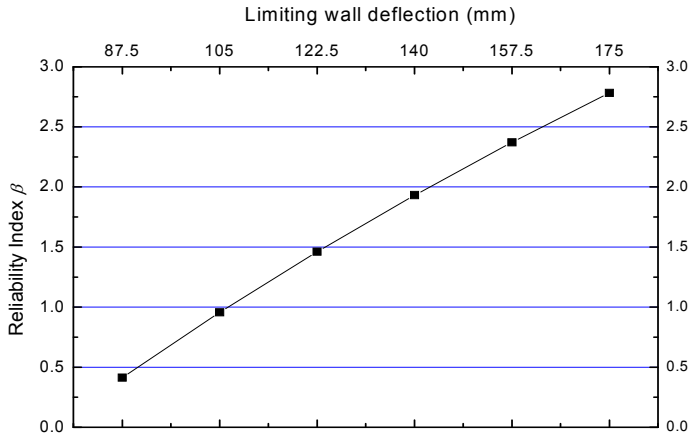

(a)

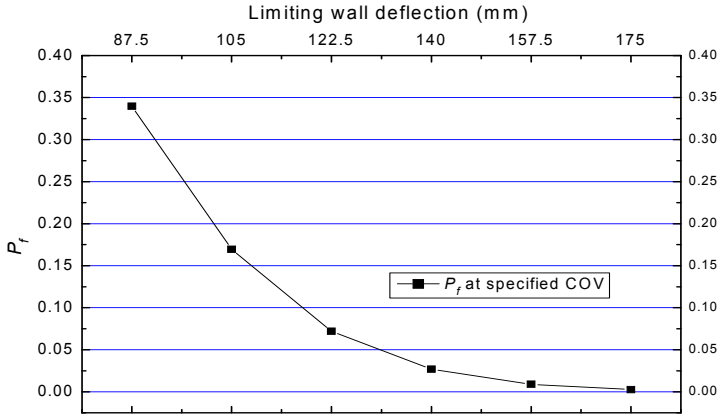

(b)

Figure 5.5 Effect of Various Limiting Wall Deflections at Final Depth of Excavation on: (a) reliability index; (b) P_f

5.5.1.4 Sensitivity Analysis by Spreadsheet

Sensitivity analysis is a way to assess the influence of variables on the state of the system. The main task of a sensitivity analysis is to identify the critical variables. The sensitivity parameter is often expressed as a partial form (Phoon, 2004):

$$u^* = \alpha^* \beta \tag{5.6}$$

$$\alpha^* = -\frac{\{\partial g/\partial u_1 \;\; \partial g/\partial u_2 \;\cdots\; \partial g/\partial u_n\}^T}{\sqrt{(\partial g/\partial u_1)^2 + \cdots (\partial g/\partial u_1)^2}} \tag{5.7}$$

in which u^* = solution vector and α^* = normalized gradient vector. Note that the normalized gradient vector provides a measure of sensitivity, which is arguably more informative than β in practical problems. Phoon (2004) proposed a simple forward difference method of computing this gradient information via spreadsheet. The advantages of this method are that the results can be validated and the case with correlated coefficients can also be worked out.

Low (1996) proposed another method to compute the sensitivity of a variable once the reliability is determined:

$$\alpha_i = -\frac{(x^* - m_{xi})}{\beta \sigma_{xi}} \tag{5.8}$$

where m_i and σ_i are mean value, standard deviation for variable x_i. The physical meaning for α_i is shown in Chapter 2.

The sensitivity parameter can be computed without requiring partial derivatives. Since the results obtained by these two method agreed with each other, the sensitivity of the reliability index in this case is illustrated by the method of Low (1996). The sensitivity parameter is obtained by entering Eq. (5.8) in column (N5:N13) in Figure 5.6 for a limiting wall deflection of $0.5\%H_e$. Since $\sum {\alpha_i}^2 = 1$, this means the sensitivity parameter measures the relative contribution of each input variable to the calculated reliability index. The result of the sensitivity analysis in Figure 5.7 shows that the reliability index is most sensitive to c_u/σ_v' and γ in this case when the COV is fixed.

Parameters	x value	mean	σ=mean*COV	COV	[nx]	α	α^2
B	21.022	21	1.05	5%	0.021	-0.050	0.003
T	22.073	22	1.10	5%	0.066	-0.161	0.026
H_e	17.547	17.5	0.88	5%	0.054	-0.130	0.017
cu/sigma	0.272	0.285	0.04	15%	-0.295	0.717	0.514
E50/cu	147.274	150	22.50	15%	-0.121	0.294	0.087
ln(EI/rwh^4)	7.290	7.30	0.14	2%	-0.074	0.180	0.033
γ	17.035	17.3	1.21	7%	-0.219	0.531	0.282
μ_w	0.802	0.8	0.04	5%	0.058	-0.141	0.020
μ_s	1.023	1.02	0.05	5%	0.058	-0.141	0.020
							1

$R^{-1}[nx]$
0.02
0.07
0.05
-0.30
-0.12
-0.07
-0.22
0.06
0.06

$[nx]^T R^{-1}[nx]$
0.17

Percent of H_e	$\sigma_{h,lim}$(mm)
0.5%	87.5

$G(x)=\sigma_{h,lim}-\mu_w\mu_s[X^T][Coe]$
-8.00186E-05

β	Pf
0.411924394	0.340197

Solver Parameters
Set Target Cell: $J$25
Equal To: Max Min Value of:
By Changing Cells:
$M$5:$M$13
Subject to the Constraints:
$J$22 = 0

Figure 5.6 Sensitivity Analysis for Farrer Park

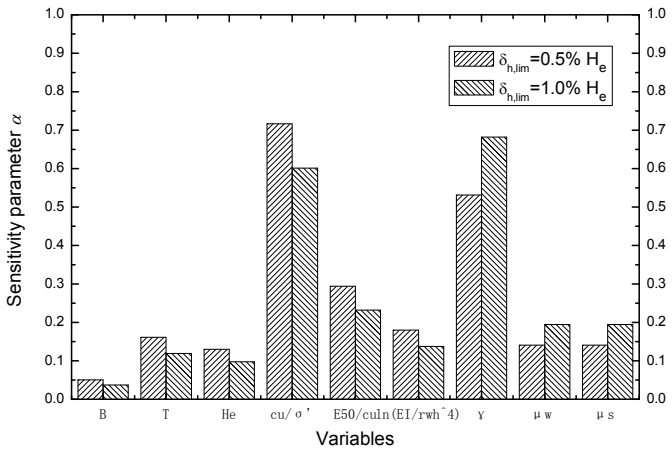

Figure 5.7 Sensitivity Parameter for Farrer Park

To investigate the effect of soil variables values on sensitivity parameter, some parametric analyses on γ, c_u/σ_v' and E_{50}/c_u are conducted. Figure 5.8, Figure

5.9 and Figure 5.10 show the effect of γ, c_u/σ_v' and E_{50}/c_u on the sensitivity parameter, wall deflection and P_f, respectively. The results show the increase of the three variables leads to the decrease of predicted wall deflection and accompanying decrease of P_f at a fixed limiting wall deflection. Figure 5.8(a) demonstrates the sensitivity parameter of γ decreases with increase of the variable, whereas Figure 5.9(a) for c_u/σ_v' shows the reverse effect while Figure 5.10(a) for E_{50}/c_u is almost constant.

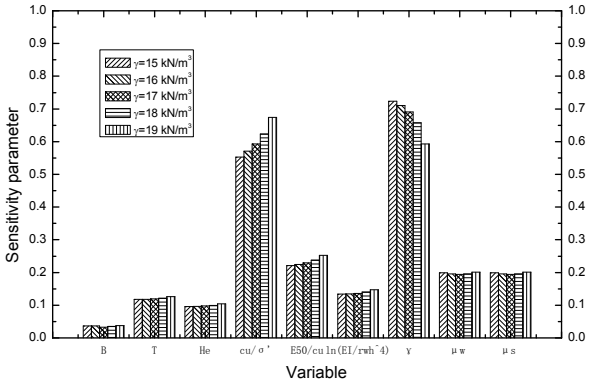

(a)

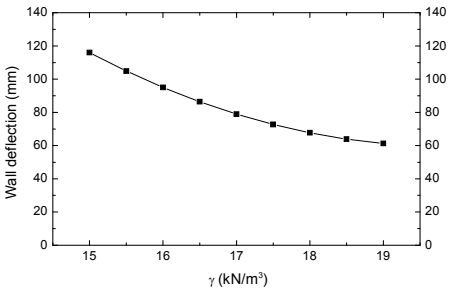

(b)

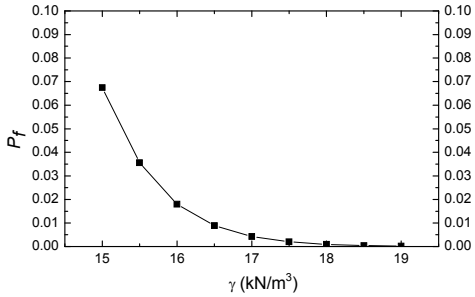

(c)

Figure 5.8 Effect of Soil Unit Weight γ on (a) Sensitivity Parameter (b) Wall Deflection (c) P_f

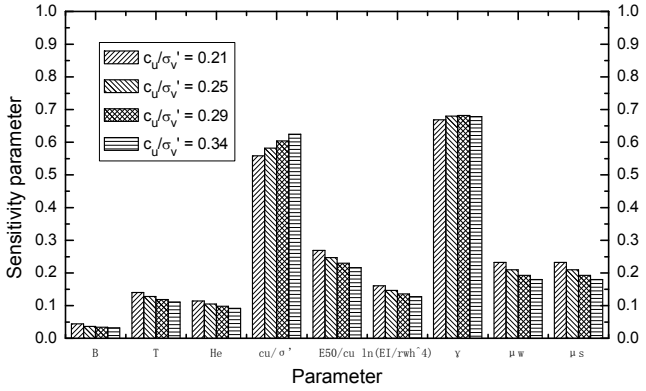

(a)

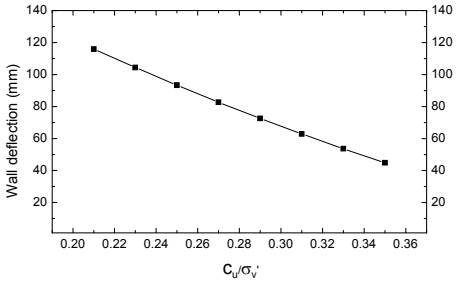

(b)

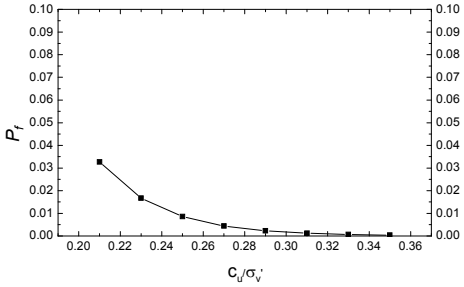

(c)

Figure 5.9 Effect of c_u/σ_v' on (a) Sensitivity Parameter (b) Wall Deflection (c) P_f

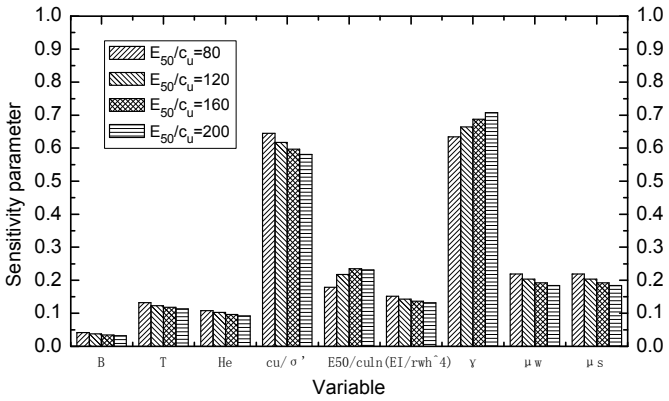

(a)

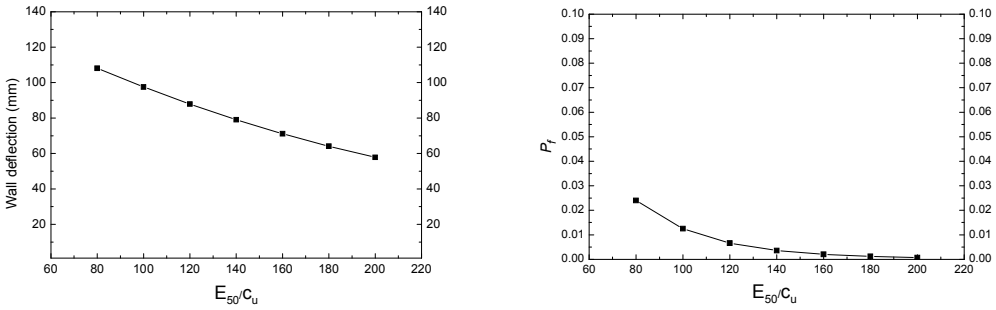

(b) (c)

Figure 5.10 Effect of E_{50}/c_u on (a) Sensitivity Parameter
(b) Wall Deflection (c) P_f

5.5.1.5 Lognormal Distribution

In the above reliability analysis it is assumed that all the variables are normally distributed. In this Section, the lognormal distribution is assumed for all the uncorrelated variables to investigate the distribution effect on reliability analysis.

To calculate the reliability index for non-normal distribution, the first-order Taylor series expansion (Phoon, 2004) is widely used to transform the non-normal distribution to equivalent normal distribution. Consider a lognormal random variable X with $\text{mean} = \text{m}$ and $\text{variance} = \text{s}^2$. By definition, ln(X) is normal distributed with $\text{variance} = \xi^2 = \ln(1 + \text{s}^2/\text{m}^2)$ and $\text{mean} = \lambda = \ln(\text{m}) - 0.5\xi^2$.The equivalent normal standard deviation (s^N) and mean (m^N) are:

$$\text{s}^\text{N} = \text{x} \times \xi \tag{5.9a}$$

$$\text{m}^\text{N} = \text{x} \times (1 - \ln(\text{x}^*) + \lambda \tag{5.9b}$$

Low and Tang (2007) provided a convenient method to calculate the reliability index for non-normal distributions. The method follows the steps of Low and Tang (2007) described in Section 5.5.1.1 where the expression $'x_i = \mu_i + \sigma_i n_i'$ is substituted with '$x_i = \exp(\lambda + \xi n_i)$' for the lognormal distribution. Figure 5.11 shows the reliability process of changing cells [nx] (M5:M13) in 'Solver', and [nx] is the dimensionless equivalent standard normal vector representing n_i. Figure 5.12 presents the P_f for variables with normal and lognormal distribution at different limiting wall deflections. The results show the difference is minimal even for large P_f.

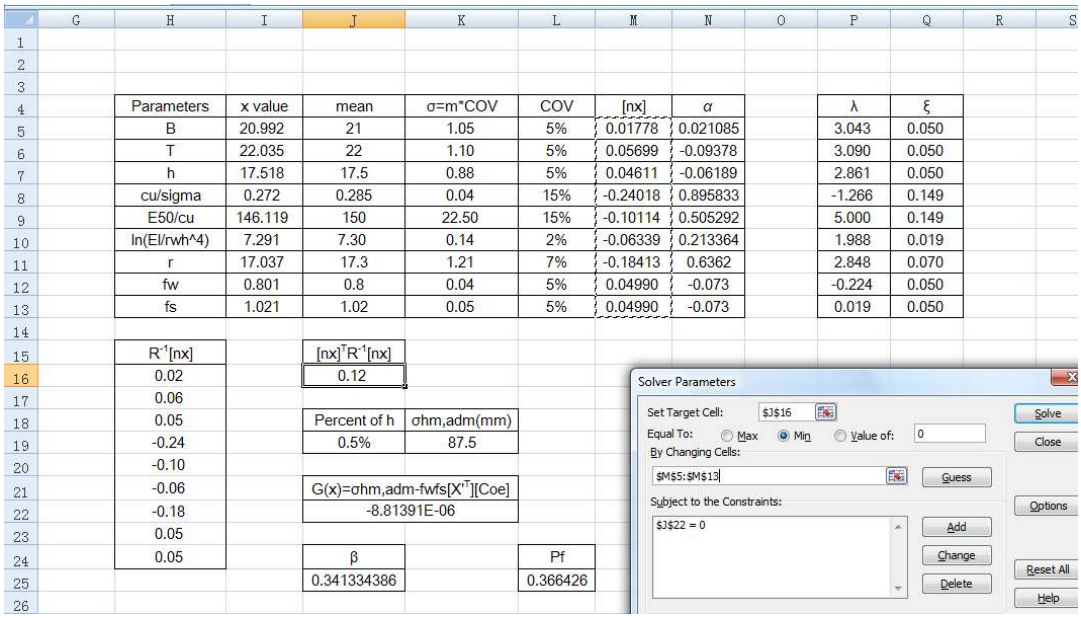

Parameters	x value	mean	σ=m*COV	COV	[nx]	α
B	20.992	21	1.05	5%	0.01778	0.021085
T	22.035	22	1.10	5%	0.05699	-0.09378
h	17.518	17.5	0.88	5%	0.04611	-0.06189
cu/sigma	0.272	0.285	0.04	15%	-0.24018	0.895833
E50/cu	146.119	150	22.50	15%	-0.10114	0.505292
ln(EI/rwh^4)	7.291	7.30	0.14	2%	-0.06339	0.213364
r	17.037	17.3	1.21	7%	-0.18413	0.6362
fw	0.801	0.8	0.04	5%	0.04990	-0.073
fs	1.021	1.02	0.05	5%	0.04990	-0.073

λ	ξ
3.043	0.050
3.090	0.050
2.861	0.050
-1.266	0.149
5.000	0.149
1.988	0.019
2.848	0.070
-0.224	0.050
0.019	0.050

$R^{-1}[nx]$
0.02
0.06
0.05
-0.24
-0.10
-0.06
-0.18
0.05
0.05

$[nx]^T R^{-1}[nx]$
0.12

Percent of h	σhm,adm(mm)
0.5%	87.5

G(x)=σhm,adm-fwfs[X'^T][Coe]
-8.81391E-06

β	Pf
0.341334386	0.366426

Figure 5.11 Reliability Analyses for Lognormal Distributions

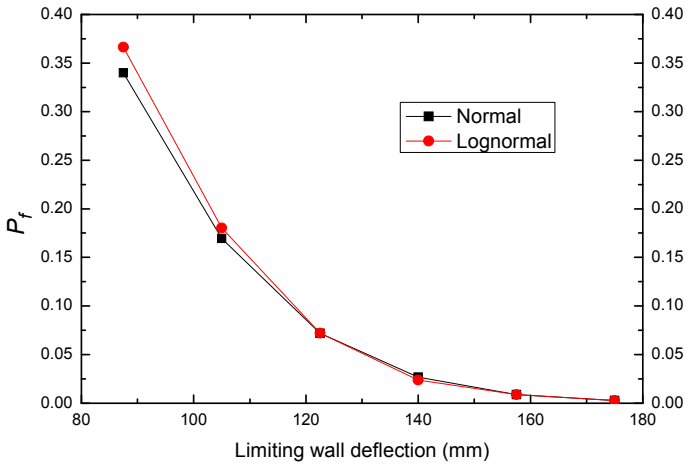

Figure 5.12 Failure Probabilities for Normal and Lognormal Distributions

5.5.2 TNEC (surface settlement)

As shown in Section 4.6, the ratio of the maximum wall deflection and maximum surface settlement is around 0.7. Since the maximum surface settlement is much dependent on the ratio μ_R, this study focuses the influence of μ_R. The other variables should have the same influence on the surface settlement as the wall deflection described in the previous section.

Details of TNEC project are described in Section 3.3.7. The reliability analysis process is shown in Figure 5.13, which only involve modifying the limit function to Eq. (5.3b) and adding an extra variable μ_R compared with the reliability analysis for wall deflection. The predicted maximum surface settlement is 80.8 mm by Eq.4.20, which is comparable with the measured value. The analyses adopt the limiting settlement as $0.5\%\sim0.7\%H_e$ and COV of μ_R as $3\%\sim19\%$ to see the influence of deflection ratio on the reliability analysis of settlement. Figure 5.14 presents the P_f for the different deflection ratios μ_R from 0.45 to 0.85 for different limiting settlements. The results show that P_f is sensitive to μ_R and

$\delta_{v,lim}$ especially for the large μ_R and small $\delta_{v,lim}$. The result of reliability analysis of surface settlement at $\mu_R = 0.7$ with COV from 3% to 19% is shown in Figure 5.15. The P_f increases from 14% to 22% at limiting settlement of $0.7\%H_e$ and increases from 0.14% to 1.5% at limiting settlement of $0.5\%H_e$ when COV increases. The sensitivity parameters of this case at two different limiting settlements with $\mu_R = 0.7$ are shown in Figure 5.16. The results indicate the deflection ratio μ_R plays a significant role in estimating β.

Reliability Analysis on Settlement

Parameters	values	Response Surface Coefficient	Product
a1	1	1612.24	1612.24
B	43	2.52	108.54
B^2	1849	-0.02	-31.20
T	33	7.56	249.32
T^2	1089	-0.05	-49.71
H_e	19.7	38.77	763.67
H_e^2	388.09	-0.26	-99.60
cu/sigma	0.32	-1014.40	-324.61
cu/sig^2	0.1024	699.09	71.59
E50/cu	100	-0.88	-88.07
E50/cu^2	10000	0.00	13.13
ln(EI/γ_wh^4)	7.30	-119.05	-869.13
ln(EI/γ_wh^4)^2	53.30	8.78	467.95
γ	19	-118.05	-2242.99
γ^2	361	2.98	1075.30
ln(EI/γ_wh^4)*H_e	143.83	-3.31	-476.03
δ_{h0}=sum(Product)(mm)			180.38
Modified Factor,μ_w	0.8		
Modified Factor,μ_s	0.8		
$\delta_{hm}=\mu_w*\mu_s*\delta_{h0}$(mm)			115.44
μ_R	0.70		
$\delta vm=\mu_R*\delta_{hm}$(mm)			80.81

	x value	mean	σ=mean*COV	COV	[nx]	α
B	43.107	43	2.15	5%	0.05	-0.05378
T	33.266	33	1.65	5%	0.16	-0.17435
H_e	19.795	19.7	0.99	5%	0.10	-0.10429
cu/sigma	0.290	0.32	0.05	15%	-0.63	0.684235
E50/cu	96.955	100	15.00	15%	-0.20	0.219656
ln(EI/rwh^4)	7.275	7.30	0.15	2%	-0.18	0.194129
γ	18.759	19	1.33	7%	-0.18	0.195957
μ_w	0.809	0.8	0.04	5%	0.22	-0.2368
μ_s	0.809	0.8	0.04	5%	0.22	-0.2368
μ_R	0.736	0.7	0.08	11%	0.46	-0.50117

R^{-1}[nx]
0.05
0.16
0.10
-0.63
-0.20
-0.18
-0.18
0.22
0.46

Percent of h	$\sigma_{vm,lim}$(mm)
0.5%	98.5

[nx]^TR^{-1}[nx]
0.85

G(x)=$\sigma_{vm,lim}-\mu_R\mu_w\mu_s$[$X^T$][Coe]
0.000

β
0.92425626

transpose[nx]							
0.05	0.16	0.10	-0.63	-0.20	-0.18	-0.18	0.22

X^T							
1	43.11	1858.20	33.27	1106.62	19.79	391.84	0.29

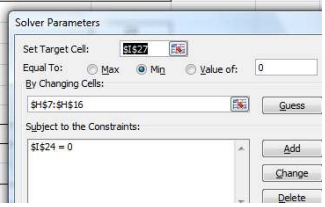

Figure 5.13 Reliability Analysis for Surface Settlement

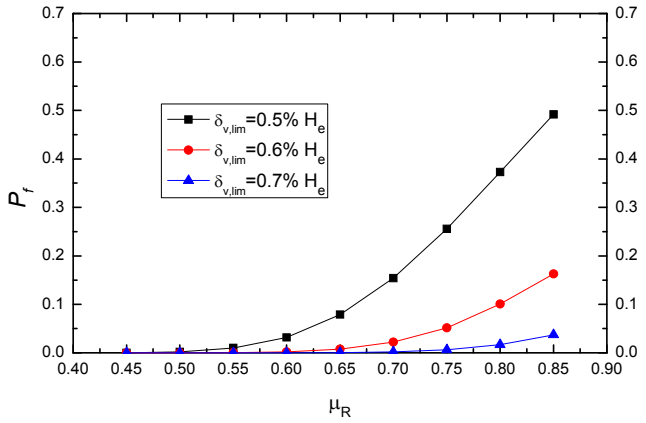

Figure 5.14 P_f for Different μ_R and Different $\delta_{v,lim}$

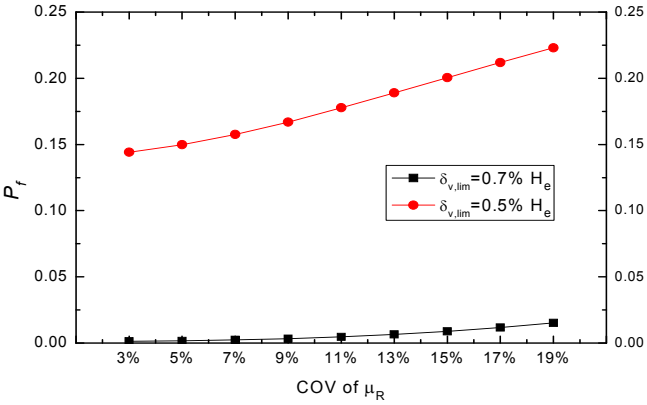

Figure 5.15 P_f for Different COV of μ_R and Different $\delta_{v,lim}$

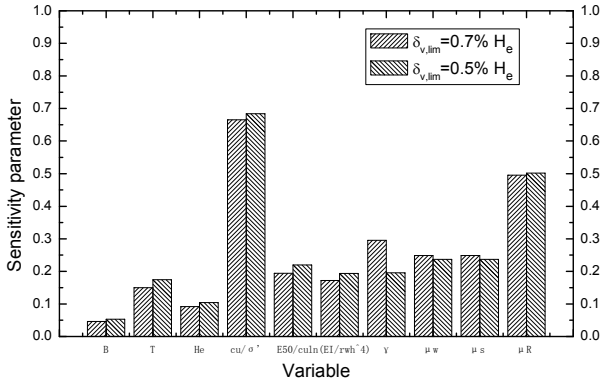

Figure 5.16 Sensitivity Parameter of μ_R for Different $\delta_{v,lim}$

5.6 Charts for Predicting P_f

This section aims to provide simplified charts to estimate P_f for preliminary design cases. The charts will enable engineers to estimate the safety of their excavation without having to perform reliability analyses. A complete reliability analysis is recommended in the detailed design phase.

To investigate the P_f for normally distributed variables, a series of parametric studies are conducted. The basic values for the variables listed in Table 5.3 are based on the 'average value' in Table 4.9. The normal ranges and various values of the variables are listed in Table 5.4. The limiting wall deflection is assumed as $1.0\%H_e$ firstly. The COV values and analysis steps are the same as in Section 5.5.1.1. The results in Figure 5.17 (a ~ g) are obtained from the cases with basic variable values in Table 5.3 and the corresponding values in Table 5.4.The results demonstrate that the failure probability P_f increases significantly as c_u/σ'_v, γ, and $ln(EI/\gamma_w h_{avg}^4)$ decreases and as T increases.

For cases with different limiting wall deflection such as $\delta_{h,lim} = 1.0\%$, 0.8%, 0.6% and $0.5\%H_e$, it was found that failure probability is directly related to the factor $\delta_{hm}/\delta_{h,lim}$, where δ_{hm} is the predicted wall deflection calculated by the response surface method and $\delta_{h,lim}$ is the limiting wall deflection. The data of P_f versus $\delta_{hm}/\delta_{h,lim}$ for $\delta_{h,lim} = 1.0\%$, 0.8%, 0.6% and $0.5\%H_e$ are plotted in Figure 5.18, 5.19, 5.20 and 5.21, respectively. The plots show that the data points from different cases can be approximated by simple polynomial equations shown in Eq. (5.10).

For $\delta_{hm}/\delta_{h,lim} \geq 0.35$:

$$P_f = 1.82(\delta_{hm}/\delta_{h,lim} - 0.35)^3 \quad (\delta_{h,lim} = 1.0\%H_e) \qquad (5.10a)$$

$$P_f = 1.47(\delta_{hm}/\delta_{h,lim} - 0.35)^{2.5} \quad (\delta_{h,lim} = 0.8\%H_e) \tag{5.10b}$$

$$P_f = 0.95(\delta_{hm}/\delta_{h,lim} - 0.35)^{1.5} \quad (\delta_{h,lim} = 0.6\%H_e) \tag{5.10c}$$

$$P_f = 0.84(\delta_{hm}/\delta_{h,lim} - 0.35)^{1.2} \quad (\delta_{h,lim} = 0.5\%H_e) \tag{5.10d}$$

For $\delta_{hm}/\delta_{h,lim} < 0.35$:

$$P_f = 0 \tag{5.11}$$

The results in these figures show good agreement between the calculated P_f by Eq. (5.10) and the actual P_f values. Alternatively, the chart in Figure 5.22 can be used instead of Eq. (5.10).

Table 5.3 Basic Values for Variables

Variable	B (m)	T (m)	H_e (m)	c_u/σ'_v	E_{50}/c_u	$ln(\frac{EI}{\gamma_w h_{avg}^4})$	γ(KN/m^2)	μ_w	μ_s
Basic Value	30	25	15.47	0.288	137	7.25	17.3	0.84	0.98

Table 5.4 Values of Variables for Parametric Study

No.	c_u/σ'_v	E_{50}/c_u	B (m)	T (m)	H_e (m)	$ln(EI/\gamma_w h_{avg}^4)$	γ(KN/m^2)
1	0.21	80	60	40	7	6.10 (d = 0.6m)	15.0
2	0.23	100	55	37	9	6.56 (d = 0.7m)	15.5
3	0.25	120	50	34	11	6.96 (d = 0.8m)	16.0
4	0.27	140	45	31	13	7.31 (d = 0.9m)	16.5
5	0.29	160	40	28	15	7.63 (d = 1.0m)	17.0
6	0.31	180	35	25	17	7.92 (d = 1.1m)	17.5
7	0.33	200	30	22	19	8.18 (d = 1.2m)	18.0
8	0.35	220	25	19	21	8.42 (d = 1.3m)	18.5
9	0.37	240	20	16	23	8.64 (d = 1.4m)	19.0

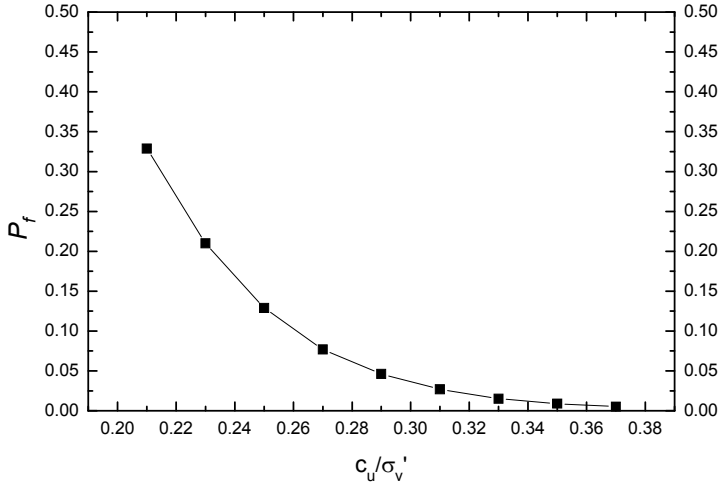

(a)

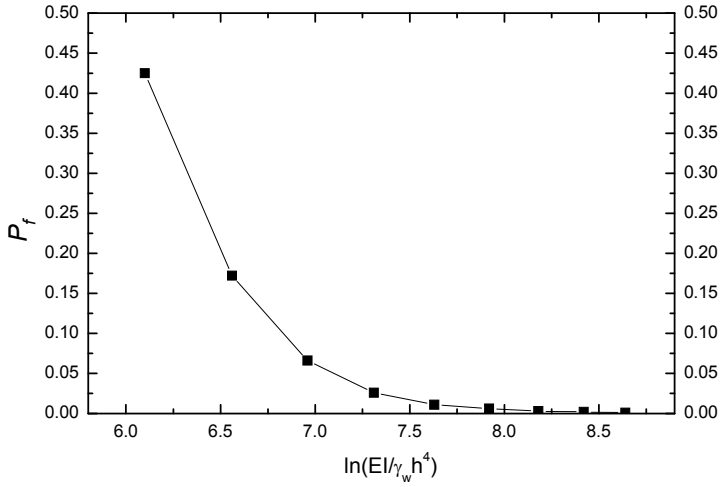

(b)

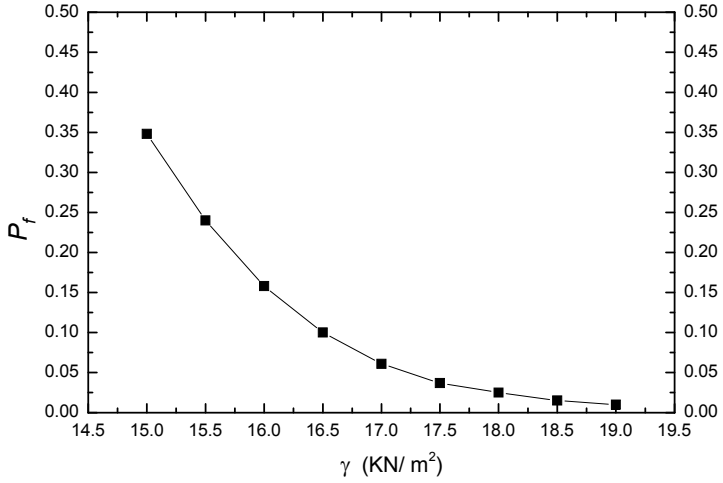

(c)

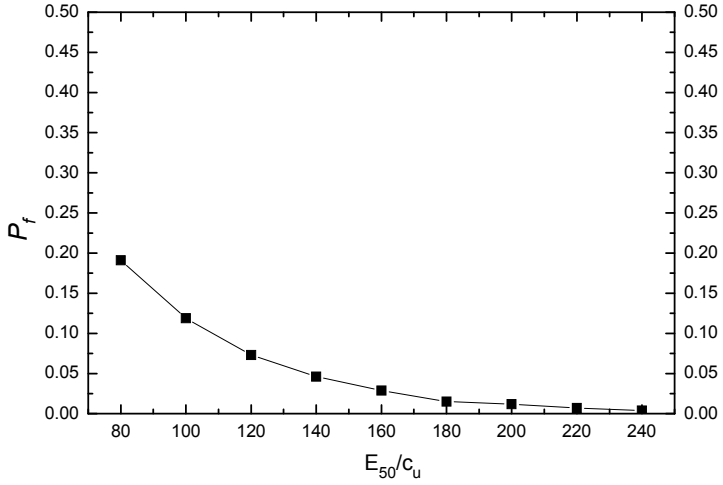

(d)

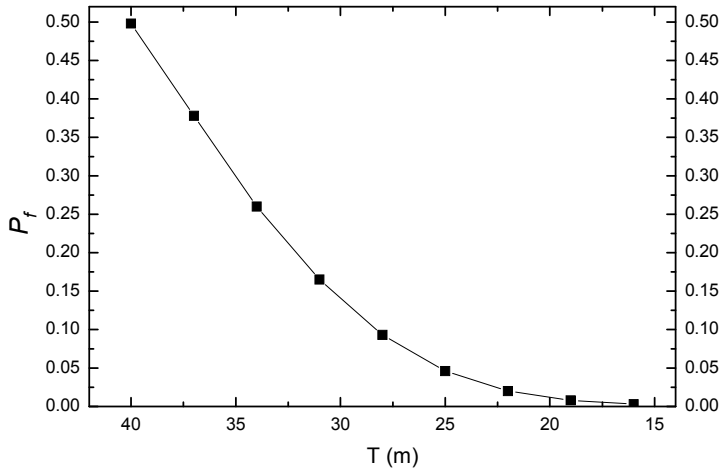

(e)

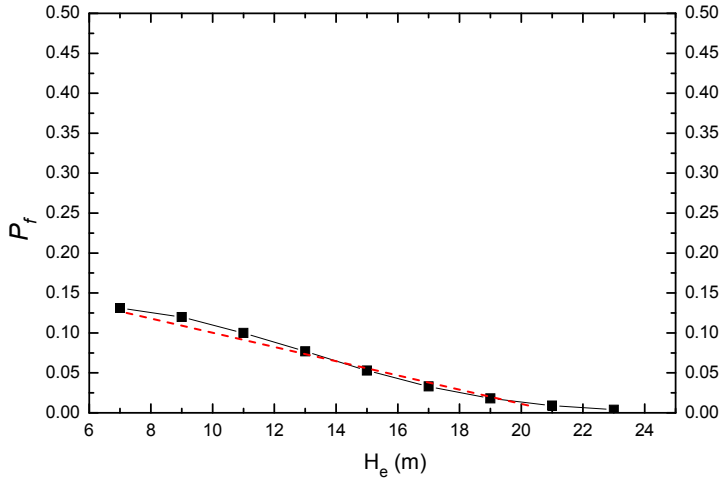

(f)

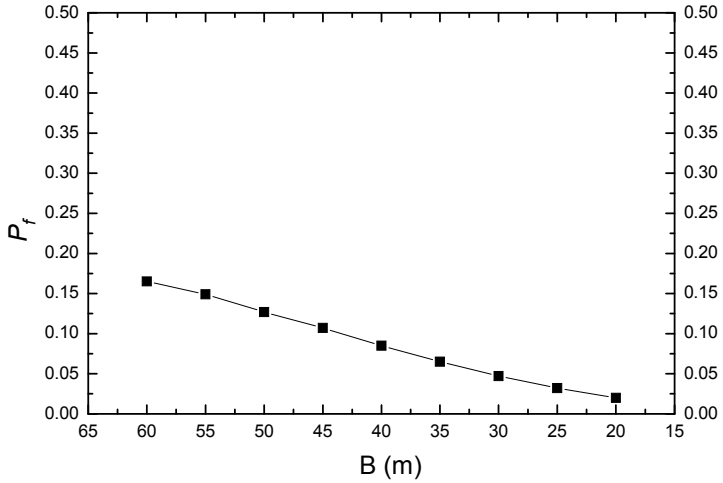

(g)

Figure 5.17 (a ~ g) Effects of Various Variables on P_f

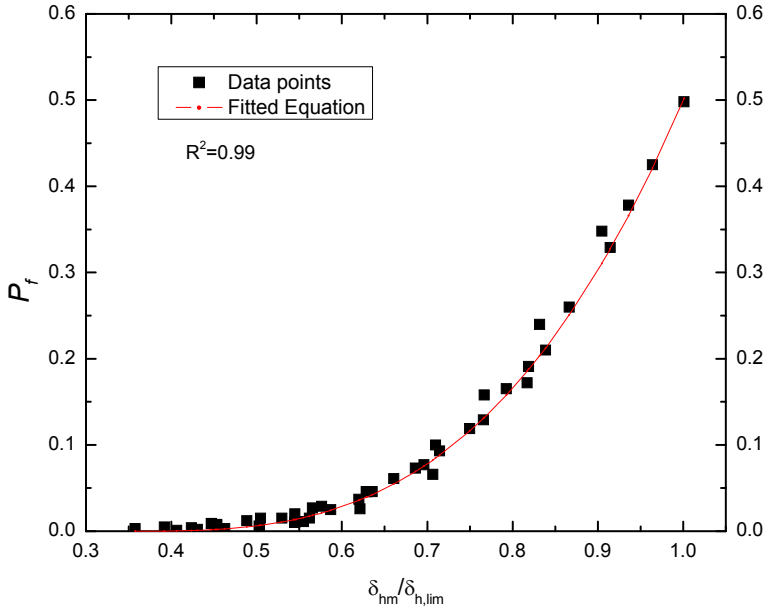

(a)

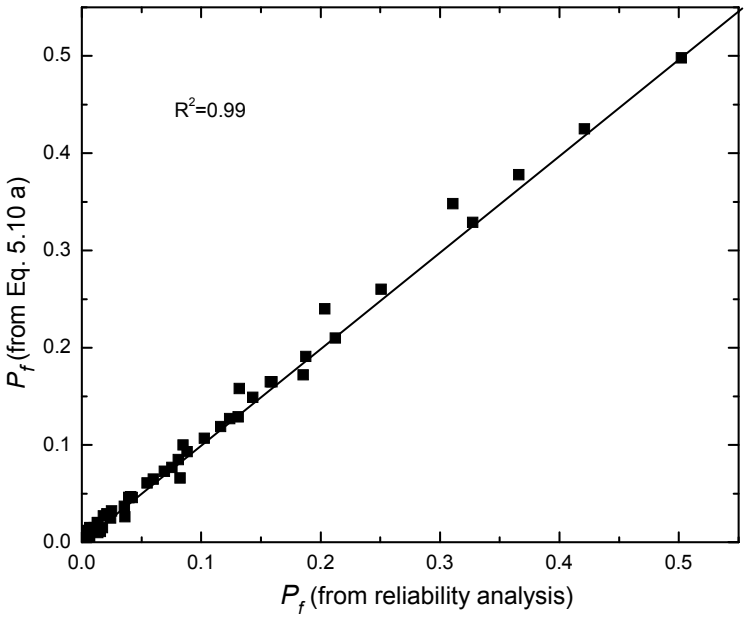

(b)

Figure 5.18 P_f at $\delta_{h,lim} = 1.0\%H_e$ (a) Fitted Curve (b) Comparison of Values Using Eq. (5.10a) and Data from Spreadsheet Reliability Analysis

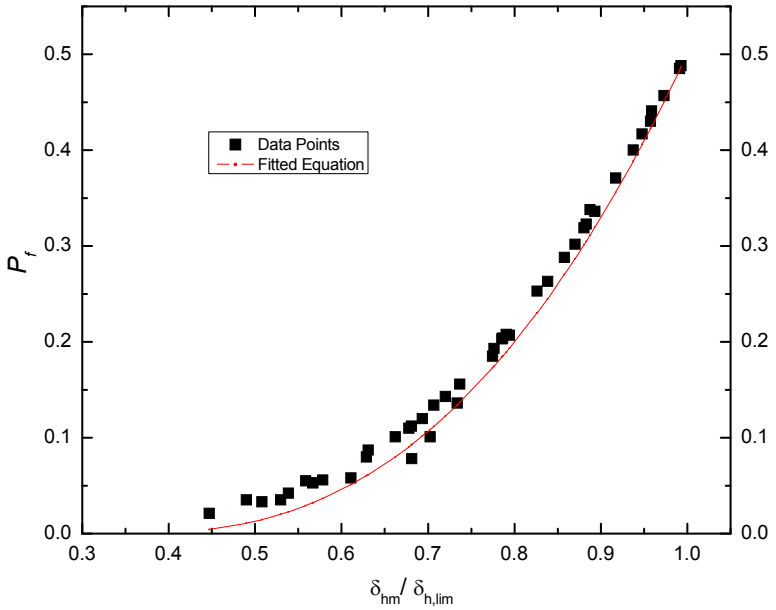

(a)

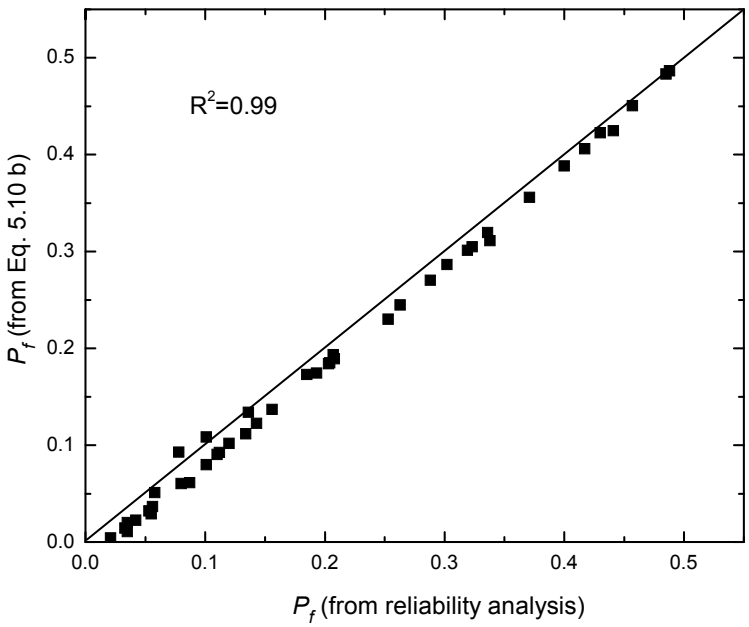

(b)

Figure 5.19 P_f at $\delta_{h,lim} = 0.8\%H_e$ (a) Fitted Curve (b) Comparison of Values Using Eq. (5.10b) and Data from Spreadsheet Reliability Analysis

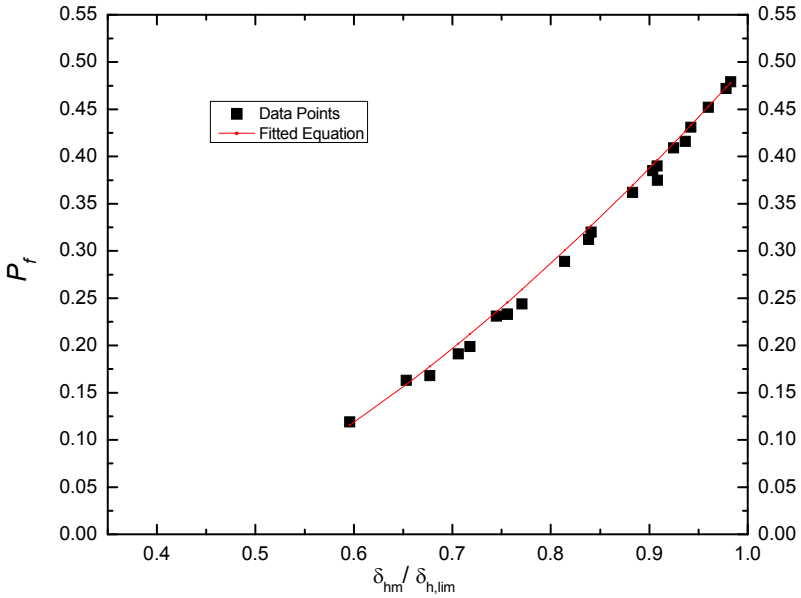

(a)

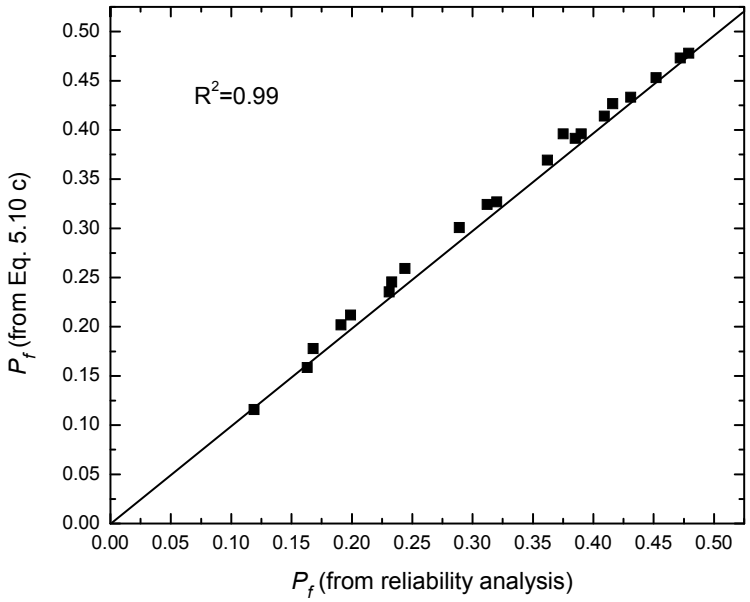

(b)

Figure 5.20 P_f at $\delta_{h,lim} = 0.6\%H_e$ (a) Fitted Curve (b) Comparison of Values Using Eq. (5.10c) and Data from Spreadsheet Reliability Analysis

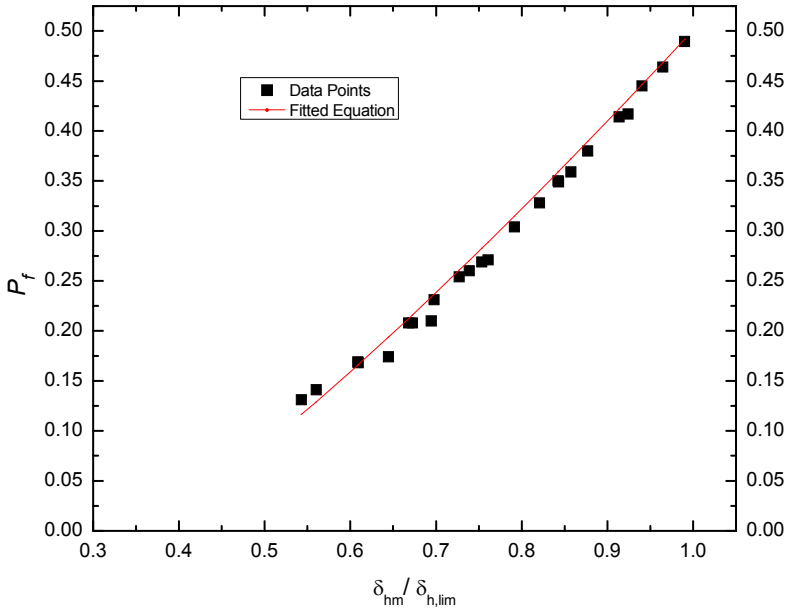

(a)

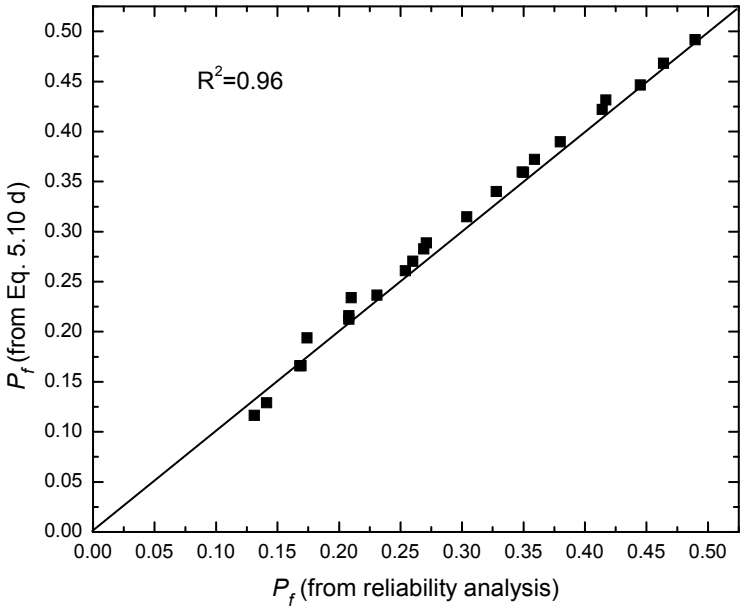

(b)

Figure 5.21 P_f at $\delta_{h,lim} = 0.5\%H_e$ (a) Fitted Curve (b) Comparison of Values Using Eq. (5.10d) and Data from Spreadsheet Reliability Analysis

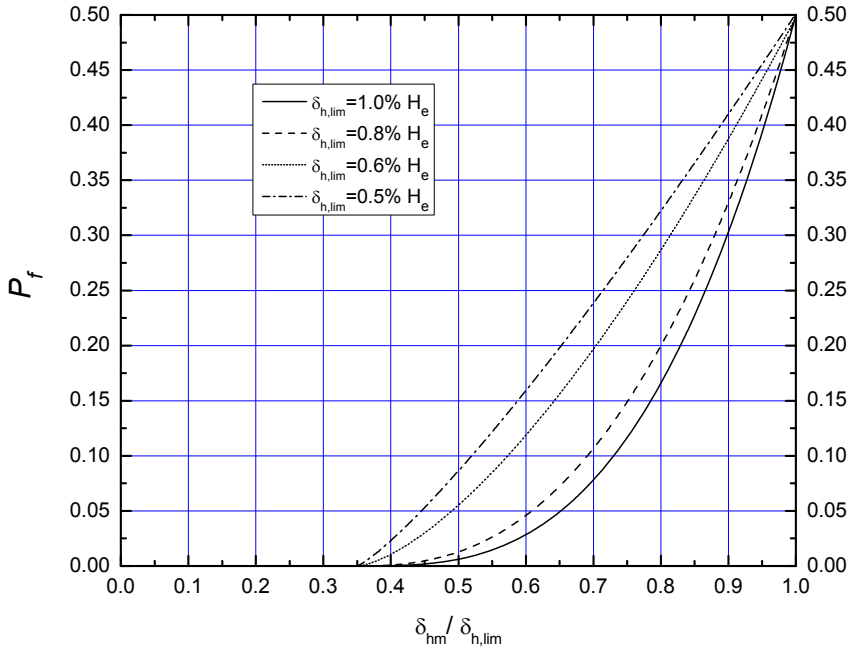

Figure 5.22 Chart for Predicting P_f for Wall Deflection

Since excavation depth H_e affects the cases with different H_e, Figure 5.17(f) is used to take into consideration this factor, which shows P_f decreases with the increase of H_e. Since the studied excavation depth is $H_e = 15.47$ m, the effect of H_e is considered to modify the failure probability $P_{f,m}$. The $P_{f,m}$ can be estimated from the following equation.

For $\delta_{hm}/\delta_{h,lim} \geq 0.35$

$$P_{f,m} = P_f + 0.01 \times (15.47 - H_e) \tag{5.12}$$

Since there is a deterministic relationship between maximum wall deflection and maximum surface settlement, a similar chart in Figure 5.23 can be used to estimate P_f for surface settlement, and then obtain $P_{f,m}$ from Eq. (5.12).

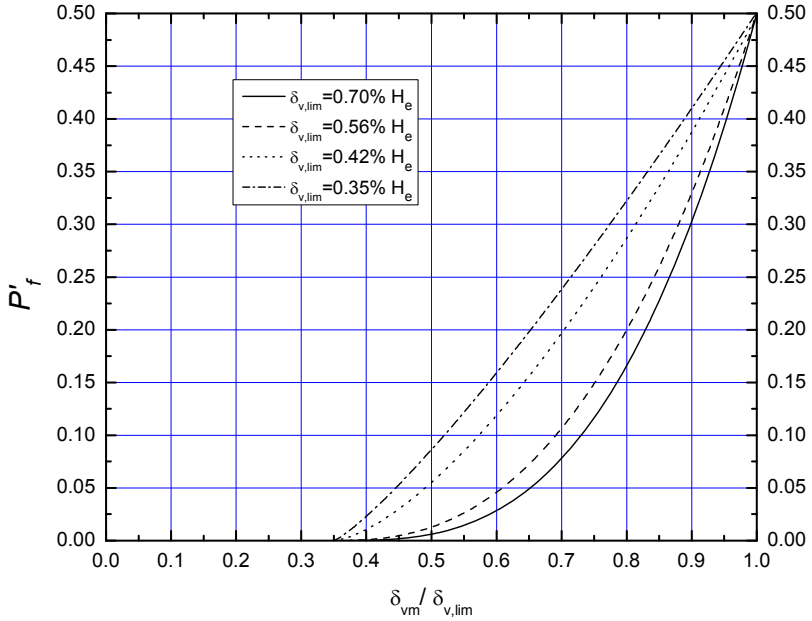

Figure 5.23 Chart for Predicting P_f for Surface Settlement

The procedure for estimating P_f for wall deflection and surface settlement involves the following steps:

1. Input soil variables and non-soil variables in the response surfaces to calculate maximum wall deflection δ_{hm} and surface settlement δ_{vm}.
2. Obtain the ratio $\delta_{hm}/\delta_{h,lim}$ with the set $\delta_{h,lim} = \lambda_h H_e$, and then obtain P_f from Figure 5.22.
3. Obtain the ratio $\delta_{vm}/\delta_{v,lim}$ with the set $\delta_{v,lim} = \lambda_v H_e$, then obtain P_f from Figure 5.23.
4. Modify P_f with Eq. (5.12) both for wall deflection and surface settlement.

5.7 Summary

The reliability analysis using the response surface method is conducted for wall deflection and surface settlement in this Chapter. Two examples are used to demonstrate the steps and results of the reliability analysis.

(a) The magnitudes of limiting wall deflection and surface settlement have significant effect on P_f and need to be characterized properly.

(b) The failure probability is not significantly influenced by normal or lognormal distribution of the variables.

(c) The most sensitive factors to P_f for wall deflection are c_u/σ_v' and γ, and μ_R is sensitive to P_f for surface settlement.

(d) Simplified charts are proposed to estimate P_f of wall deflection and surface settlement.

Chapter 6

CONCLUSIONS AND RECOMMENDATIONS

6.1 Conclusions

This study has two aims. The first one is to obtain reasonable predictions on excavation behavior by conducting a series of parametric studies with the small strain model HSS. The second one is to carry out reliability analysis on wall deflection and surface settlement using the predicted response surfaces. The main findings are summarized below.

6.1.1 Estimation of HS and HSS Parameters for Excavation Analysis

Several case histories have been back analyzed using the two soil models. Some reasonable estimation for the effective friction angle and soil stiffness of clay is proposed for the two models to predict the undrained behavior of excavations. The results show the ratio of E_{50}/c_u is concentrated in the range of 100~150 and the effective friction angle φ follows the equation recommended by Wroth and Houlsby (1985) for undrained behavior of soft clay. The method which is suggested by PLAXIS manual to estimate the small strain parameter G_0 is presented in the forms of equations.

6.1.2 Coefficient for Estimating the Small Strain Effect

A coefficient and the corresponding chart are proposed to estimate the small strain effect through conducting a series of analysis using the HSS and HS soil models. The results show the effect of small strain on excavation problems depends on the ratio of G_0/E_{ur} and the excavation depth H_e. The study suggested that the small strain effect is not significant for Singapore marine clay in excavation problems

with depth ($H_e \geq 8$ m).

6.1.3 Methods for Predicting Wall Deflection Path

Based on the parametric study, a simple method is suggested to predict the wall deflection path when the initial stages of wall deflection are known. The method can be applied to estimate the wall deflections at the next and the final stage for excavations.

6.1.4 Response Surfaces for Wall Deflection and Surface Settlement

The response surfaces were developed to estimate the maximum wall deflection and the maximum surface settlement based on the results of the parametric study. The response surfaces are applicable for excavations with diaphragm walls in soft clay. Ihe equations provide an efficient way to estimate the maximum wall deflection and maximum surface settlement without conducting numerical analysis.

6.1.5 Charts for Predicting APD

The charts are proposed for estimating the maximum apparent earth pressure and apparent pressure diagram by considering the two most critical factors for excavations with diaphragm walls in soft clay. The results show the clay thickness is the most important factor affecting the magnitude of the maximum apparent earth pressure.

6.1.7 Charts for Estimating P_f

Some charts are presented to estimate P_f for wall deflection and surface settlement of excavations. The step-by-step procedure for generating the approximate P_f is shown in Section 5.6.

6.1.8 Limitations of the Proposed Methods

a) The proposed response surface for wall deflection and the proposed chart for estimating the maximum apparent pressure are only applicable for excavations in soft clay with $H_e \geq 8$ m and assuming the diaphragm wall penetrates into the stiff clay and/or with a little movement at the toe. The vertical spacing of excavations should be around 3 m.

b) The assumed deflection ratio $\mu_R = 0.7$ can be used to estimate the maximum surface settlement for deep excavations $H_e \geq 8$ m, assuming that the wall should be restrained at the toe. The soils are assumed to be undrained and no consolidation is involved.

c) The charts for estimating the failure probability of excavations follow the limitation of previous clauses and it should be noted that the predicted results are an approximation.

6.2 Recommendations for Future Research

The following highlights some further research that could be examined.

a) The HSS model can be employed in other geotechnical problems to study the soil small strain effect on the deformations and stress. More data of G_0 or G_0/c_u in HSS should be collected for various soils for excavation problems. The normal strain and shear strain of soil elements in different districts of excavations can be characterized properly to consider their influences on the wall deflection and soil deformation.

b) Since the proposed response surfaces for wall deflection is only applicable for diaphragm walls in soft clay, more complicated type of response surfaces considering wide range of wall stiffness and soil stiffness are required for various excavation problems. Other factors such as vertical strut spacing, different soil strength distributions, multiple clay layers and soil stress histories

can be considered in generating the response surface.

c) The influence of soil consolidation on the deformation ratio μ_R can be incorporated in predicting the maximum surface settlement. The soil consolidation may be the main factor affecting μ_R.

d) Response surfaces for maximum bending moment and strut force also can be generated to carry out the reliability analysis. As the limiting values for wall deflections or surface settlement in limit state function (LSF) have a significant effect on the probability of failure, the hazards associated with excavation behavior for adjacent buildings, facilities, tunnels, roads, and so on should be assessed carefully and three dimension analyses may be involved.

e) The system reliability for a excavation project can be defined and characterized properly after calculating the failure probability for wall deflection, surface settlement, basal heave, bending moment, strut force, etc. The index of system reliability can be used to assess the safety of the project.

REFERENCES

Alpan, I. (1970), "The Geotechnical Properties of Soils", Earth-Science Reviews, Vol. 6, pp. 5-49.

Anderson D.G. and Woods R.D. (1976), "Time-Dependent Increase in Shear Modulus of Clay", Proc. ASCE: Journal of the Geotechnical Engineering Division, 102 (GT5): 525-537.

Ang, A. H. S. and Tang, W. H. (1984), Probability Concepts in Engineering Planning and Design, Vol. II – Decision, Risk and Reliability. Wiley, New York.

Atkinson, J. H. and Sallfors, G. (1991), "Experimental Determination of Soil Properties", In Proc. 10th ECSMFE, Florence, Vol. 3, pp. 915-956.

Ashraf, S. O. and Bolton, M. D. (2006), "Ground Movement Predictions for Braced Excavations in Undrained Clay", Journal of Geotechnical and Geoenvironmental Engineering, Vol. 132, No. 4, pp. 465-477.

Beacher, G. B. and Christian, J. T. (2003), Reliability and Statistics in Geotechnical Engineering. Wiley, West Sussex, England.

Benz, T., (2007), "Small-Strain Stiffness of Soil and Its Numerical Consequences", Ph.D, Thesis, University of Stuttgart.

Bjerrum, L. (1963), "Discussion on 'Proceedings of the European conference on soil mechanics and foundation engineering, vol. III.'", Norwegian Geotech. Inst. Publ. No. 98, Oslo, Norway, 1-3.

Bjerrum, L. and Eide, O. (1956), "Stability of Strutted Excavation in Clay", Geotechnique, London, England, Vol. 6, pp. 57-62.

Boone, S. J. (1996), "Ground-Movement-Related Building damage", Journal of Geotechnical Engineering, Vol. 122, No. 11, pp. 886-896.

Bowles, J. E. (1988), Foundation Analysis and Design, 4th ed., McGraw-Hill Book Company, New York.

Box, G. E. P. and Wilson, K. B. (1951), "On the Experimental Attainment of Optimum Conditions", Journal of the Royal Statistical Society B 13, pp. 1-45.

Brinkgreve, R. B. J. and Vermeer, P. A. (2002), PLAXIS User's Manual, Version 8. Balkema, Rotterdam.

Chang, J. D., and Wong, K. S. (1996), "Apparent Pressure Diagram for Braced Excavations in Soft Clay with Diaphragm Wall", Proceedings of International Symposium on Geotechnical Aspects of Underground Construction in Soft Ground. City University London.

Chew C.H., Lee, F.H., Lim, S.C., Lim, S.P., Quek, S.T. and Tan, T.S. (1997), Review of Floating Slab Track System for North-East Line. Stage II: Ground Vibration Study. Prepared for Land Transport Authority, Singapore.

Clough, G. W. and O'Rourke, T. D. (1990), "Construction Induced Movements of In Situ Walls", In Proceedings, Design and Performance of Earth Retaining Structures, ASCE Special Conference, Ithaca, New York, pp. 439-470.

Cornell, C. A. (1969), "A Probability-based Structural Code", American Concrete Institute, Vol. 66, No. 12, pp. 974-985.

Ditlevsen, O. (1981), Uncertainty Modeling: With Applications to Multi-dimensional Civil Engineering Systems, McGraw-Hill, New York.

Duncan, J. M. (2000), "Factors of Safety and Reliability in Geotechnical Engineering", Journal of Geotechnical and Geoenvironmental Engineering, Vol. 126, No. 4, pp. 307-316.

Duncan, J. M. and Buchigani, A. L. (1976), "An Engineering Manual for Settlement Studies", Geotechnical Engineering Report, Department of Civil Engineering, University of California, Berkeley, 94 pp.

Goh, A. T. C. (1994), "Estimating Basal Heave Stability for Braced Excavation in Soft Clay", Journal of Geotechnical Engineering Division, ASCE, Vol. 120, No.8, pp. 1430-1436.

Goh, A. T. C., Wong, K. S., and Kulhawy, F. H. (2005), "Reliability Assessment of Serviceability of Braced Excavation Systems", Underground Singapore, Singapore.

Goh, A. T. C., and Kulhawy, F. H. (2005), "Reliability Assessment of Serviceability Performance of Braced Retaining Walls Using A Neural Network Approach", Intl. J. Numerical & Analytical Methods in Geomechanics, Vol. 29, pp. 627-642.

Goh, A. T. C., Kulhawy, F. H. and Wong, K. S., (2008), "Reliability Assessment of Basal-heave Stability for Braced Excavations in Clay", Journal of Geotechnical and Geoenvironmental Engineering, Vol. 134, No. 2, pp. 145-153.

Halim, D. (2006), "Effect of Excavation on Performance of Adjacent Buildings", Ph.D, Thesis, Nanyang Technological University.

Hardin B.O. and Black W.L. (1968), "Vibration Modulus of Normally Consolidated Clays", Proc. ASCE: Journal of the Soil Mechanics and Foudations Division, 94 (SM2): 353-369.

Hardin B.O. and Drnevich V.P. (1972), "Shear Modulus and Damping in Soils: Design Equations and Curves", Proc. ASCE: Journal of the Soil Mechanics and Foudations Division, 98 (SM7): 667-692.

Hardin B.O. and Richart F.E. (1963), "Elastic Wave Velocities in Granular Soils". Proc. ASCE: Journal of the Soil Mechanics and Foudations Division, 98 (SM1): 33-65.

Harr, M. E. (1984), "Reliability-Based Design in Civil Engineering", 1984 Henry M. Shaw Lecture, Dept. of Civil Engineering, North Carolina State University, Raleigh, N. C.

Hashash, Y. M. A., Whittle, A. J. (1996), "Ground Movement Prediction for Deep Excavations in Soft Clay", Journal of Geotechnical Engineering, Vol. 122, No. 6, pp. 474-486.

Hashash, Y. M. A., Whittle, A. J. (2002), "Mechanisms of Load Transfer and Arching for Braced Excavations in Clay", Journal of Geotechnical and Geoenvironmental Engineering, Vol. 128, No. 3, pp. 187-197.

Hasofer, A. M., and Lind, N. C. (1974), "Exact and Invariant Second-moment Code Format", J. Eng. Mechanics, ASCE, Vol. 100, No. 1, pp. 111-121.

Hsiao, E. C. L., Schuster, M., Juang, C. H., and Kung, G. T. C. (2008), "Reliability Analysis and Updating of Excavation-Induced Ground Settlement for Building Serviceability Assessment", Journal of Geotechnical and Geoenvironmental Engineering, Vol, 134, No. 10, pp. 1448-1458.

Hsieh, P. G. and Ou, C. Y. (1998), "Shape of Ground Surface Settlement Profiles Caused by Excavation", Canadian Geotechnical Journal, Vol. 35, pp. 1004-1017.

Hsiung, B. C. Benson, Nash, D. F. T., Tsai, W. S. and Hwang, Richard, N. (1999), "Observed behavior of a deep excavation in Taipei", AIT's 40th Anniversary Civil and Environmental Engineering Conference, New Frontier and Challenges, Bangkok, Thailand, Volume II, II- 55- II- 66.

Hwang, N. R. and Moh, Z. C. (2007), "Deflection Paths and Reference Envelopes for Diaphragm Walls in the Taipei Basin", Journal of GeoEngineering, Vol. 2, No. 1, pp. 1-12.

Jardine, R. J., Potts, D. M., Fourie, A. B., and Burland, J.B. (1986), "Studies of the Influence of Non-linear Stress-strain Characteristics in Soil-structure Interaction", Geotechnique, London, England. Vol. 36, No.3, pp. 377-396.

Kulhawy, F. H. (1992), "On the Evaluation of Soil Properties", ASCE Geotech. Spec. Publ. No. 31, pp. 95-115.

Kung, G. T.-C., Hsiao, E. C.-L., Juang. C. H. (2007a), "Evaluation of a Simplified Small-strain Soil Model for Analysis of Excavation-induced Movements", Canadian Geotechnical Journal, Vol. 44, No. 6, pp. 726-736.

Kung, G. T. C., Juang, C. H., Hsiao, E. C., Hashash, M. A. (2007b), "Simplified Model for Wall Defelction and Ground-surface Settlement Caused by Braced Excavation in Clays", Journal of Geotechnical and Geoenvironmental Engineering, Vol. 133, No. 6, pp. 731-747.

Kung, G. T. C., Ou, C. Y., and Juang. C. H. (2008), "Modeling Small-strain Behavior of Taipei Clays for Finite Element Analysis of Braced Excavations", Computers and Geotechnics.

Lambe, T. W., and Whitman, R. V. (1969), Soil mechanics, Wiley, New York.

Lim, K. W., Wong, K. S., Orihara, K. and Ng, P.B. (2003), "Comparison of Results of Excavation Analysis Using WALLAP, SAGE CRISP, and EXCAV97", Underground Singapore 2003, Singapore, pp. 83-94

Low, B. K. (1996), "Practical probabilistic approach using spreadsheet", ASCE Geotechnical Special Publication No. 58, Proc., Uncertainty in the Geologic Environment—From Theory to Practice, Madison, Wisconsin, July 31-August 3, Vol. 2, pp. 1284-1302.

Low, B. K., and Tang, W. H. (1997), "Reliability Analysis of Reinforced Embankment on Soft Ground". Canadian Geotechnical Journal, Vol. 34, No. 5, pp. 672-685.

Low, B. K., and Tang, W. H. (2007), "Efficient Spreadsheet Algorithm for First-Order Reliability Method", Journal of Engineering Mechanics, Vol. 133, No. 12, pp. 1378-1387.

Mana, A. I., and Clough, G. W. (1981). "Prediction of Movement for Braced Cuts in Clay", Journal of Geotechnical Engineering Division, ASCE, Vol. 107, No. 6, pp. 759-777.

Miyoshi, M. (1977), "Mechanical Behavior of Temporary Braced Wall", Proceedings of 6th International Conference on Soil Mechanics and Foundation Engineering, Tokyo, Vol. 2, No. 2/60, pp. 655-658.

Myers, H. R., Montgomery, C. D., Vining, G. G., Borror, C. M., and Kowalski, S. M. (2004), "Response Surface Methodology: A Retrospective and Literature Survey", Journal of Quality Technology, Vol. 36, No. 1, pp. 53-77.

Ou, C. Y., Hsieh, P. G. and Chiou, D. C. (1993), "Characteristics of Ground Surface Settlement during Excavation", Canadian Geotechnical Journal, Vol. 30, No. 5, pp. 758-767.

Ou, C. Y., Liao, J. T., and Lin, H. D. (1998), "Performance of Diaphragm Wall Constructed Using Top-down Method", Journal of Geotechnical and Geoenvironmental Engineering, ASCE, Vol. 124, No. 9, pp. 987-1008.

Ou, C. Y., Teng, F. C., Seed, R. B., and Wang, I. W. (2008), "Using Buttress Walls to Reduce Excavation-Induced Movements", Geotechnical Engineering, 161 August 2008 Issue GE4, pp. 209-222.

Peck, R. B. (1969), "Deep Excavations and Tunneling in Soft Ground", Proceedings of 7th International Conference on Soil Mechanics and Foundation Engineering, Mexico City, State of the Art Volume, pp. 225-290.

Peck, R. B., Hanson, W. E., and Thornburn, T. H. (1974), Foundation Engineering, 2nd ed., Wiley and Sons, NY.

Phoon, K. K. (2004), Vulnerability and Risk Associated with Geohazards General Non-Gaussian Probability Models for First-Order Reliability Method (FORM), A State-of-the-Art Report, ICG Report 2004-2-4.

Poh, T. Y., Wong, I. H. and Chandrasekaran, B. (1997), "Performance of Two Propped Diaphragm Walls in Stiff Residual Soils", Journal of Performance of Constructed Facilities. Vol. 11, No. 4, pp. 190-199.

Rackwitz, R. and Fiessler, B. (1978), "Structural Reliability under Combined Random Load Sequences", Comput. Struct., 9, 484-494.

Rackwitz, R. (2001), "Reliability Analysis—A Review and Some Perspectives", Struct. Safety, Vol. 23, No. 4, pp. 365-395.

Schanz, T. (1998), Zur Modellierung des Mechanischen Verhaltens von Reibungsmaterialen, Habilitation, Stuttgart Universitat.

Schanz, T., Vermeer P. A., and Bonnier P. G (1999), "The Hardening Soil Model—Formulation and Verification", Beyond 2000 in Computational Geotechnics. Amsterdam, Balkema, pp. 281-296.

Schweckendiek, T. (2006), "Structural Reliability Applied to Deep Excavations – Coupling Reliability Methods with Finite Elements". MSc thesis. Delft University of Technology.

Schweiger, H. F. (2002), "Results from Numerical Benchmark Exercises in Geotechnics", In P. Mestat, editor, Numge 2002. 5th European Conference Numerical Methods in Geotechnical Engineering, Paris, Vol. 1, pp. 305-314.

Stroud, M. A. (1974), "The Standard Penetration Test in Insensitive Clays and Soft Rocks", Proceedings European Conference on Penetration Tests, Stockholm, Vol. 2. No. 2. pp. 367-375.

Tang, Y. G. and Kung, G. T. C. (2008), "Application of Nonlinear Optimization Technique to Back Analyses of Deep Excavation", Computers and Geotechnics, Vol. 36, Issue. 1-2, pp. 276-290.

Terzaghi, K. (1943), Theoretical Soil Mechanics, Wiley, New York.

Terzaghi, K. and Peck, R. (1967), Theoretical and Applied Soil Mechanics, Wiley, New York.

Twine, D. and Roscoe, H. (1997), Prop Loads: Guidance on Design, Funders Report FR/CP/48, Construction Industry Research and Information Association, London.

Veneziano, D. (1974), "Basic Analysis of Structural Safety", Journal of Structural Engineering, Vol. 109, No. 3, pp. 721-472.

Vucetic, M. and Dobry, R. (1991), "Effect of Soil Plasticity on Cyclic Response", Journal of Geotechnical Engineering ASCE, Vol. 117, No. 1, pp. 89-107.

Whittle, A. J., and Hashash, Y. M. A. (1994), "Soil Modeling and Prediction of Deep Excavation Behavior", Proc., Int. Symp. on Pre-Failure Deformation Characteristics of Geo-Mat. (IS-Hokkaido '94), A. A. Balkema, Vol. 1, pp. 589-595.

Whittle, A. J. and Kavvadas, M. J. (1994), "Formulation of MIT-E3 Constitutive Model for Overconsolidated Clays", Journal of Geotechnical Engineering, ASCE, Vol. 120, No. 1, pp. 173-198.

Wong, K. S. and Broms, B. B. (1989), "Lateral Wall Deflections of Braced Excavation in Clay", Journal of Geotechnical Engineering Division, ASCE, Vol. 115, No. 6, pp. 853-870.

Wong, K. S. (2003), "Observational Approach to Avoid Failures in Temporary Works", Seminar on Avoiding Failures in Excavation Works, Building & Construction Authority, Singapore, 11 July 2003.

Wong, K. S. (2004), "How to Avoid Failures in Deep Excavation", Proceedings of International Conference on Structural and Foundation Failures, Singapore, pp. 384-397.

Wong, I. H., Poh, T. Y., and Chuah, H. L. (1997), "Performance of Excavations for Depressed Expressway in Singapore", Journal of Geotechnical Engineering Division, ASCE, Vol. 123, No. 7, pp. 617-625.

Wroth, C. P., and Houlsby, G. T. (1985), "Soil Mechanics-property Characterization and Analysis Procedures", Proceedings of the 11th International Conference on Soil Mechanics and Foundations Engineering. San Francisco, pp. 1-55.

Wroth, C.P., Randolph, M. F., Houlsby, G. T., and Fahey, M. (1979), A Review of the Engineering Properties of Soils with Particular Reference to the Shear Modulus, CUED/D-SOILS TR 75, University of Cambridge, 79 p.

Yoo, C. (2001), "Behavior of Braced and Anchored Walls in Soils overlying Rock", Journal of Geotechnical and Geoenvironmental Engineering, Vol. 127, No. 3, pp. 225-233.